THE UNIVERSITY OF OKLAHOMA

GRADUATE COLLEGE

ADDITIVE MANUFACTURING AND DESIGN OF MECHANICALLY TAILOR-MADE HYBRID COMPOSITES WITH ARTIFICIAL INTELLIGENCE

A DISSERTATION

SUBMITTED TO THE GRADUATE FACULTY

in partial fulfillment of the requirements for the

Degree of

DOCTOR OF PHILOSOPHY

By

SANJIDA FERDOUSI

Norman, Oklahoma

2024

ADDITIVE MANUFACTURING AND DESIGN OF MECHANICALLY TAILOR-MADE HYBRID COMPOSITES WITH ARTIFICIAL INTELLIGENCE

A DISSERTATION APPROVED FOR THE

SCHOOL OF AEROSPACE AND MECHANICAL ENGINEERING

BY THE COMMITTEE CONSISTING OF

Dr. Yijie Jiang, Chair

Dr. Mrinal Saha

Dr. Shuozhi Xu

Dr. Byeong-Min Roh

Dedicated to

My dearest husband Md Mosharaf Hossain

ACKNOWLEDGEMENTS

This chapter of my life has been profoundly rewarding and I am truly thankful for the decision to pursue this path in completing my doctoral degree. I want to express my heartfelt thanks to everyone who has supported and guided me throughout my doctoral journey. First and foremost, I am deeply grateful to my advisor, Dr. Yijie Jiang, for his unwavering support and guidance. I feel truly fortunate to have had the privilege of working with such an exceptional mentor. When I began, my research experience was limited and Dr. Jiang patiently guided me every step of the way appreciating my efforts, introducing me to fascinating research topics, and helping me acquire invaluable new skills.

I am also immensely thankful to my dissertation committee members for their insightful feedback, encouragement, and constant support. I extend my sincere gratitude to Dr. Byeong-Min Roh, Dr. Shuozhi Xu, and Dr. Mrinal Saha for being part of my committee and providing invaluable guidance throughout the process. From assisting me with my general exam to organizing the defense their support has been indispensable.

It has been a pleasure to collaborate with incredibly talented co-authors whose contributions have significantly shaped the papers resulting from this dissertation. I would like to express my gratitude to Dr. Rigoberto Advincula, Dr. Wonbong Choi, Dr. Rajiv S. Mishra, Dr. Ravi Sankar Haridas, Dr. Eugene B. Caldona, Marcel Roy B. Domalanta, Karen Y. Patiño Jaimes, Sophia Zoch, Mehrzad Soltani, Guanying Li, Gary Tejeda-Godinez and others for their meaningful contributions to this research.

I am also deeply appreciative of my lab mates and friends who have supported me throughout my doctoral journey. My heartfelt thanks go to Dr. Nurul Islam, Onome, Dr. Lee, Amoko, Alejandro, Hojae, Nipa, and James for their help on various occasions. Additionally, I would like to thank my friends Nitu, Neela, and others for their constant support.

My deepest gratitude belongs to my beloved father Md Akkas Ali, my mother Nazma Begum, and my other family members who cared and supported me along the way. I am forever thankful for their unwavering care and encouragement. Your support has been crucial in helping me reach this stage, and I am deeply grateful for your belief in me.

Lastly, my most earnest thanks go to my amazing husband, Dr. Md Mosharaf Hossain. From the very beginning, he has been my pillar of support, offering comfort, and encouragement whenever I felt overwhelmed. He not only taught me how to navigate research but also helped me develop essential skills. Without his boundless support, patience, and encouragement, this journey would have been far more challenging. I am incredibly grateful to him for always standing by my side and helping me achieve this success.

TABLE OF CONTENTS

LIST OF FIGURES

ABSTRACT

Hybrid composites are composed of multiple fillers incorporated into a single matrix. With enhanced and unique material properties, hybrid composites are suited for specific applications in material science and mechanical engineering, particularly in aerospace, automotive, and sports equipment. Hybrid composites with various fillers of different geometries and properties are multifunctional with complex microstructures that affect mechanical performance. Designing materials with specific characteristics is challenging due to the numerous microstructural factors, such as filler geometries and distributions, as well as the complexity of analyzing these structures. Traditional design methods rely on trial and error which are time-consuming and computationally intensive requiring extensive human intervention for feature extraction and descriptors selection. Recent advancements in materials science leverage artificial intelligence (AI) including deep learning (DL) to tailor microstructure designs for desired mechanical traits and discovery of novel materials through large-scale databases. The main goal of this dissertation is to develop an AI-driven framework for designing tailor-made hybrid composite microstructures with desired mechanical behaviors. By integrating AI with finite element analysis (FEA), additive manufacturing (AM), and experimental validation, the framework aims to establish a comprehensive understanding of structure-property (S-P) and inverse S-P relationships in hybrid composites. Firstly, the study aimed to characterize S-P relationships by leveraging a conventional design of experiments, a theoretical hybrid model, and an image-driven machine learning (ML) approach to investigate the mechanical behaviors of 3D printed lightweight hybrid composites. Then, inverse microstructural designs for hybrid composite materials were developed to achieve tailor-made full-range stress-strain relationships by utilizing FEA and DL techniques. Lastly, inverse S-P relationships were formulated by integrating a domain-specific constraint model which explained the design of tailor-made materials using fundamental knowledge of material design. Custom-designed lightweight materials with AI-driven models will enhance the understanding of S-P relationships in hybrid composites leading to reduced design time as well as computational resources.

CHAPTER 1

INTRODUCTION

2.1 Overview

The development of multiscale hybrid composites represents a promising frontier in high-performance lightweight materials with significant potential across industries such as aerospace, automotive, materials engineering, and advanced manufacturing. These hybrid composites combine two or more distinct types of fillers such as different geometries or functionalities incorporated into a matrix to attain enhanced multifunctional or unique properties. The ability to tailor microstructures in composite materials enables exceptional performance under lightweight and high-stress conditions by improving both mechanical properties and efficiency. The advancement of design strategies in materials science now integrates advanced artificial intelligence/ machine learning (AI/ML), such as deep learning techniques for designing microstructures for on-demand materials. Integrating AI-driven models into the design process further enhances the ability to customize these microstructures by refining performance predictions. This integration is promising in novel materials discovery and design through extensive database and mathematical modeling. Understanding the structure-property (S-P) relationships in hybrid composites can transform various industries by reducing environmental impact, improving energy efficiency, and promoting sustainability. The composites demonstrate characteristics like reduced weight, enhanced anti-fatigue properties, and superior tensile strength and stiffness due to their intricate and heterogeneous microstructures.

Lightweight hybrid composites are ideal for flexible structural designs and multifunctional applications which offer the advantages of low density and reduced energy consumption. With advancements in 3D printing, the microstructures of these composites can be precisely tailored through careful control of the manufacturing processes. The mechanical properties of hybrid composites are heavily influenced by the intrinsic characteristics of their fillers and matrices, such as the geometries, densities, and strengths of the fillers, as well as the resulting microstructures shaped by factors like spatial distribution, orientation, and alignment during production. Exploring S-P relationships and customizing microstructural traits enables the achievement of desired material performance by focusing on key mechanical attributes such as strength, ductility, and durability, resulting in improved functionality, efficiency, and reliability across diverse applications.

2.2 Problem Statement

Hybrid composites generally have sophisticated microstructures consisting of several types of fillers along with various length scales and diverse geometries. These intricacies in the microstructures lead to the formation of multi-phase interfaces and local defects that collectively impact their mechanical properties. Therefore, designing tailor-made materials with desired mechanical characteristics poses a formidable challenge due to the multitude of microstructural factors (e.g., filler geometries, orientation, and distribution), and the complexity of controlling and analyzing the diverse structural data sets. Many traditional design approaches relying on trial and error and heuristic rules, are time-consuming and computationally expensive due to numerous design variables, design spaces and required human intervention. Also, existing research often relies on manually selected descriptors and feature extraction from microstructural images which require significant designer's input. Current research focuses on design optimization, while a shortfall remains in structural design for tailor-made properties and the availability of datasets. To overcome the limitations, this study aims to leverage the integration of finite element analysis (FEA) and an AI-driven framework to design tailored hybrid composite microstructures and formulate S-P relationships.

2.3 Objective

The overarching objective of this dissertation is to investigate an AI-driven framework that can effectively design hybrid composite microstructures with tailorable mechanical performance. The AI framework, together with FEA, additive manufacturing (AM) and experimental validation, will enable us to establish fundamental knowledge of S-P and inverse S-P relationships in hybrid composites. We hypothesize that integrating FEA with advanced ML techniques can effectively predict and design these relationships. The specific aims are-

1. Characterize S-P relationships: Leverage a conventional design of experiments, a theoretical hybrid model, and an image-driven ML method to investigate the mechanical behaviors of 3D printed light-weight hybrid composites.

2. Develop microstructural designs: Construct the hybrid composite materials microstructural designs from tailor-made mechanical properties, using the FEA and advanced ML techniques, specifically cGAN.

3. Formulate inverse S-P relationships: Derive the inverse S-P relationships of hybrid composite materials by integrating domain specific constraint model to explain the tailor-made materials with fundamental knowledge of material design.

Custom-designed materials, emphasizing the properties like low density and superior performance will be beneficial in various applications, such as aerospace and automotive parts, sports equipment, and protective coatings for devices. By developing AI-driven models, this research will be able to contribute to a comprehensive understanding of the S-P relationships in hybrid composites and reduce the time and computational resources for designing tailor made structure.

CHAPTER 2

BACKGROUND AND MOTIVATION

2.1 Hybrid Composites

In 2022, the global composite market value was USD 93.69 billion with an expected expansion at a compound annual growth rate (CAGR) of 7.2% from 2023 to 2030.[1,2] The rising market was caused by the increased demand for lightweight components in the automotive, transportation sectors and manufacturing industries for reducing the transportation parts weight focusing on fuel efficiency and performance.[3] From the perspective of lightweight automobiles, a 9% reduction in vehicle weight was led to a 7% to 9% reduction in energy consumption which led to a 1.54% increase in global automotive sales from 2021 to 2022.[4] Furthermore, the global urbanized area increased by approximately 6.92% from 2016 to 2022, which also tended to boost the demand for hybrid composites in both the automotive and construction sectors.[5] Several types of fibers are renowned for their high strength and lightweight properties, such as carbon fibers, aramid fibers (such as Kevlar), ultra-high-molecular-weight polyethylene (UHMWPE), glass fibers, and so on. Among them, glass fiber was favored for its tensile strength, rigidity, and lightweight properties, making it a preferred material for composite manufacturing with a 60.0% revenue market share in 2022.[6] Carbon fiber reinforced polymers (CFRP) are known for their lightweight, high tensile strength and are commonly used in both interior and exterior aircraft applications.[7] Based on the fiber, composites can provide ranging from 15% to 40% more lightweight property.[6] With the inflated demand of lightweight material towards the progress of automotive, aircraft production and manufacturers industries, the competition and growth of the hybrid composite are anticipated to intensify.[1,8]

Hybrid composites comprise a matrix and two or more fillers with distinct properties and diverse geometries to achieve a synergic effect that single filler composites often lack.[9,10] Hybrid composites can have high specific properties and enhanced material performance in applications of aerospace, automotive, packaging, lightweight structures, civil engineering, aviation, sports, biomedicine, thermomechanical components, and other fields.[11–13] Designed with diverse materials, hybrid composites can demonstrate particular characteristics, such as high strength-to-weight ratios, improved anti-fatigue properties, high tensile strength and stiffness, exceptional durability, tailored thermal and electrical conductivity due to their complex and heterogeneous microstructures.[10,14] Lightweight hybrid composites can benefit flexible structural designs and multifunctional applications with low density and less energy consumption.[15] Furthermore, hybrid polymer composites microstructures are significantly influenced by factors such as the morphology, characteristics such as type, size, shape, distribution and orientation of fillers, along with other design variables of constituent elements.[16]. Traditional methods often explored and optimized this intricate design space and its influencing factors. For example, design of experiments (DOE) approaches was utilized to conduct and analyze experiments for understanding the effects of various factors and their interactions. In DOE, experimental planning, such as the Taguchi method, and analysis of variables (ANOVA) were used to quantify the process-property relations to optimize materials performance.[17,18] Various techniques, such as morphological analysis, regression analysis, gray relational analysis, and tensile and rheological tests, were needed.[19–22] However, given the complexity of microstructural design spaces and the high dimensionality of the design variables, the reliance on these approaches made the exploration of each factor individually time-consuming and labor-intensive. Heuristic rules and trial-and-error approaches were used to experiment with different processing conditions and material compositions based on empirical knowledge. However, this approach falls short in designing novel composites with advanced or tailored properties.[19,23,24] Constituent-Based Design plays a pivotal role in systematically selecting and combining materials to achieve desired composite characteristics. This design focuses on developing mathematical models to explain the relationship between the stress, strain, and failure mechanisms of composites at different scales and also incorporate the effects of microstructural factors.[25]

2.2 Additive Manufacturing (AM)

In the realm of AM, the intricate interplay between process parameters, material microstructure, and the resulting properties of manufactured parts is quite significant.[26–28] Particularly in extrusion based composites, the precise control over the intricate spatial arrangement of materials at the microscopic level plays a pivotal role in defining the microstructure which directly influences the mechanical and thermal characteristics of the final product.[29] Through leveraging these relationships, significant progress has been made in the field of 3D printing, particularly in the development of advanced composites that exhibit superior mechanical characteristics with controlled manufacturing processes.[30–33] 3D printing requires a comprehensive understanding and careful optimization of numerous factors, including raster speed, extrusion temperature, nozzle diameter, printing speed and material properties such as ink composition, viscosity, spatial distribution, filler orientation, and so on. With the advancement of 3D printing, the microstructures of composites can be carefully tailored by the control of manufacturing processes.[30–33] The mechanical properties of the composites highly rely on the intrinsic material properties of the fillers and matrix, such as fillers' geometries, densities, and strength, as well as resulting microstructures due to manufacturing processes, including spatial distribution, orientation, and alignment of the fillers.[12,24,31,33,34]

Leveraging the 3D printing process parameters, various works have been done with a focus on manipulating the spatial structural variation by 3D printing to achieve advanced composites with higher stiffness, toughness, and fatigue thresholds, which may have orders of magnitude enhancement.[24,32,34–36] For example, Mo and Raney[33] harnessed a rotational nozzle and printing path designs to enable elongated and helical fiber alignments and created mechanical anisotropy by spatial distribution for aorta-inspired fiber composites. Mechanical properties contrast was obtained by printing a series of regions with various filler orientations.[33] In light of the manufacturing, the nature-inspired composites exhibited different deformation modes and high resistance to failure, even with significant defects and under cyclic loads. Another example is that Muth et al.[32] 3D printed porous cellular structures and evaluated them with adjustable microstructures, geometries, and stiffness through the modification of ink composition, printing path, and sintering conditions. Compared to bulk-cast foam and light-based 3D printing structures, a unit cell based on these architected structures featured at least one order of magnitude less density and higher stiffness.[32] Understanding the processing of advanced composites requires linking process-structure-property (P-S-P) relationships through both statistical methods (like DOE and ANOVA) and theoretical modeling (including continuum mechanics and micromechanical models) to optimize material performance and correlate mechanical properties with structural heterogeneity and 3D printing. Despite the great effort in theoretical models, it remains challenging when different heterogeneous fillers are considered, or experimental uncertainties are considered rather than the ideal conditions.[25]

2.3 S-P Relationships

To explore the composites design space, formulating the S-P relationships has been required to determine the combination of microstructure to obtain tailor properties. For a comprehensive understanding of the P-S-P relationships, various works have focused on creating constitutive models. In constitutive modeling, various analytical models, such as continuum mechanics and micromechanical models, have been investigated for different material combinations and mechanical constraints.[37–41] For instance, continuum mechanics models have been proposed to illustrate the phenomena, including the stretch-induced softening in elastomers-based composites and anisotropic damage parameters of the fiber reinforcement for the mechanical response of soft biological tissues, such as tendons and blood vessel walls.[37,38,42,43] Micromechanical models, such as shear lag models and energy release rate calculations, have been used to evaluate the shear stress distribution at filler-matrix interfaces and establish failure mechanisms.[44,45] The field of S-P relationships has been explored based on statistical parameters derived from 3D printing processes or computational modelling, such as average filler dimensions, average orientation angles, roughness of interfaces, and average inter-filler distances.[46,47] In order to investigate S-P relationships, individual statistical parameters effect on mechanical behavior were generally discussed using constitutive and computational models.[24,40,48] In addition, process parameters of 3D printing were also analyzed to identify and derive mechanical properties like stiffness, failure strength, damage behavior for the correlation of S-P.[49] To address the variability and uncertainties in the mechanical properties of composites, the parameters for 3D printed additive manufacturing were tailored to analyze damage, failure behavior, and interlayer bond strength, using the stochastic constitutive modeling approach.[50,51] Constitutive mechanical modeling has also relied on factors like strain rates, temperature, and filler-reinforced adhesives to predict mechanical properties along with the fracture analysis of elasto-plastics based composite to overcome the traditional trade-off between plasticity and strength design strategies.[52–54] To define the relationship between microstructure and mechanical properties, microstructure-based theoretical model was also developed and validated, offering predictions on tensile strength to show the influence of microstructural factors such as filler dimensions and volume fraction.[55] Despite the great effort in theoretical models, it remains challenging when different heterogeneous fillers are considered, or experimental uncertainties are considered rather than the ideal conditions.[25]

Traditional methods are good starting points, however, designing hybrid composites presents formidable challenges due to their nonlinear behavior, multiphase nature, and the various challenges in optimization, testing, environmental sensitivities, and manufacturing.[56–58] Hybrid composites require sophisticated design approaches due to their intricate properties for effective optimization. To address the complexity and variability of the control factors, advanced techniques like computational modeling, finite element analysis, and molecular dynamics simulations integrated by empirical and data-driven methods have become necessary for a more comprehensive understanding and optimization.[59,60] Particularly in addressing intricate rheological behaviors and microstructural variations, these approaches can capture with great accuracy. Consequently, the uses of computational models, artificial intelligence specifically ML models has been quite promising towards the advancement of the tailor-made properties.[61,62]

2.4 AI-driven Design of Hybrid Composites

ML is a branch of AI which has recently become a pivotal technology in mechanical engineering. ML models have become integral to structural analysis of composite materials, especially in computational mechanics for predicting the properties and failure points of structural elements by leveraging vast data from experiments and simulations.[63–67] ML model employs statistical and probabilistic techniques to identify patterns within extensive datasets which facilitates the prediction and analysis of structural behaviors and material properties using advanced computing power and algorithms.[68] Deep learning (DL) model is a subset of ML and artificial intelligence which leverages neural networks with multiple layers to model and understand the complex relationships between the structure of composite materials and their properties. These DL models can learn from vast amounts of data to predict the material behavior under any loading conditions by identifying the patterns and hidden relationships.

2.4.1 Predictive Modelling Approaches

Advanced ML algorithms are transforming composite materials research by enhancing the analysis of mechanisms in additive manufacturing and structural design. Also, they are outperforming traditional methods in predicting flexural behavior and establishing P-S-P correlations for controllable mechanical parameters. Several studies have integrated AI technologies, including ML and DL, across various fields for emphasizing their impact on enhancing computing capabilities and enabling sophisticated tasks such as self-teaching and identifying complex patterns. This role of AI improves numerical modeling for predicting material properties traditionally reliant on extensive experimentation. To address the complexity of relationships and the high dimensionality in the design and analysis of polymer composites, advanced algorithms and predictive modeling are supplemented by experimental validation to optimize properties like strength and lightweight.[69] The application of Artificial Neural Network (ANN) in constitutive modeling of composite materials and predicting the impact energy absorption of thermoplastic composites has been explored to forecasts the mechanical properties in optimizing the design by leveraging the progressive failure behavior of composites.[70,71] This process facilitated the integration of analytical modeling, multiscale modeling, experimental data and physics-based simulations to demonstrate the potential of AI.[65,72] Hybrid ANN approaches were utilized to optimize 3D printing parameters and for damage identification in composites, targeting the enhancement of PSP relationships.[73–75] ML algorithms have been used to predict and optimize the fiber-reinforced polymer composites properties through streamlining design processes and overcoming traditional experimental constraints through computational methods.[25,76]

2.4.2 ML-driven Material Designs

The exploration into the design of bio-inspired materials through the computational modeling, AI, and big data showcases the application of multiscale simulations and AI in exploring the vast design space of soft bio-inspired materials for material discovery and design.[77] The application of ML in design has revolutionized reinforced polymer composites to achieve and investigate durable and superior properties for multiscale and multifunctional productions.[68,78,79] Further studies elaborate on various aspects of AI's application from predictive modeling, property optimization and material's structural design optimization to the development of novel composite materials and the enhancement of manufacturing processes and sustainable development.[70,74,75,78,80] Furthermore, the ML has advantages in analyzing large databases and establishing mathematical relations in novel materials discovery and design. To design optimal composite materials, traditional methods like gradient-based topology optimization and genetic algorithms have been extensively utilized. Recent research on generative inverse design networks (GIDN) offers a novel approach by optimizing design variables through random initialization and incorporation of active learning to optimize material properties with less data. Despite GIDNs demonstrating potential with high prediction accuracy and improved design quality, their effectiveness relies on the availability of comprehensive, representative data, and face challenges in achieving satisfactory outcomes across various design objectives.[81] Due to advances in additive manufacturing, topology optimization techniques are increasingly utilized to optimize material distribution to enhance performance which is transitioning from homogenization-based approaches to multi-scale structures.[82–84] Designing these multi-scale structures poses significant challenges to address constraints such as pattern repetition and local volume limitations. Despite recent progress involving the application of diverse methods such as SIMP (solid isotropic material with penalization) and inverse homogenization, achieving specific properties in these complex designs remains a formidable challenges.[82,85] In response to the need for a deeper understanding of S-P relationships, researchers have explored several structural optimization techniques.[86–88] These methods involve the selection of relevant properties or attributes and formulation of an objective function using optimization algorithms to iteratively adjust the structure to optimize this function while considering constraints. This process explores the design space, accommodating parameters like geometry and materials, and often requires iterative refinement to converge toward an optimal solution.[89,90]

2.4.3 Image-based ML Models

Promising computational approaches based on advanced ML algorithms have emerged in composites studies, from nanoscale interface mechanics to large-scale structural designs.[91–95] To evaluate the influence of composite mechanisms in additive manufacturing, a recent study developed a data-driven framework on composite systems using a regression ML model and compared that with conventional linkage techniques.[91] Similarly, other studies have investigated the effects of structural design variables on flexural behavior using an ensemble learning data-driven model. They compared it with physics-based approaches and linear regression models, where the data-driven model achieved improved performance.[92] Further efforts were applied to establish the P-S-P correlations considering their variables by developing a ML-based framework to demonstrate the ML model's efficiency and obtain controllable mechanical parameters.[93] Different than the data-driven models, fewer studies are using image-driven ML models, which could capture details of the microstructures direct from experimental observations and establish direct prediction based on the S-P relationships. There are several types of image-driven ML models such as Convolutional Neural Network (CNN), Autoencoder, Recurrent Neural Network (RNN), Generative Adversarial Network (GAN), Support Vector Machines (SVM), Decision tree, Random Forest and so on.[96] The main functionalities of image-driven ML models are designed and adapted for generating, reconstructing, sequencing, and classifying images. Among them, CNN is capable of recognizing images and extracting features from them. CNN provides scalable techniques for pattern recognition by utilizing the patches through whole images to identify the local features.[97,98] The algorithm passes through several processing layers where it translates and relates image properties closer to the output at each step.[25,99] Subsequently, Conditional Generative Adversarial Network (cGAN) excel in generating images focusing on specific conditions which enables precise control over the characteristics of the generated images. By conditioning the generation process based on the labeled, cGAN facilitate targeted image creation, enhancing the diversity and relevance of the outputs.[100]

2.5 FEA and ML Combined Approaches in Composites Design

In the exploration of inverse S-P relationships of hybrid composites, computational modeling approaches like the FEA employ sophisticated models and simulations to work on a tailored material's properties and its structure across various length scales. With recent advances in computational modeling, predictions for new composite configurations under different conditions become much easier for complex hierarchical composite designs for desired properties. The optimal combinations of microstructure and materials property allow to analyze for various loads and boundary conditions to replicate the realistic cases and obtain detailed insights into the stress, strain, and deformation patterns within the composite material. The integration of deep learning with finite element analysis creates a powerful tool to investigate the S-P relationships for lightweight hybrid composites with tailored properties for specific applications. The deep leaning model also shows their versatility in inverse design across a spectrum of materials, including polymers, photonic materials, inorganic solid-state functional materials, porous materials, and thermoelectric materials. Prior researchers have employed ML to streamline materials discovery and design, enabling the prediction of property behavior and structural optimization.[101–103] Additionally, ML approaches have been utilized for exploring molecular space, navigating complex high-dimensional microstructure spaces, and accommodating multi-objective application needs.[85,103] Constitutive and computational models were used for defining the individual statistical parameters effect on mechanical behavior.[24,40,48] Furthermore, data-driven and deep learning techniques were also investigated to build quantitative correlations between microstructures and property values.[35] Functional data analysis also used to validate the relation between physical parameters and microstructural parameters in polymer composites.[104] However, previous research often focuses on predicting the mechanical property or optimizing structures using predefined descriptors which relies on manually selecting descriptors or extracting features from microstructural images, and requiring designer intervention.[25,91,105]

2.6 Outline

Currently, the predominant research emphasis is on microstructure design and optimization as well as notable gap exists in the inverse structural design based on tailor-made properties. ML models have the potential to explore diverse material properties within a given microstructure for further understanding of novel materials. In this dissertation, an AI-driven framework was developed by integrating FEA, ML, and mechanical experiments to effectively design hybrid composite microstructures with tailorable mechanical properties by leveraging fundamental knowledge of S-P relationships. The details of the experimental process, statistical analysis, ML model creation, and FEA simulations are discussed in Chapter 3. A composite mechanics model and an image-driven DL model were established to predict mechanical properties, as discussed in Chapter 4. Statistical analysis identified key printing parameters, such as printing direction and volume fraction of fiber, which significantly affected the mechanical properties. The developed hybrid mechanics model captured the trends of mechanical properties and showed the upper bound results due to the inconsideration of local uncertainty. The image-driven ML model demonstrated better performance compared to the hybrid mechanics model by capturing experimental uncertainty. In Chapter 5, a computational and DL-based framework was developed for the tailored designs of hybrid composite materials' microstructures. Within the framework, a generative DL model was built with the capability of generating tailored microstructures for desired mechanical characteristics. This process also involved simulating two different composites for transfer learning approach to validate the generative DL model performance. Simulated data frame was utilized to train DL model to successfully generate the tailor microstructure with accurate resemblance for specific mechanical behavior. By integrating a domain specific constraint model, inverse S-P relationships were formulated to explain the experimental tailor-made materials with fundamental knowledge, as described in Chapter 6. Furthermore, an automotive parts application was introduced to attain uniform stress distribution across different segmented parts.

CHAPTER 3

MATERIALS AND METHODS

3.1 Materials

In this study, various polymer matrices and fillers were employed to fabricate hybrid composite materials. The primary matrices used were polydimethylsiloxane (PDMS) and epoxy which were selected for their mechanical properties, flexibility, low cost, and ease of processing. The fillers included glass microfibers, hollow spherical glass microparticles, carbon fibers, and glass fibers, which were incorporated to tailor the structural and mechanical properties of the composites. The PDMS matrix was formulated using Dow Corning® SE 1700 to balance mechanical stiffness, flexibility, and providing a suitable base for the inclusion of reinforcing fillers. The fillers were glass microfibers (FibreGlast®, initial length 123.1 ± 92.03 μm and diameter 11.7 ± 3.34 μm) and hollow spherical glass microparticles (FibreGlast®). Glass microfibers were used to improve the tensile strength and stiffness of the PDMS matrix due to their high aspect ratio and reinforcing capabilities. Hollow spherical glass microparticles low density and spherical shape help reduce the composite's overall weight while providing structural reinforcement. This also enhance stiffness without significantly increasing mass which makes it ideal for lightweight applications. The microparticles were experimentally determined to have a density of 0.13 ± 0.05 g/cm^3 based on casted composites with different particle fractions, an external diameter of 47.8 ± 1.33 μm by using optical microscopy, and a wall thickness of 160 ± 99.7 nm by calculations based on the external diameter and particle density.

Additionally, two different epoxy-based composites were fabricated using distinct reinforcing fillers. One composite incorporated carbon fibers and glass particles where the carbon fibers enhanced tensile and flexural strength due to their high strength-to-weight ratio. The second epoxy composite was reinforced with glass fibers and glass particles with the glass fibers improving stiffness and durability. In both epoxy composites, glass particles were used to further enhance mechanical properties by creating balanced materials suitable for structural applications that require strength, durability, and lightweight characteristics.

3.2 DIW 3D Printing of Hybrid Composites

An extrusion-based AM method, direct ink writing (DIW) 3D printing was used to fabricate the hybrid PDMS-based composites. To formulate the 3D printable inks, mixtures of two types of PDMS, glass microfibers and hollow spherical particles, were used. For the matrix, PDMS from Dow Corning® SE 1700 (1:10 crosslinker ratio) and Dow Corning® Sylgard 184 (1:10 crosslinker ratio) were formulated at a ratio of SE1700: Sylgard 184 = 10:1.5. Volume fractions between 0 and 9% for each filler, respectively, were added to formulate different inks. The mixtures were mixed at 1600 rpm in a vacuum for 5 min in a bladeless planetary mixer (FlackTek, SpeedMixer™, DAC 400.2 VAC). The composite ink was then transferred into a 30 cc syringe and centrifuged at 1400 rpm for 4 min to condense the inks and remove air bubbles. The loaded syringe was mounted on a home-built DIW 3D printer, which used a MakerGear® M2 platform and a high-precision Nordson® Ultra™ 2800 volumetric extrusion control system. Three different nozzle sizes (400, 610, and 800 µm) were used to extrude the materials. The extrusion rate was 0.0018–0.004 cc/s, and the printing speed was 10 mm/s. Tensile dog bone specimens with different thicknesses (0.6–1.2 mm) and printing directions (0◦, 45◦, and 90◦ against the longitudinal direction of the tensile bars) were 3D printed. The printed composites were cured at 100 ◦C for 40 min.

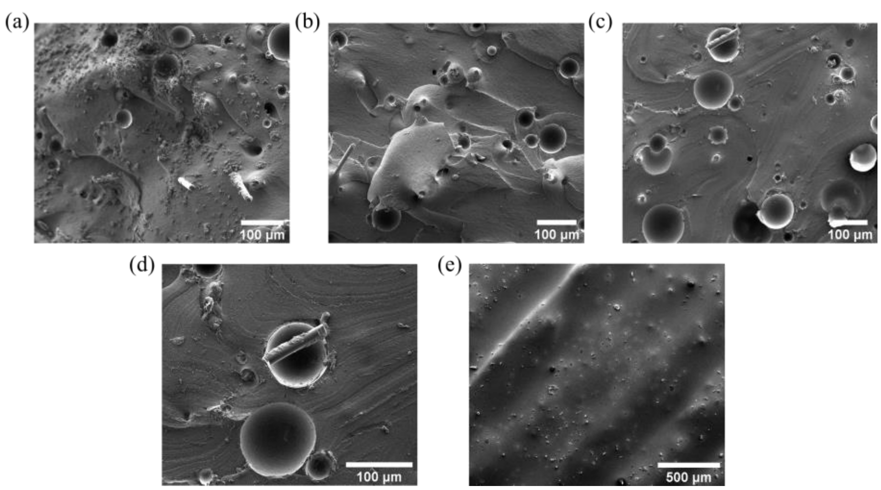

Figure 3.1: SEM microstructure of 3D printed hybrid composites. The cross section of the tensile tested specimen of (a) 3 vol% of fibers, 3 vol% of particles, and 0° printing direction; (b-d) 3 vol% of fibers, 9 vol% of particles, and 0° printing direction; and (e) surface of the 3D printed hybrid composite specimen.

Microstructures were observed under an Amscope® MU1803 optical microscope at 10× magnification. At least 8 images of each printed specimen were taken for later use in ML studies.

Uniaxial tensile tests were conducted in a universal testing machine (Shimadzu® AGS-X) at a constant nominal strain rate of 0.0067 1/s. Nominal stress-strain curves were then obtained from the force-displacement curves, and key mechanical properties, including stiffness, ultimate tensile strength, and toughness, were calculated for later analyses. The scanning electron microscope (FEI Quanta 200 ESEM) images of the cross section and top surface of the tensile tested specimen were shown in Figure 3.1.[25]

3.3 Taguchi Method and ANOVA

Taguchi DOE method[106] was used to investigate the effect of process parameters on mechanical properties. There were four parameters, namely the volume fraction of fibers, the volume fraction of particles, printing direction, and nozzle size, and three levels each (Table 3.1). An L9 orthogonal array was determined by the Taguchi method (Table 3.1-2) and 4 specimens and mechanical tests were performed for each case. Statistical ANOVA analyzed experimental data on mechanical properties, including stiffness, strength, and toughness, with processing parameters.[17,106] Significant tests using the F-test with a 95% confidence interval and the percentage of contribution for each process parameter were shown in Figure 4.3.[25]

Table 3.1. Taguchi L9 orthogonal array design.

Exp no.	Fiber (vol%)	Particle (vol%)	Printing direction (°)	Nozzle size (μm)	Tensile strength (MPa)	Stiffness (MPa)
1	3	3	0	400	1.65 ± 0.36	1.03 ± 0.19
2	3	6	45	600	1.81 ± 0.19	1.15 ± 0.07
3	3	9	90	800	1.95 ± 0.09	0.89 ± 0.06
4	6	3	45	800	2.04 ± 0.05	0.97 ± 0.01
5	6	6	90	400	1.43 ± 0.15	0.96 ± 0.06
6	6	9	0	600	1.98 ± 0.16	1.87 ± 0.26
7	9	3	90	600	2.25 ± 0.11	0.99 ± 0.07
8	9	6	0	800	2.13 ± 0.15	2.51 ± 0.26
9	9	9	45	400	2.43 ± 0.49	1.68 ± 0.27

Table 3.2. Response table for mean values identifying the affecting parameters.

Parameter	Fiber (vol%)	Particle (vol%)	Printing direction	Nozzle size
Level 1 (Experiment no.)	1,2,3	1,4,7	1,6,8	1,5,9
Level 2 (Experiment no.)	4,5,6	2,5,8	2,4,9	2,6,7
Level 3 (Experiment no.)	7,8,9	3,6,9	3,5,7	3,4,8

3.4 ML Models

A ML model is a technique that identifies patterns and relationships within data by applying an algorithm. This process allows the model to make predictions about new, unseen data with a certain level of accuracy. ML models come in various forms, including supervised, unsupervised, and reinforcement learning approaches. In particular. Supervised learning is widely used for datasets that include labeled training data, which consists of input features and their corresponding target variables. These datasets are utilized to teach the model through examples, helping it to discover the connections and patterns between the features and variables.[95] Image-based ML models emerge as a powerful extension of supervised learning techniques for visual data interpretation by applying the foundational mechanism to this domain. There are several types of image-based ML models representing a specialized category that focuses on the analysis and interpretation of visual data by performing a variety of tasks, including image classification, object detection, and image segmentation. Image-based models manage high-dimensional data, with each image pixel serving as a unique feature. Image-based ML models are utilized to interpret and interact for recognizing specific objects within an image, identifying distinct patterns, such as edges and shapes, classifying images into categories, creating new images that mimic those seen during training and so on.

3.4.1 CNN

An integrated set of building blocks was used in CNN to systematically design, acquire, and extract the knowledge of features' spatial sequence from low-level to high-level patterns by employing backpropagation. CNN has the capability of learning and extracting meaningful features from complex, high-dimensional images. The CNN model architecture also can identify the microstructural features while predicting the desired output with higher accuracy without the feature engineering that requires in other classical ML models.[107–109] An image-driven CNN deep learning model was used to investigate the S-P relationships. [98,110]

In CNN[111–115], we have three basic parameters weights, bias and filters. In the first step, when the image goes through the convolution layer small filters pass through the image pixels and extract important features from the image. The fully connected layer operates two functions on data- linear and nonlinear transformations. The linear transformations are-

$$Z = W^T x + b \tag{3.3.1}$$

where x is the input, W is the weight and b are the bias. As the linear transformation unable to detect complex form, the nonlinear transformation introduced to assist. In the backward propagation model, the models update the parameters using gradient descent technique. Using the chain rule, the change in error is calculated with respect to error which are-

$$\frac{\partial E}{\partial W} = \frac{\partial E}{\partial O} \frac{\partial O}{\partial Z_2} \frac{\partial Z_2}{\partial W} \tag{3.3.2}$$

The overall change in the error with respect to filter are-

$$\frac{\partial E}{\partial f} = \frac{\partial E}{\partial O} \frac{\partial O}{\partial Z_2} \frac{\partial Z_2}{\partial A_1} \frac{\partial A_1}{\partial Z_1} \frac{\partial Z_1}{\partial f} \tag{3.3.3}$$

The error evolved during each step/ layer. In each iteration, we can update our filter matrix using these equations-

$$f = f - lr * \frac{\partial E}{\partial f} \tag{3.3.4}$$

Where, parameter represents by f, learning rate by lr and gradient of parameter by $\frac{\partial E}{\partial f}$. This step is repeated throughout the iteration of CNN.

In our models, five convolutional layers were used with 256, 128, 64, 32, and 16 numbers of channels/filters and (3,3) kernel/filter size with the same padding. The max pooling layer had a (2,2) filter size. A rectified linear unit (ReLU) was used as an activation function for all convolutional and fully connected layers. The nonlinear transformation ReLU function of $f(x)=\max(0, x)$ was used. After the convolutional layer, the data set was flattened and used in a single fully connected layer with 256 neurons. The output size was 1 with an input shape of (128,128,3). For training, mean square error (MSE) was used as a loss function and “adam” optimizer,[110] which was the extension of stochastic gradient descent to update the learning rate of each network's weight. To avoid overfitting, an early stopping method is used with the patience of the early stopping in 3 epochs to terminate the training after 3 epochs when the model performance has not improved. Here, validation loss was used as a monitor with a mode minimum to minimize the loss. To train the model, 100 epochs were utilized with 16 batch sizes. The whole dataset was split into three sets- training to fit the parameters to the model, validation to tune hyperparameters & validate the fitted model, and testing the dataset to validate the final model for unbiased evaluation. The total datasets were split into 85:15% for training and remaining, and the remaining datasets were divided into 85:15% for validation and testing.

By grid searching, the model was tuned using hyperparameters of the CNN, where the convolutional layers were varied. In the convolutional layer, the variation of the number of filters was 512 to 16; filter/kernel size was 5 to 3. The filter size of the max-pooling layer was also changed from (4,4) to (2,2). The epoch was also tuned from 50 to 100 with 8 to 16 batch sizes. The model performance was validated based on the MSE. For the same 9 cases used in the Taguchi method and theoretical model, 77 samples were prepared, and each case had 8-9 samples. Each sample has 8 microstructure images taken uniformly distributed within the test areas. As a result, a total of 616 microstructural data as an input, along with the mechanical properties as an output, were used in the CNN model.[25]

3.4.2 cGAN

GAN are a type of image-based DL model designed to generate artificial images that mimic real images from training datasets. These networks aim to learn the latent distribution of high-dimensional data through a setup involving two adversarial models: the Generator and the Discriminator. The Generator's primary role is to produce artificial images so closely resembling real images that they are indistinguishable, while the Discriminator's goal is to identify these synthetic images.[116,117] The training process is iterative and concludes when the Discriminator can no longer differentiate between synthetic and real images. At that point, the Discriminator is discarded, and the Generator is preserved for the task of reconstructing synthetic images.[118] Conditional GAN build upon this framework by enabling the Generator to create images based on specific conditions or attributes, further enhancing the versatility of GAN in generating targeted synthetic images.[116] In a cGAN model, the model is conditioned using both input features (x) and label (y) which are fed into both the generator (G) and discriminator (D), with y being used as an additional input layer. Initially, the generator creates a prior input noise of $P_z(z)$. Later, this input noise is updated to incorporate a joint hidden representation of (x) and (y) during training. The objective function of the cGAN framework aims to minimize the loss function of the generator model and maximize the loss function of the discriminator model. The min-max objective functions are defined as: [116–118]

$$\min_G \max_D L_{cGAN}(G, D) = E_{x \sim P_{data}(x)}[logD(x|y)] + E_{x \sim P_z(z)}\left[log\left(1 - D(G(z|y))\right)\right] \quad (3.3.1)$$

Here, P_{data} are the distribution of real images and z is input parameter given to the generator.

In this work, we utilize a deep learning architecture, specifically a conditional Generative Adversarial Network (cGAN), to capture the intricate relationships between microstructure patterns and the mechanical properties of hybrid composite materials.[119] The input to the model includes mechanical properties such as stress-strain sequences, while the output is the generated microstructures that correspond to these properties. The model is trained on a dataset containing force-displacement data from composite structure simulations, which is essential in learning the correlations and predicting custom microstructure designs based on specific mechanical properties.

The model leverages a combination of deep learning and transfer learning techniques to generate microstructures with varying mechanical properties. Here, we combine long short term memory (LSTM) layers in a unique way within both the generator and discriminator to understand and use the sequencing patterns in strain-stress data. Mainly, the model uses a cGAN, where the generator synthesizes microstructure images from a combination of latent space vectors and encoded strain-stress sequences. The discriminator assesses these generated images against real ones to ensure their authenticity, utilizing adversarial training with Wasserstein GAN and Gradient Penalty (WGAN-GP) for improved stability and more accurate synthesis.

The generator architecture starts with an LSTM sequence encoder that captures temporal dependencies in the input strain-stress data with a sequence length of 99. LSTM encoder has four layers, each with 256 hidden units, and employs a dropout rate of 0.2 to prevent overfitting. The encoded sequence is then concatenated with a random latent vector of size 128 via a fully connected layer that outputs a feature map of size 512 by 8 by 8. From this point, a series of four transposed convolutional layers progressively expanded the feature map to generate high-resolution images of size 128 by 128. The first transposed convolution layer takes the 512-channel input and produces 256 channels, with a kernel size of 4, a stride of 2, and padding of 1, resulting in an output of 256 by 16 by 16. The next layer further reduces the channels to 128, keeping the same kernel size, stride, and padding, and producing an output of 128 by 32 by 32. The third transposed convolution layer reduces the channels to 64 with the same settings, producing an output of 64 by 64 by 64. Finally, the last layer outputs a three-channel RGB image with a size of 128 by 128.

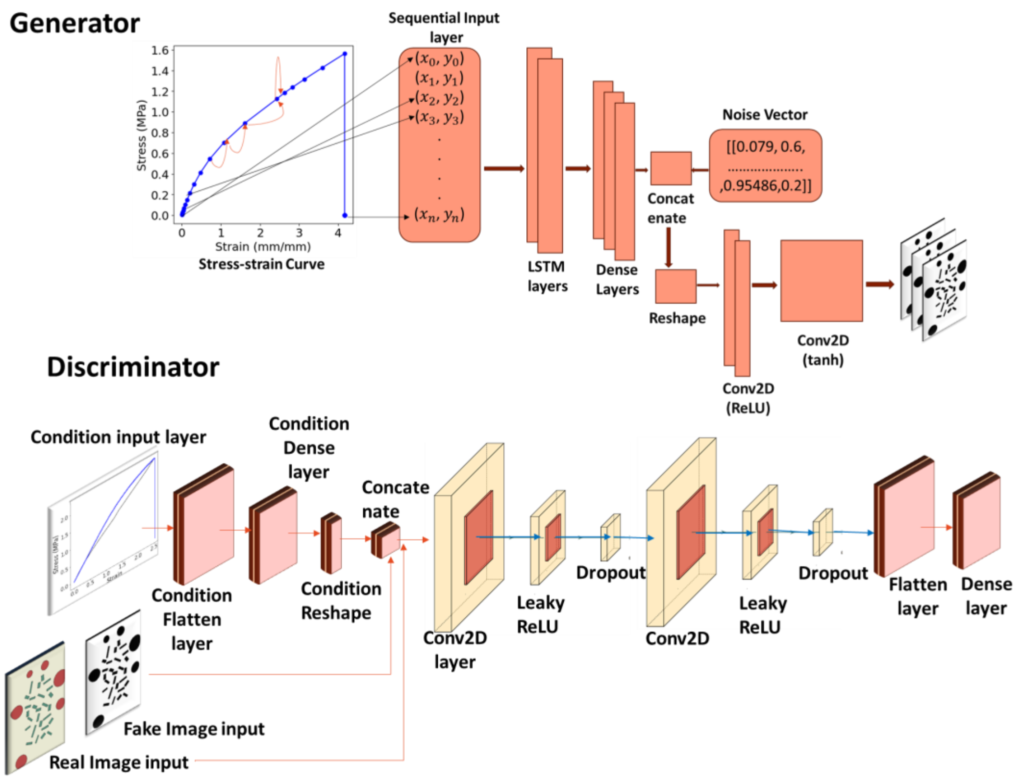

Figure 3.2: Framework of cGAN model generator and discriminator networks.

The discriminator takes both real or generated microstructure images and encoded strain-stress sequences as input. Similar to the generator, the strain-stress sequences are processed through an LSTM sequence encoder with four layers and 256 hidden units. The discriminator uses five convolutional layers to downscale the input image, while simultaneously incorporating the encoded sequence at each layer. The first convolutional layer takes the 3-channel image and concatenates it with the 256-channel encoded sequence, producing a 64-channel output with a kernel size of 4, a stride of 2, and padding of 1, resulting in an output size of 64 by 64 by 64. The second convolutional layer further reduces the channels to 128 using the same settings and produces an output of 128 by 32 by 32. The third layer reduces the channels to 256, producing an output of 256 by 16 by 16, and the fourth layer reduces the channels to 512, outputting 512 by 8 by 8. Finally, the last convolutional layer outputs a single scalar value that represents the authenticity of the image.

Both the generator and the discriminator are trained using adversarial loss, specifically based on the Wasserstein loss function. The generator's objective is to minimize the loss by creating realistic images that deceive the discriminator, while the discriminator maximizes the distance between real and fake images. To stabilize training, a gradient penalty is applied to the discriminator, promoting smooth gradients in the loss function and preventing issues like mode collapse. To further stabilize training, we use $\lambda_{gp} = 10$ for the gradient penalty, and critic update frequency = 5 to update the discriminator five times for each generator update. The training is performed over a batch size of 32, with an initial learning rate of 0.0001, and the Adam optimizer with $\beta_1 = 0$ and $\beta_2 = 0.9$ is used for optimization. To reduce overfitting and improve the model's generalization and performance, the cGAN model was trained for 500 epochs with early stopping criteria based on validation metrics, to prevent overfitting ensuring sufficient convergence and generation quality.

To evaluate the quality of the generated images, we compute the Fréchet Inception Distance (FID), which compares the distributions of real and generated images. A simple CNN-based feature extractor is used to extract features from both sets of images. This CNN consists of three convolutional layers. The first layer takes the 3-channel input and produces 64 channels with a kernel size of 3, a stride of 1, and padding of 1, resulting in an output of 64 by 128 by 128. The second layer reduces the channels to 128, keeping the same kernel size, stride, and padding, and produces an output of 128 by 128 by 128. The third layer reduces the channels to 256, with the same settings, producing an output of 256 by 128 by 128. The feature vector from the third layer is then passed through a fully connected layer, and the FID score is calculated by comparing the means and covariances of these feature vectors between real and generated images.

During the training process, the generator synthesizes microstructure images by reconstructed the encoded strain-stress sequences and latent vectors, while the discriminator evaluates these images by comparing them to real samples. For every update of the generator, the discriminator is updated multiple times, following the WGAN-GP framework. After each epoch, the model's performance is validated using the FID score, and the model is saved if improvements are observed in the quality of the generated images.

A total of 8,054 cases were simulated and used to train, validate, and test the model. The dataset was split using a 70:30 rule. Specifically, 70% of the data (5,637 cases) was allocated for training the model so that the model could learn the patterns and relationships. The remaining 30% (2,417 cases) was further divided equally: 15% of the total dataset (1,208 cases) was used as validation during training for continuous performance monitoring without introducing bias, and the remaining 15% (1,209 cases) was reserved for final testing. Testing set provided an unbiased evaluation of the model's performance after the training phase to ensure generalization on unseen data. A high-performance computing (HPC) cluster with GPU resources was used to train the customized cGAN-LSTM model. Each job was allocated one GPU within the GPU partition and 8 GB of memory to optimize processing time for all computational experiments. The total training time was 3 hours and 32 minutes.

3.4.3 Transfer learning models for simulated datasets

In this study, we employed a transfer learning approach to enhance the model's ability to generate tailored microstructures for a range of material properties, including both flexible and rigid materials. Fine-tuning the pretrained model on these distinct material types led to the creation of high-quality microstructures that closely match the mechanical traits of the new dataset. As a result, the model gained the ability to generalize across a broader spectrum of materials through this transfer learning approach. The core architecture of the pretrained model consisted of a cGAN, with a generator and discriminator, which were retained to maintain compatibility with the pretrained weights. This process allowed us to leverage the knowledge acquired during the pre-training phase, which was originally focused on flexible materials, and adapt the model to handle new material types through fine-tuning.

The transfer learning process involved initializing the model with the pre-trained weights and fine-tuning it on a new, more diverse dataset. During this fine-tuning phase, key hyperparameters were carefully selected to allow for effective adaptation without destabilizing the model. A lower learning rate of 0.00001 was utilized to ensure subtle updates to the pre-trained weights, while the Adam optimizer with β_1= 0 and β_2= 0.9 was employed to maintain stable and consistent gradient updates. The latent dimension (128) and batch size (28) from the original model were preserved to maintain continuity in the generative process. Additionally, a gradient penalty term $\lambda_{gp} = 10$ was applied to ensure smooth training and prevent gradient instability in the adversarial setting of the GAN. The model was trained over 500 epochs, with early stopping criteria based on validation metrics, including the Fréchet Inception Distance (FID) score, to prevent overfitting and capture the best performance.

In the transfer learning model, two distinct datasets were employed: epoxy-carbon fiber-glass particle composite and epoxy-glass fiber-glass particle composite. These datasets were used to train and fine-tune the model for improved performance. This dataset contained similar structural features and sizes as the pre-trained model's dataset. For the epoxy-carbon fiber-glass particle composite, a total of 1,504 cases were simulated. This dataset was split according to an 80:20 ratio. Specifically, 80% of the data (1,203 cases) was used for training the model with training time 1 hour 42 minutes. The remaining 20% (301 cases) was divided into two parts: 10% of the total dataset (150 cases) for validation to obtain real-time feedback of the model's progress during training, and the final 10% (151 cases) for testing the model's performance on unseen data. For the epoxy-glass fiber-glass particle composite, a slightly larger dataset of 1,528 cases was simulated to fine-tune the model. Similarly, the dataset was split using the same 80:20 ratio. Out of the total, 80% (1,222 cases) was allocated for training (training time 1hour 43 minutes), 10% (153 cases) for validation, and the remaining 10% (153 cases) for testing.

3.4.4 Transfer learning models for experimental datasets

In this work, we implemented a transfer learning framework for fine-tuning a cGAN model incorporating domain-specific loss functions to improve the generator's ability to produce tailored microstructures for real-life experimental mechanical properties. For better generalization, we integrated the fine-tuned model with the pretrained model's core architecture, which includes a sequence-conditioned generator and discriminator, preserving the pretrained weights while also updating the base model architecture to address real-life experimental cases. This transfer learning approach allowed us to harness the knowledge from pretrained model on specific microstructure patterns, adapting the model to new datasets through targeted fine-tuning. In this stage, we utilized a transfer learning model where both the model hyperparameters and architecture were updated to optimize performance. Additionally, we incorporated domain-specific loss functions to ensure the generated microstructures closely align with the experimental properties.

The core architecture of this model consists of a simple CNN-based feature extractor, a generator conditioned on both strain-stress sequences and latent noise, and a discriminator responsible for evaluating the realism of the generated images. The fine-tuning process begins by freezing certain layers of the pretrained models and gradually unfreezing them by leveraging knowledge from the pretrained model while adapting the network to new material properties. To control the training process and optimize model performance, we utilized several hyperparameters, including the latent noise vector, sequence length, and image size. The latent noise vector was set to 128 providing input to the generator. The sequence length was set to 99 representing the length of the input strain-stress data and later the LSTM-based encoder processed to generate the latent representation. We fixed the image size at 128x128 pixels to maintain uniformity between the input, output, and evaluation images. The number of image channels was 3 which corresponds to RGB images. We set the batch size to 32 where it allows 32 samples to be processed in each training iteration for balancing computational efficiency and model performance. The number of epochs was set to 500 where the model passed through the entire training dataset 500 iteration to improve learning. We set the learning rate at 0.0005 for both the generator and discriminator to control the step size for updating model weights during training. The Adam optimizer used momentum parameters, with β_1 set to 0.0 and β_2 set to 0.9 to stabilize training by controlling the moving averages of the gradients. To enforce the Lipschitz constraint required for Wasserstein loss with Gradient Penalty, we applied a gradient penalty coefficient λ_{gp} = of 10, ensuring smooth gradient behavior and stable convergence. Additionally, the discriminator was updated five times for each generator update to balance the training dynamics between the two networks.

For fine-tuning, we introduced updated layers for both the Generator and Discriminator models to adapt to the new dataset while retaining the knowledge from the pretrained models. Initially, the original layers were frozen to preserve the patterns learned during pretraining. Three new layers were added to both the Generator and Discriminator to enhance their capacity for generating and evaluating more complex microstructures. In the Generator, the additional convolutional and up sampling layers helped to produce higher-resolution outputs and gradually unfreezing the original layers allowed the model to better adapt to the new data. Similarly, the Discriminator received new convolutional layers to improve its ability to distinguish between real and generated images. To further enhance this process, we employed multiple loss functions to guide the training process. The adversarial loss from Wasserstein loss with Gradient Penalty was used similar to the pretrained model to ensure the generator produced images indistinguishable from real ones, while the discriminator learned to differentiate between them. Additionally, we also incorporated microstructure loss to fine tuning model for comparing the particle statistics, such as size and count, between real and generated images to capture the physical characteristics of microstructures. The SSIM loss also added to measure the structural similarity between real and generated images for improving the visual quality of the generated microstructures. Lastly, the feature matching loss was applied to align feature distributions between real and generated images by comparing intermediate layers in the discriminator to resemble at pixel level as well as in terms of abstract features. So, the customized generator loss function -

$$L_G^{total} = -E[D(x_{gen}, s)] + \lambda_{micro} \Big[MSE\big(\mu_{gen}, \mu_{real}\big) + 0.5\, MSE\big(\sigma_{gen}, \sigma_{real}\big) + 0.5\, RELU\big(\mu_{gen} - \mu_{real}\big)^2 + 0.3\, RELU\,\big(n_{real} - n_{gen}\big) + 0.2\, MSE\,\big(I_{gen}, I_{real}\big)\Big] + \lambda_{ssim}\big(1 - SSIM(x_{real}, x_{gen})\,\big) + \lambda_{fm} \textstyle\sum_i MSE(\mu_{real,i}, \mu_{gen,i}) \qquad (3.4.1)$$

where, D represents the discriminator and $x_{gen} = G(s, z)$ to generate image using the z noise vector and stress-strain sequence input s to the generator. μ_{gen} and σ_{gen} are the mean and standard deviation of the particle sizes in generated images, and μ_{real} and σ_{real} are the corresponding values for real images. n_{gen} and n_{real} are the number of particles in the generated and real images, respectively. Also, I_{gen} and I_{real} are the mean intensities of the generated and real images. $\mu_{real,i}$ and $\mu_{gen,i}$ are the mean feature maps of real and fake images at layer i in the discriminator. Lastly, λ_{micro}, λ_{ssim} and λ_{fm} are the weight of microstructure, SSIM, and feature matching losses, respectively.

In this transfer learning model applied to an experimental dataset, we used four combinations of datasets: 3D printed PDMS-glass fiber-glass particle hybrid composite, 3D printed PDMS-glass particle composite, casted PDMS-glass fiber-glass particle hybrid composite, and casted PDMS-glass particle composite. These experimental datasets were utilized for fine-tuning the model to generate microstructures that mimic the experimental conditions. We combined all four datasets, resulting in a total of 1,846 cases, each consisting of microstructure images and corresponding stress-strain data points. The dataset was split in an 80:20 ratio, with 80% (1,476 cases) used for training the model to learn structural characteristics conditioned on mechanical properties. The total training time was 57 minutes. The remaining 20% (369 cases) was further divided: 10% of the total dataset (185 cases) was used for validation to provide real-time feedback during training, and the final 10% (184 cases) was reserved for testing the model's performance on unseen data. Unlike previous transfer learning models based on simulated data, this model includes two different structural combinations. The hybrid composite contains cylindrical-shaped fibers and hollow circular particles, which are similar to the structures in the pretrained model, while the single fiber composite contains only hollow circular particles without cylindrical fibers.

3.5 FEA

To design microstructures with tailored full-range stress-strain curves, an AI-driven framework was used to address inverse S-P relationships. Since these frameworks rely on datasets, FEA simulations were conducted on defined composites to generate the data for the AI models. FE models were designed using Abaqus/CAE Standard/Explicit (Abaqus® v2023) to simulate the hybrid composites' mechanical characteristics. A two-dimensional finite element (FE) model of a hybrid composite material was developed, where the representative composite structure features a polydimethylsiloxane (PDMS) matrix measuring 0.4 mm × 0.6 mm (element type: CPE4R). Embedded within this matrix are reinforcing glass fibers, with lengths varying from 0.215 mm to 0.031 mm and a width of 0.015 mm, modeled using element type CPE3. Additionally, the composite contains glass particle fillers, with radii ranging from 0.049 mm to 0.02 mm, also represented by element type CPE3. This model enables a detailed analysis of the composite's mechanical behavior and interaction between the PDMS matrix and the glass-based reinforcements. To cover a broad dataset, the microstructure design parameters, including glass fiber length, width, fiber orientation, fiber spacing, volume fraction of fibers, glass particle radius, volume fraction of particles, particle spacing, and mesh sizes, were varied during simulations. The composite models were meshed using equal interval fine size control with a 2D solid quadrilateral free mesh due to the complexity of the structure. The final mesh sizes were set to 0.005 mm for the particles, 0.01 mm for the matrix, and 0.02 mm for the fibers in the composite model. The mesh convergence check was performed with five mesh sizes differing by around 2 times in sequence, namely 0.0025, 0.005, 0.01, 0.02, and 0.04 mm. For the uniaxial tension test simulations, a 2.5 mm displacement was applied on the top surface. The bottom plate was constrained in the y-direction to prevent vertical movement. A reference point was also created on the bottom plate where fixed x- and y-displacement boundary conditions were applied.

Additionally, 2D solid models of the epoxy-carbon fiber-glass particle and epoxy-glass fiber-glass particle hybrid composites were developed in FEA. In these models, the epoxy matrix dimensions were 0.4 mm × 0.6 mm with an element type of CPE4R, and the carbon fibers had lengths ranging from 0.05 mm to 0.2 mm and a width of 0.01 mm, with an element type of CPE3. Both models shared identical meshing and boundary conditions as the previously described PDMS-glass fiber-glass particle hybrid composites. For the uniaxial tensile simulations, a displacement of 0.3 mm was applied on the top surface to evaluate the failure criteria.

3.5.1 Material Properties

The matrix of the composites, PDMS, was defined as a 2D deformable solid using a hyper-elastic model in Abaqus. The Neo-Hookean model were utilized to represent the realistic hyperelastic/ rubber-like behavior of the matrix and its strain energy potential U in polynomial form[120] was applied.

$$U = \sum_{i+j=1}^{N} C_{ij} \, (\bar{I}_1 - 3)^i (\bar{I}_2 - 3)^j + \frac{1}{D_1} \, (J_{el} - 1)^2 \tag{3.4.1}$$

For the first-order Neo-Hookean form of the strain energy potential[120] (N=1), the stain energy potential reduces to

$$U = C_{10} \, (\bar{I}_1 - 3) + \frac{1}{D_1} \, (J_{el} - 1)^2 \tag{3.4.2}$$

where J_{el} represents the elastic volume ratio; I_1 and I_2 represents the first and second invariants of the distortion in the material; and N represents the order of the function. The C_{ij} define the shear behavior of the material, and the D_1 introduce compressibility. Based on previous experimental data, the key values of the shear behavior C_{10} are 0.16 and compressibility, D_1 of the material are 0.585 MPa.[120,121]

To define the failure characteristics of the matrix in the model, a tabular input of artificial plasticity and a failure drop of stress were determined based on the pseudo plasticity characteristics and back-propagation of experimental composite properties so that the FEA would terminate when the composites reached this failure stress to replicate the real failure in the experiments.[120,121] The stress-strain relationship of PDMS was shown in Figure 3.3(a).

In the FEA model, the epoxy matrix was assigned a Young's Modulus of 1580 MPa and a Poisson's ratio of 0.2.[122] To mimic the nonlinear mechanical responses and failure of the epoxy, a tabular artificial plastic strains and stresses were defined in the Abaqus to achieve a stress-strain relationship as shown in Figure 3.3(b). The FE models were created for glass fibers as 2D cylindrical deformable solids. Glass fiber properties were defined with a Young's Modulus of 60 GPa and Poisson's ratio of 0.3 for glass fiber. The carbon fiber properties were characterized by a Young's Modulus of 890 MPa and a Poisson's ratio of 0.2.[122] Glass particles were modeled as 2D circular deformable solids with a Young's modulus of 50 GPa and a Poisson's ratio of 0.45.

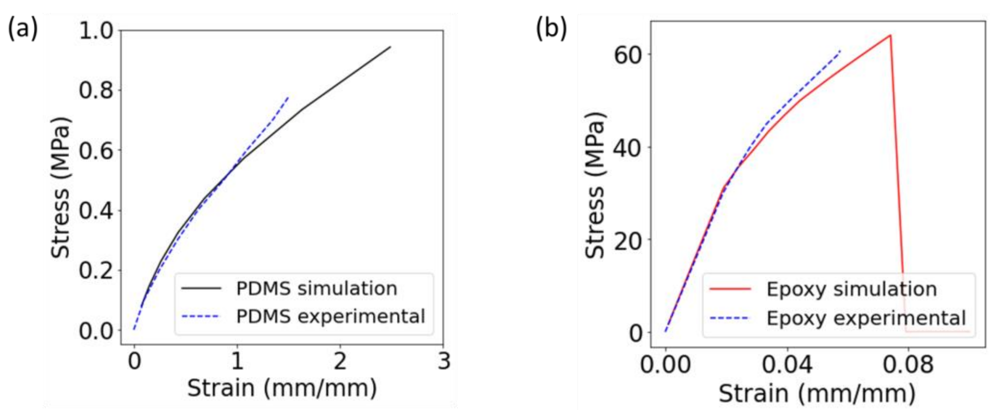

Figure 3.3: Stress-strain curve of simulated and experimental (a) pure PDMS and (b) pure epoxy materials.

For each simulation, the orientation of the glass fiber was varied at angles of 0°, 30°, 45°, 90°, and randomly. The volume fraction of glass fiber and glass particles also varied independently between 0 and 18 vol% for each type of filler. The carbon fiber orientation was varied among 0°, 45°, and 90°. The volume fractions of carbon fiber and glass particles were adjusted for each simulation, with carbon fiber ranging from 3%, 5%, 6%, 8%, 10%, to 12%, and glass particles from 3%, 6%, 9%, 12%, 15%, to 18%. Finally, the composite microstructure with corresponding force-displacement information was extracted after processing the simulation to investigate the mechanical properties further.

CHAPTER 4

CHARACTERIZATION OF HYBRID COMPOSITES S-P RELATIONSHIPS

4.1 Introduction

The advancement of 3D printing technology has revolutionized the creation and optimization of composite materials by enabling precise tailoring of their microstructures with enhanced mechanical properties like stiffness, toughness, and fatigue resistance. Achieving the desired mechanical properties is enabled by controlling the manufacturing processes which influences the geometry, density, and strength of fillers and matrices, along with their spatial distribution, orientation, and alignment. Furthermore, employing image-driven ML algorithms such as CNN proves beneficial in analyzing and predicting the behavior of these composites providing a deeper insight into their properties and performance. The current goal is to implement the CNN-based ML model to predict the mechanical properties from the experimental microstructure data, where it can effectively correlate the S-P relationships based on the local analysis of image features.

Here, we developed a composite mechanics model and an image-driven DL model to predict mechanical performances and understand the P-S-P relationships. Different from conventional statistical approaches, we utilized experimental microstructure data in the ML model to forecast the factual mechanical characteristics of the composite by taking into account local defects, texture, and other deviations affecting the properties. In this work, we 3D-printed a series of lightweight hybrid composites. The heterogeneously structured composites were formulated with soft hyper elastic polydimethylsiloxane (PDMS) as matrix and hybrid fillers of glass microfibers and hollow thin shell microparticles. The composites were 3D printed using an extrusion-based direct ink writing (DIW) method. Combining the hybrid fillers was simple yet efficient, providing us composite design freedom with density and mechanical properties varying nearly two-fold quickly. To understand the relationships between process parameters and mechanical properties, we conducted the Taguchi method and statistical analysis on the ink compositions, 3D printing parameters, and the resulting experimental tensile testing data to identify the significant parameters for mechanical strength and stiffness. A theoretical mechanics model for the hybrid composites was developed based on a Weibull analysis that combined multiple classical single-filler composite models, incorporating the fraction and spatial information of the fillers and the failure criteria for the hybrid composites. Distinguishing from the conventional approach, we used an image-driven CNN method to capture the microstructural details directly from optical microscopy images and predict the critical mechanical properties. The image-driven model outperformed our statistical and theoretical analysis compared with experimental data.[25]

4.2 Results & Discussion

The overview of this study is illustrated in Figure 4.1. Our work includes three parts, specifically (i) conventional statistical analysis using Taguchi and ANOVA, (ii) development of a hybrid theoretical mechanics model, and (iii) establishment of image-driven ML models. In the conventional statistical approach, we used the Taguchi method to optimize the number of experimental cases and ANOVA to quantify the contribution of several process parameters to the mechanical properties (Figure 4.1 (a)). Following that, a theoretical model for our hybrid composites was developed based on classical single-filler composites and Weibull distribution function (Figure 4.1 (b)). The mechanical behavior was explicitly correlated with the statistical structural parameters in this model. Finally, an image-driven CNN ML model was implemented to analyze the relationships between microstructures and mechanical properties to provide more accurate predictions for the 3D-printed hybrid composites (Figure 4.1 (c)).[25]

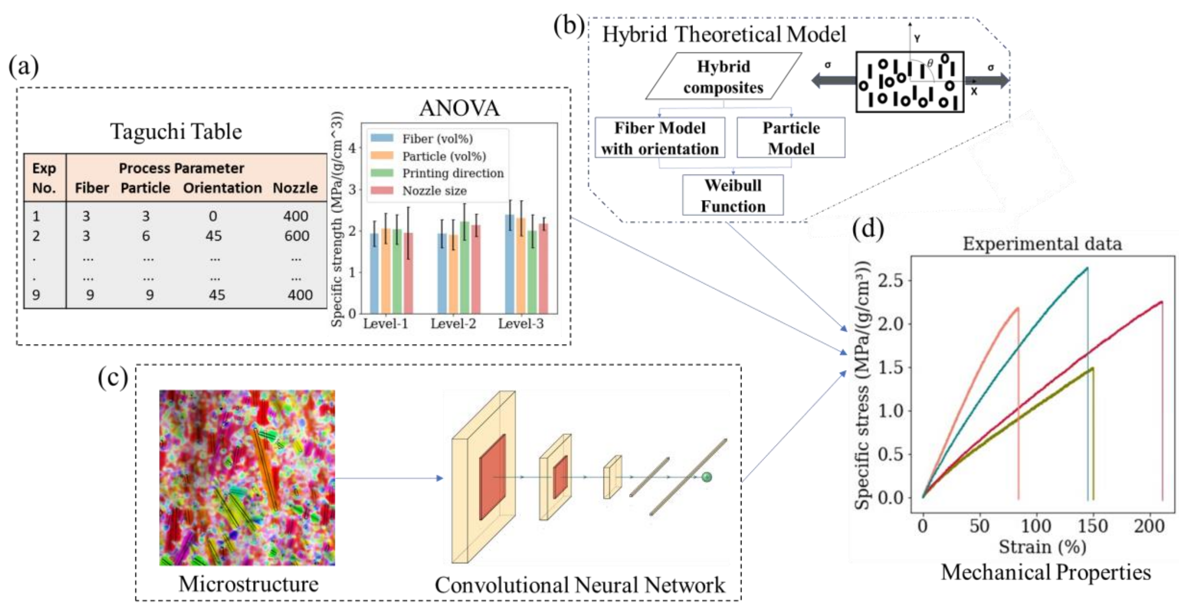

Figure 4.1: An overview of the framework in this study for the 3D printed hybrid composites investigation. This framework includes (a) conventional statistical approaches to the design of experiments to quantify the effect of manufacturing process variables on mechanical properties, (b) a hybrid mechanical model, and (c) an image-driven ML model to capture (d) the experimental mechanical behaviors.

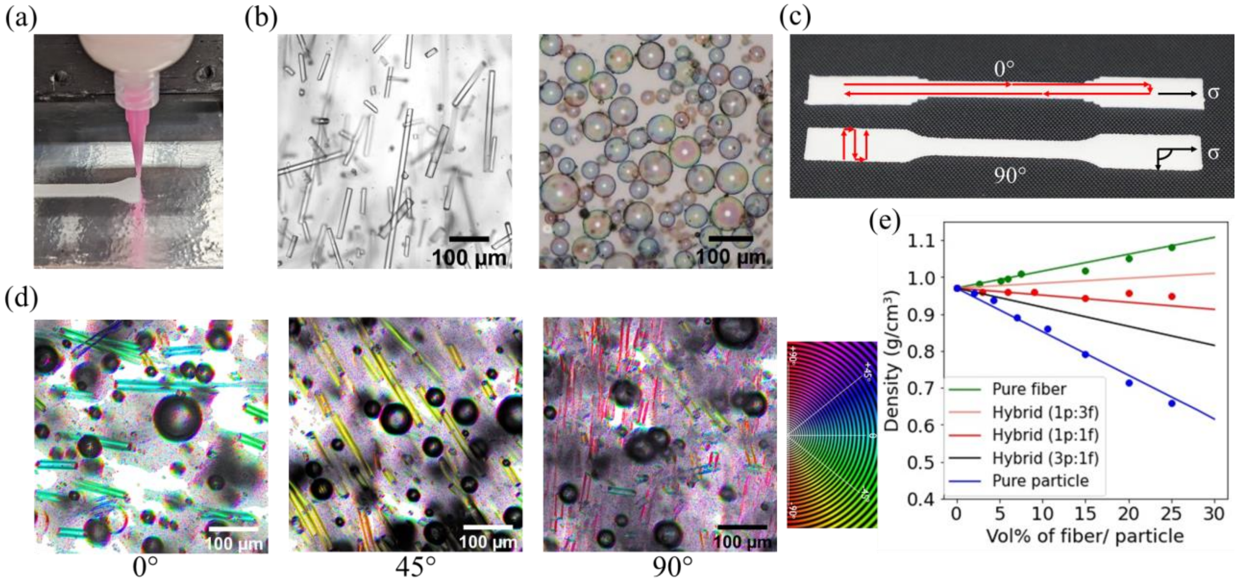

Figure 4.2: (a) 3D printing of hybrid composites into a tensile specimen using the DIW method, (b) fillers in the printed composites, including glass microfibers and glass thin-shell spherical particles, (c) 3D printed tensile specimens with 0° and 90° printing directions, (d) microstructures of 3D printed hybrid composites with 0°, 45° and 90° printing directions along with their color definition, and (e) the nominal density range of the hybrid composites via the combination of fillers at different volume fractions, where lines are the theoretical calculations and dots are 3D printed experimental validations.

To fabricate the hybrid composites, we used the DIW method, which was a material extrusion-based additive manufacturing technique, to 3D print specimens of various ink formulas and printing directions (Figure 4.2 (a)). The fillers used in this study are shown in Figure 4.2 (b), where the dimensions of the glass microfibers before mixing are 123.1±92.03 µm in length and 11.7±3.34 µm in diameter and the particle sizes are 47.8±1.33 µm in diameter with a shell thickness of 160±99.7 nm. The DIW method harnessed the rheological properties of the composite inks, specifically shear thinning and yielding (Fig. B.1 in Appendix B), to ensure smooth extrusion and retain shapes after printing.[31,123] More importantly, the shear effect between ink flow and the nozzle walls results in the alignment of the fillers along the printing direction.[31,124,125] By simply controlling the printing path direction (Figure 4.2 (c)), different orientations of microfibers in composites could be achieved, as shown in Figure 4.2 (d). The geometric anisotropy of the microfibers would lead to mechanical enhancement and anisotropic responses for the composites. At the same time, the hollow spherical glass particles could provide local strength enhancement and enable the design freedom for desired nominal density of the hybrid composites. By tuning the volume fractions of the hybrid fillers, Figure 4.2 (e) shows the design space of the theoretical composite density (lines) and experimental validations of 3D printed samples (dots). Due to the low nominal density of 0.13 g/cm^3 of the thin-shell particles, the density of the hybrid composites could vary more than 70%, potentially enabling lightweight applications like energy absorption and protective coatings.

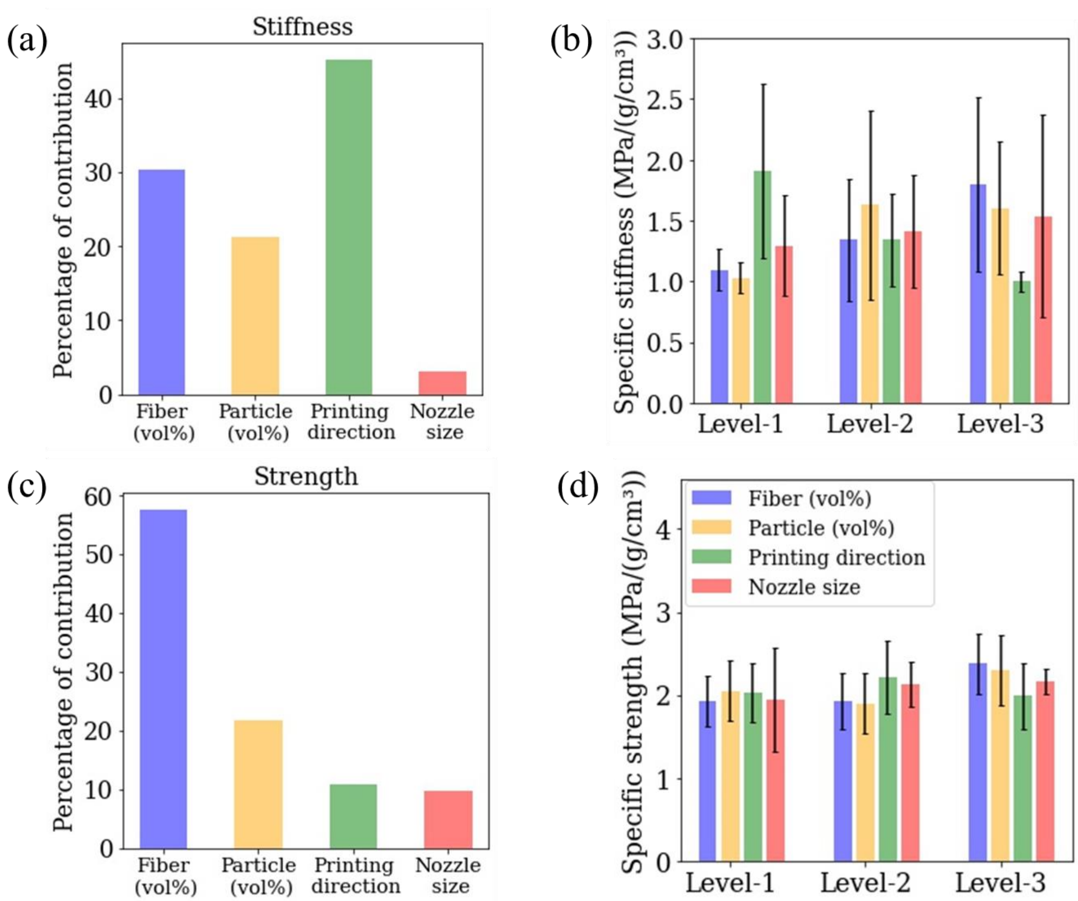

Figure 4.3: The effect of process parameters on the mechanical properties of hybrid composites. (a) Percentages of contribution and (b) Taguchi analysis for process parameters on specific stiffness, (c) percentages of contribution, and (d) Taguchi analysis for specific strength at different levels of process parameters.

To understand the correlations between the process parameters and mechanical properties, we first utilized the statistical Taguchi analysis and ANOVA. Tensile specimens were 3D printed in 9 cases with printing conditions listed in the Taguchi orthogonal array (Table 3.2) and were used to collect mechanical properties from tensile tests. Figure 4.3 illustrates the ANOVA results of the contribution percentages of four process parameters and specific stiffness and strength at different levels of these parameters. For stiffness, the printing direction had the highest percentage of contribution (45.3%) compared to the other three parameters (Figure 4.3 (a)). In addition, the stiffness for each level of process parameter was calculated using the Taguchi table (Table 3.1) in Figure 4.3 (b). For printing direction, the stiffness was increasing 91.1% from level 3 to level 1, where the level 3 represents the printing direction of 90°, and level 1 represents 0°. The stiffness changes for the fiber volume fraction from level 1 to level 3 significantly increased by 64.3%, where level 1 represents 3 vol% of fiber and level 3 represents 9 vol%. For the volume fraction of particles, the stiffness improved by 55.9% from level 1 to level 3, representing the 3 and 9 vol% of particles.

Figure 4.3 (c) illustrates the percentage of the contribution of each process parameter to the strength properties. And the tensile strength for each level of process parameters is visualized in Figure 4.3 (d) using the Taguchi table (Table 3.1). For the volume fraction of fibers, the average strength increased by 23.1% from level 1 (3 vol% fibers) to level 3 (9 vol% fibers). The average strength increased by 12.13% for the increasing volume fraction of particles from 3 to 9 vol%. The changes in strength and stiffness for nozzle sizes were determined as insignificant via an F-test (Table B.1 and B.2 in Appendix B). The volume fraction of fibers dominated the percentage of contribution (57.64%) to the strength of the 3D printed hybrid composites.

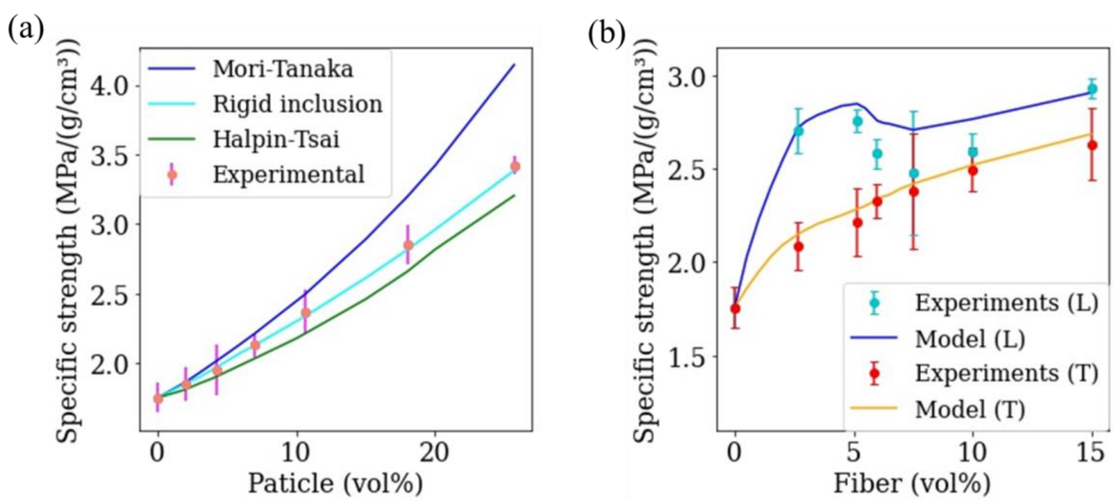

Figure 4.4: Comparison of theoretical models with experimental data for single-filler composites. The specific strength of (a) glass particle reinforced composites for different volume fractions of particles using three different mechanics models and experimental data, and (b) glass fiber reinforced composites for different volume fractions of fibers with longitudinal (L) and transverse (T) fiber orientations using Halpin-Tsai fiber model and experimental data.

To further quantify the P-S-P relationships, we developed a theoretical mechanical model to establish the properties based on the process parameters explicitly. Before getting the model for hybrid composites, we performed experimental validations on selecting multiple classical analytical models for single-filler composites (Appendix A). For the particle models, we used rigid inclusion, Mori-Tanaka, and Halpin-Tsai mechanics models based on Eq. (A.3), (A.4), and (A.5), respectively.[41,126–129] For the fiber models, we applied the rule of mixture, the Halpin-Tsai model, and the Tsai-Hill criterion to consider different fiber dimensions and orientations using Eq. (A.6).[47,130–132] In Figure 4.4 (a), we observed that the Mori-Tanaka particle model depicted an upper bound, and the Halpin-Tsai particle model was the lower bound.[128,130] The rigid inclusion model aligned well with the experimental specific strength data, which increased linearly with particle volume fraction. For fiber-reinforced composites (Figure 4.4 (b)), the composites with transversely oriented fibers had less specific strength than the longitudinal ones. For all the cases, the specific strength depended mainly on the fiber sizes, which were highly correlated with the volume fraction of fiber[24] and the Halpin-Tsai and Tsai-Hill criteria fitted well with our experimental data.

We developed a mechanics model for 3D printed composites with hybrid fillers based on the single-filler composite models. A Weibull probability density function was used to incorporate the effect of microfibers and spherical particles on the specific strength.[133]

$$\sigma_c = \sigma_{c_f} P_{cf} + \sigma_{c_p} P_{cp} \tag{4.2.1}$$

with

$$P_{cf} = 1 + e^{\left(-\frac{l}{l_{cr}}\left(\frac{\sigma_{c_f}}{\sigma_{crf}}\right)^{m_1}\right)} \tag{4.2.2}$$

and

$$P_{cg} = 1 + e^{\left(-\left(\frac{\sigma_{c_p}}{\sigma_{crp}}\right)^{m_2}\right)} \tag{4.2.3}$$

where σ_{c_f} is the strength of fiber composite, σ_{c_p} is the strength of particle composite, and l is the length of the fiber. σ_{crf} and σ_{crp} are the critical strength of fiber-matrix and particle-matrix interfaces, and l_{cr} is the critical length of fiber associated with the critical strength σ_{crf}. The key parameters to calculate the stress for hybrid models in Eq. (4.2.1) are the critical strengths of the filler-matrix interface, the critical length of fibers, and the variable m_1 and m_2 calculated using the weight function.[134] The strength of fiber and particle were calculated using the Mori-Tanaka and the Halpin-Tsai models combined with Tsai-Hill criterion formulas (Eq. (A.4) and (A.6)), respectively. The detailed derivation of the hybrid model is in Appendix A.3.

Based on the hybrid model of Eq. (4.2.1), the specific strength of the composites was determined and compared with the experimental results shown in Figure 4.5. Figure 4.5 (a) and 4.5 (b) depict that the hybrid model captured the overall trend in the different cases, but with a propensity to overestimate the experimental results. The overestimation in the hybrid model is because the statistical method disregards the structural details and has idealized assumptions without making allowances for experimental uncertainties, such as voids, geometric imperfection, and filament waviness during 3D printing.[124]

To address the challenges above and provide better predictions, we harnessed a predictive image-driven CNN ML model to directly predict the critical mechanical properties using the microstructure of the hybrid composites. Using CNN, we predicted the hybrid composites' stiffness, strength, and toughness from the composite's microstructures shown in Figure 4.6. The microstructural data contained detailed information, like volume fraction of fillers, shape, and sizes of fillers, geometric imperfections, inter-filament gaps, etc., to correlate with the mechanical properties, allowing the ML model to provide better predictions with higher accuracy.

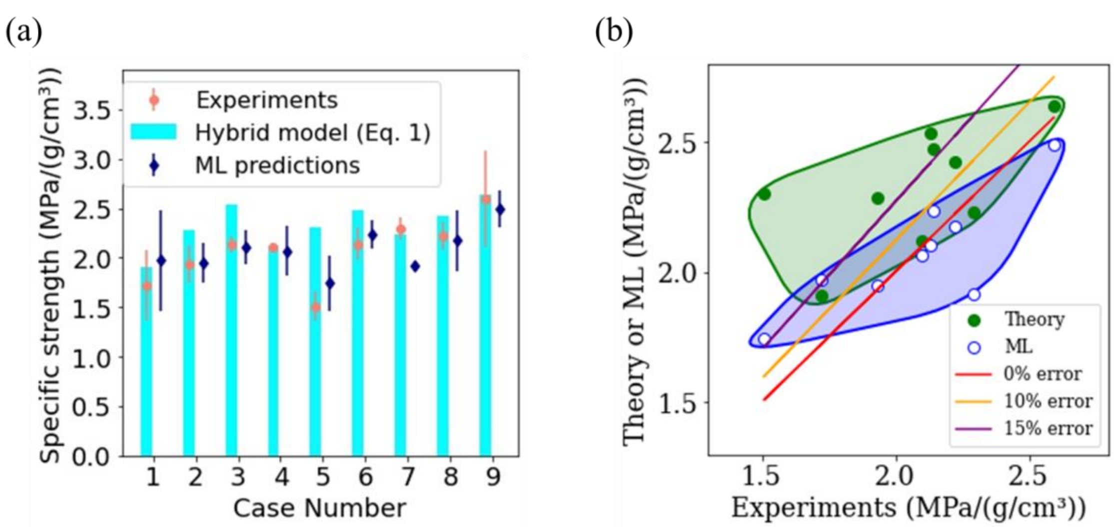

Figure 4.5: (a) A comparison between the hybrid mechanics model, the experimental data, and the ML model prediction results of the specific strength of the hybrid composites, and (b) an Ashby plot of ML model predictions and the hybrid mechanics model of specific strength against experimental data.

Figure 4.5 (a) compares the experimental data, hybrid mechanical model results, and the CNN prediction results of specific strength. The ML prediction data showed close values against the experimental data. Error bars were associated with ML results since the specimens in each case (8-9 specimens in each case) had different local microstructures, which were fully considered in the ML model rather than being ignored or summarized in a statistical way as in the theoretical models. Rather than collecting an extensive dataset, our ML model required a minimal dataset of 616 images from 77 specimens for training. This saved much experimental effort and resulted in much higher accuracy. In Figure 4.5 (b), an Ashby plot compares the theoretical model and ML model results of the mechanical strength of the hybrid composite to the experimental results. The error represents the waviness of the filament surface during 3D printing, which can be quantified through statistical measurement. The waviness is caused by variations in microstructure, processing conditions, and material composition. The error is defined in Eq. (4.2.4).[124]

$$\sigma_e = \sigma_{exp}(1 + 6e^2) \tag{4.2.4}$$

Here, e is the experimental error, σ_{exp} and σ_e is the experimental strength and strength caused by the experimental waviness. In Figure 4.5 (b), the red straight line indicates a perfect prediction with 0% experimental error, whereas 10% and 15% error represents the 10% and 15% experimental error due to the waviness. However, as expected, the waviness error is associated with statistical measurements and cannot explicitly define the local uncertainties. The theoretical model overestimated the strength, whereas the ML model data showed more accurate results with a Pearson's correlation coefficient 37.5% higher and a root mean square error (RMSE) 48.6% lower.

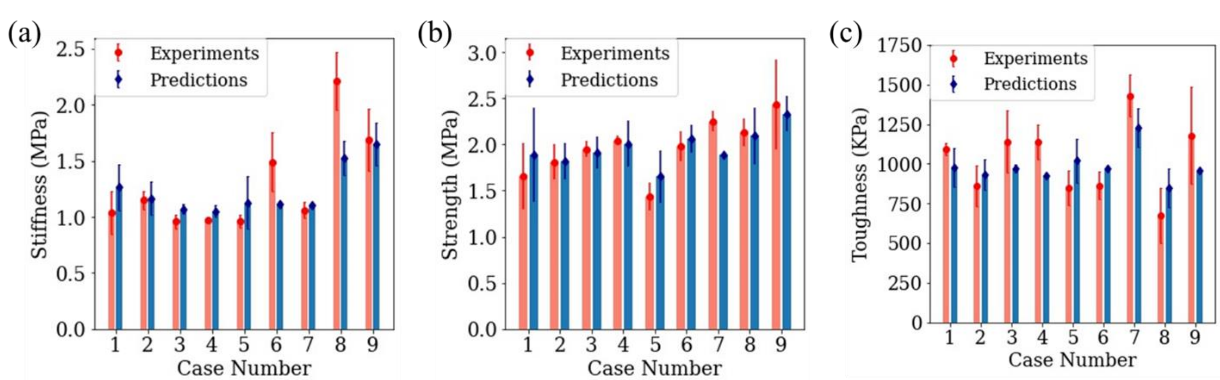

Figure 4.6: Incorporating image-based convolutional neural networks in the prediction of the (a) stiffness, (b) strength, and (c) toughness properties of the 3D printed hybrid composites.

Two demonstrations of impact and drop tests using the 3D printed hybrid composites and pure PDMS are shown in Figure 4.7. Both materials were 3D printed into a film shape with identical weights. Our drop tests used a dropping weight (5 lbs.) from the same height (7.62 cm) onto a plastic 'egg' sandwiched by hybrid composites and pure PDMS, respectively. The pure PDMS-protected eggs were broken into pieces (Figure 4.7 (b)). In contrast, the hybrid composite protected eggs had minimal damage on the top (Figure 4.7 (a)). In the impact test demonstrations, a high-speed rubber bullet hit the center of a thin rectangular plate of pure PDMS or hybrid composite at a constant speed of 1.43 m/s. The impact resulted in a deformation of the pure PDMS film of 6.9 mm, which was 62.7% larger than the hybrid composite film (4.24 mm), as shown in Figure 4.7 (c)-(d). Both demonstrations showed the advantages of mechanical efficiency in energy absorption and deformation rigidity for our 3D-printed hybrid composites.

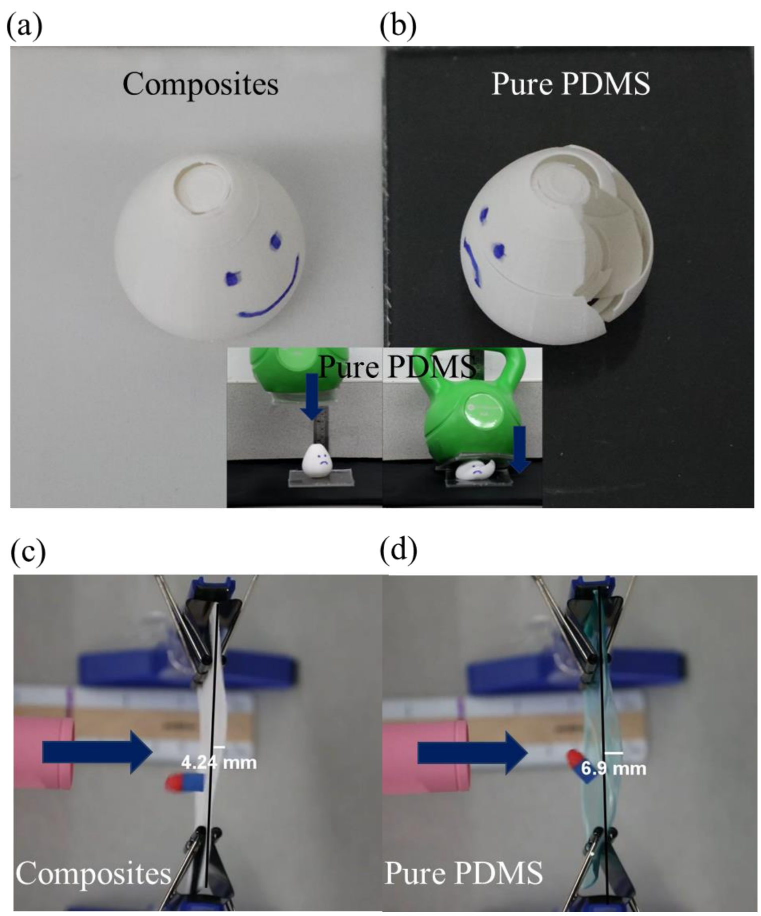

Figure 4.7: Demonstrations of dropping tests using (a) the 3D printed lightweight hybrid composites and (b) pure PDMS films in protecting a plastic egg, and impact tests using (c) the hybrid composites and (d) pure PDMS films with identical weights.

4.3 Conclusions

We have developed 3D printable lightweight hybrid composites and investigated their P-S-P relationships using conventional statistical approaches, theoretical modeling, and an image-driven CNN method. The hybrid fillers of solid micro fillers and hollow particles provided greater degree of freedom in structural designs with reduced density and increased properties. Our statistical analysis determined the dominant parameters as the printing direction (contribution percentage of 45.3%) and the volume fraction of fibers (contribution percentage of 57.7%) on the specific stiffness and strength, respectively. A hybrid mechanics model was developed in this study, harnessing a simple Weibull distribution function and classical single-filler models. This model could effectively capture the trend of the mechanical properties in different conditions but overestimated experimental results in general because the experimental local uncertainty was not considered in the model. The image-driven ML model predicted more accurate results with 48.6% lower RMSE than the hybrid theoretical model.

CHAPTER 5

DEVELOPMENT OF MICROSTRUCTURAL DESIGN OF HYBRID COMPOSITES

5.1 Introduction

Investigating inverse S-P relationships in lightweight hybrid composites is crucial for designing customized products by focusing on microstructure manipulation to optimize mechanical properties like strength and ductility. However, achieving these tailor-made properties presents challenges like poor interfacial bonding, filler agglomeration, and complicacy of other additive manufacturing variables. To address these issues, computational models and artificial intelligence offer promising solutions by modeling complex relationships between material structure and properties. DL, through neural networks, and computational methods like the FE method enable detailed analysis and prediction of material behavior under various conditions leading to optimized designs. Though gaps remain in inverse design and data availability for microstructures and their associated properties, the use of experimental characterization, along with computational and data-driven models, will provide substantial support in understanding these relationships.

This study introduces a novel computational framework that integrates FEA with Conditional Generative Adversarial Networks (cGAN) to develop tailored microstructural designs for hybrid composite materials. A DL model was trained on FEA generated dataset to recognize complex patterns and customize microstructures in line with their mechanical behaviors. The AI-generated microstructures demonstrated strong feature similarity with the original microstructures for target full-range stress-strain curves. The low Fréchet Inception Distance (FID) scores further indicated high fidelity and precision in accurately replicating intricate material structures. The full-range stress-strain curves derived from AI-generated microstructure matched well with the original stress-strain curves that were target for. Additionally, we implemented transfer learning techniques to refine the model further to encompass different materials.

5.2 Results and Discussion

The overview of this study is depicted in Figure 5.1, outlining the framework for generating custom-made microstructures based on specific properties. This framework is divided into three primary components: (a) the data generation step, (b) a Deep Learning (DL) model, and (c) a transfer learning model. Initially, a simulation method is employed to generate a dataset of composite microstructures along with their corresponding mechanical properties, aiming to replicate experimental results. Subsequently, the dataset is used within a DL model to train and assess the model's performance in predicting tailored microstructure designs. Lastly, a transfer learning model is implemented to transfer knowledge from the previous model, refining the new model to adapt to a new dataset focused on rigid materials.

A comprehensive dataset was generated through FEA to investigate the inverse S-P relationship of elastomer-based hybrid composites by varying a defined set of parameters, as illustrated in Figure 5.1 (a). By modifying the design parameters, diverse microstructures of hybrid composites composed of PDMS, glass fibers, and glass particles were produced through simulations, accompanied by their corresponding full-range stress-strain data.

Then, we employed a DL framework, integrating a cGAN model with LSTM layers, designed to capture the intricate patterns of microstructures and correlations within the data. Here, the full-range stress-strain curves of the hybrid were used as input labels for the model. In contrast, the composite microstructures (images rather than statistical numerical data) were target-generated outputs. The cGAN model interpreted stress-strain curves as sequences of interconnected coordinates, with each data point containing a pair of stress and strain values, denoted as (x_i, y_i). This approach created a chain-like labeling system where the values of each coordinate were informed by its predecessor's points to reflect the continuous nature of the stress-strain curves of composite materials. The Figure 5.1 (b) schematic illustrates a detailed framework of a cGAN model developed to synthesize realistic, tailored microstructures informed by sequential stress-strain data. The generator was trained with stress-strain data and a noise vector to produce realistic microstructural images. At the same time, the discriminator simultaneously learned to distinguish real from synthetic images, driving the generator to create increasingly accurate representations of composite microstructures over time. The training phase was considered complete when the discriminator could no longer reliably differentiate between real and unrealistic microstructures. Figure 5.1 (c) shows the transfer learning model based on a pre-trained cGAN model implemented on different material combinations. The transfer learning model was trained and fine-tuned using the previously trained model's weights with updated hyperparameters for both the generator and discriminator to learn new material combinations' microstructures and stress-strain properties.

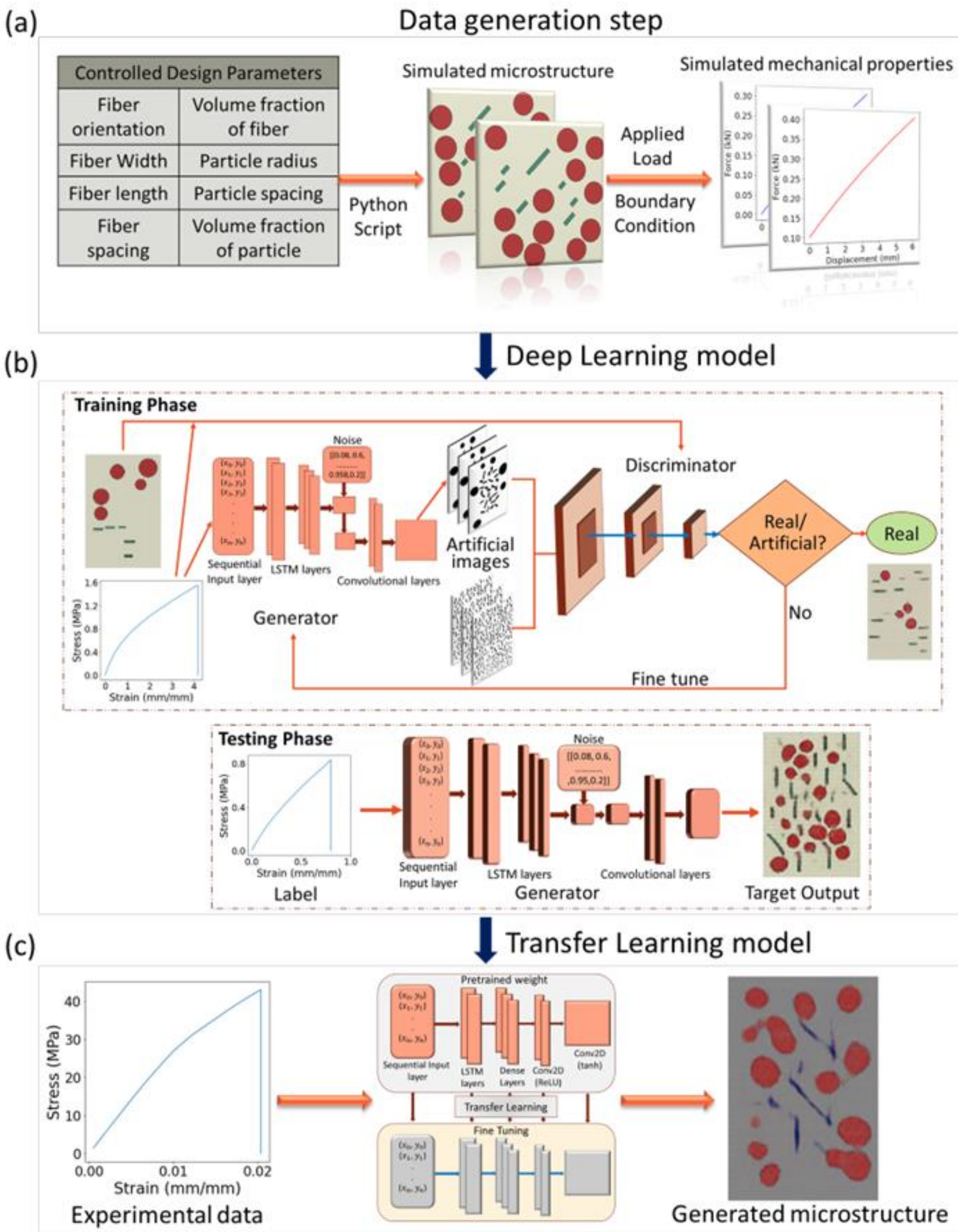

Figure 5.1: Schematic of the generation of tailored microstructures from full-range stress-strain relationships. The framework includes (a) data generation of microstructures and their corresponding stress-strain curves by systematically varying structural parameters, (b) a DL model trained with hybrid composite microstructures and stress-strain relationships, as well as testing the model's ability to generate microstructures using stress-strain relationships, and (c) applied transfer learning to fine-tune models to generate microstructures for different materials combinations of hybrid composites.

To gather a substantial dataset from simulations, the S-P relationships of pseudoplastic composites was simulated by varying a selected set of parameters. The impact of extreme cases was also examined to determine the maximum filler volume fraction and the mechanical property ranges. In Figure 5.2, the strength spanned from 0.7 to 2.2 MPa, the initial stiffness spanned 0.5 to 1.17 MPa, and the toughness 0.59 to 2.15 MPa for pure-PDMS to the hybrid composite. For the hybrid composite, up to 9% volume fraction of fiber and 18% volume fraction of glass particles were integrated into the plastic composite during the simulation process. The simulation method was also refined by updating the material properties to encompass both plasticity and hyper-elasticity of the material. Furthermore, additional analyses were performed to consider any experimental anomalies, including failure characteristics. By comparing with experimental data from fiber-reinforced composites, the failure characteristics observed in simulations were validated which ensured the reflection of practical conditions accurately.

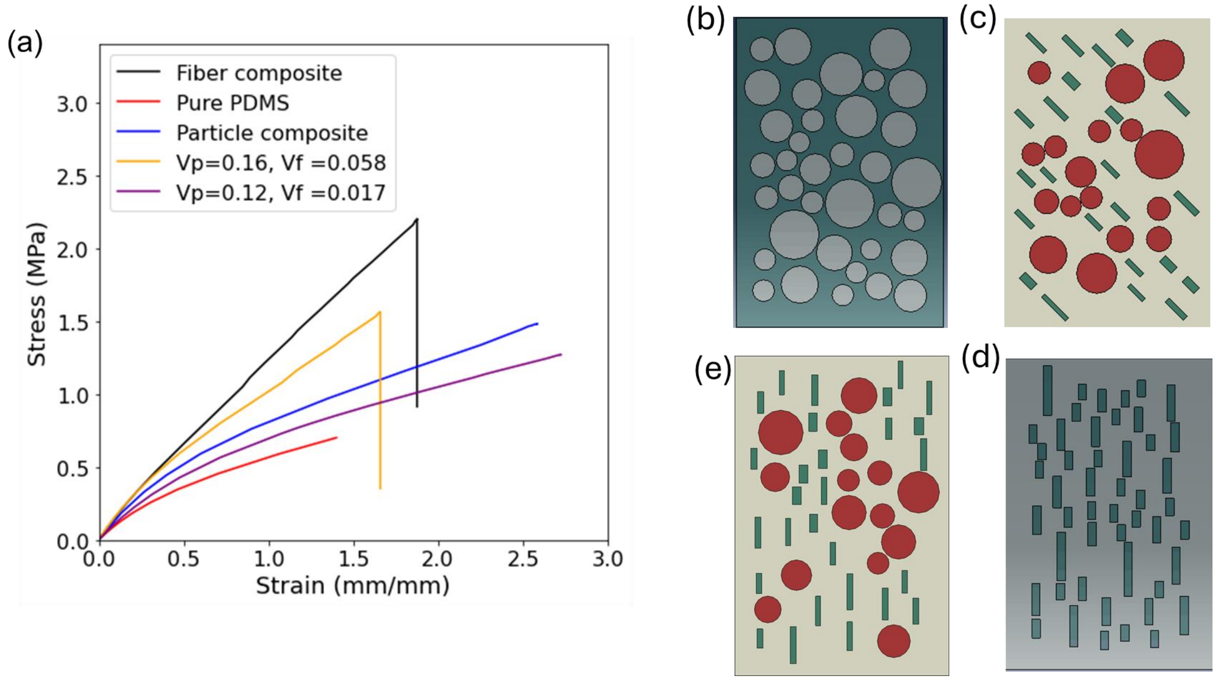

Figure 5.2: Inverse S-P relationships. (a) Stress vs Strain relationship along with the microstructure of the (b) 25% volume fraction of particles composite, (c) combination of 5% volume fraction of fiber and 16% volume fraction of particle composites, (d) 12% volume fraction of fiber composite, (e) combination of 1.7% volume fraction of fiber and 12% volume fraction of particle composites.

A specific example is given in Figure 5.3 (a), where a hybrid composite with an original microstructure of 4 vol% of well-aligned glass fibers and 18.5 vol% of glass particles was used. The stress-strain curve was collected from FE simulation based on this microstructure. The stress-strain data was subsequently used as input for the cGAN model's generator to produce the AI-generated microstructure. Note that the stress-strain curve was the only input, and no information of the original microstructure was provided to the cGAN model in the testing phase. From the generated microstructures, key features of particles and fibers were identified. The generated microstructure was then imported into the FE simulation to obtain its stress-strain curve. The generated microstructure and its stress-strain curve were later compared with the original microstructure and input stress-strain data. The comparison between the input stress-strain data used in the cGAN model and the stress-strain data derived from the generated microstructures demonstrated a close matching over the strain range. The results showcased the model's accuracy and proficiency in replicating complex material patterns as well as establishing inverse S-P relationships. Several more cases are exemplified in Figure 5.3 (b). Additionally, the image-driven model relied on geometric features rather than color contrast. A grayscale images trained cGAN model demonstrated this in Figure 5.3 (c). The models, either trained on colored or grayscale microstructural images, showed comparable performance on the test dataset with a low Fréchet Inception Distance (FID) score of 0.577 and 0.457, respectively. The FID score measures the similarity between images by comparing the distributions of feature representations. A lower FID score indicates higher similarity.[135] In other categories of material and image-based ML models, FID scores range from approximately 1.48 to 29.22.[135] In some cases, an FID score of less than 5 is considered high-generation quality.[136,137] In our cGAN model results, the FID score is below 1, which suggests that the model is robust enough to generate microstructures irrespective of the color of the microstructures.

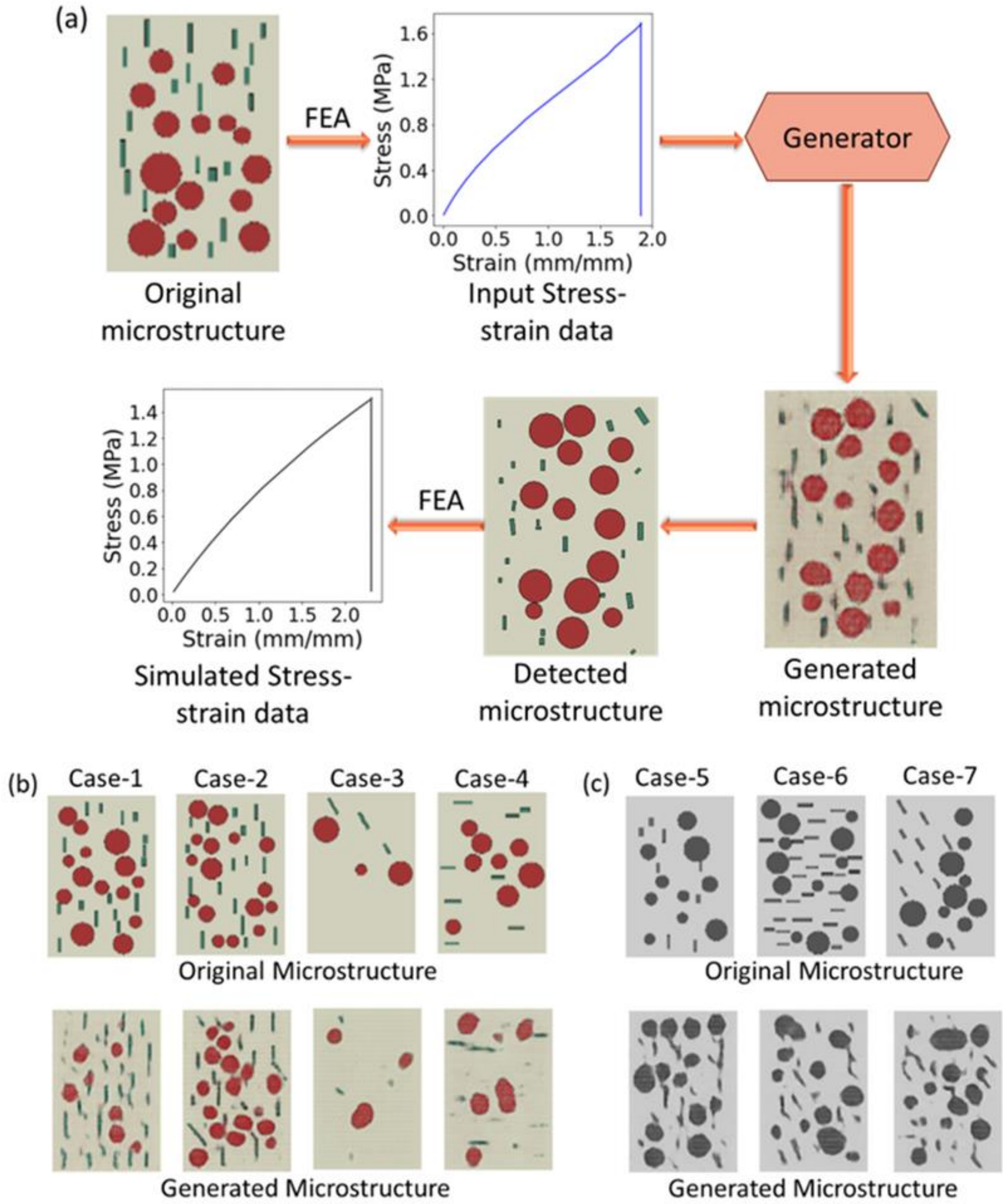

Figure 5.3: (a) An example of cGAN model generated composite microstructures using stress-strain data as input and comparing them with original composite microstructures. The cGAN model generated (b) color microstructures and (c) grayscale microstructures from stress-strain data, and the corresponding original microstructures.

For further analysis of composite microstructural features, we compared the volume fraction of filler in the original and generated microstructures across 32 cases. Figure 5.4(a) presents a statistical comparison of particle volume fractions across different cases. The data points are mainly concentrated around the zero line, indicating of minimal deviation between the original and generated microstructures. The standard deviation of the particle volume fractions between the AI-generated microstructures and the original ones was ±3.39%, as highlighted in the yellow shaded region in Figure 5.4 (a).

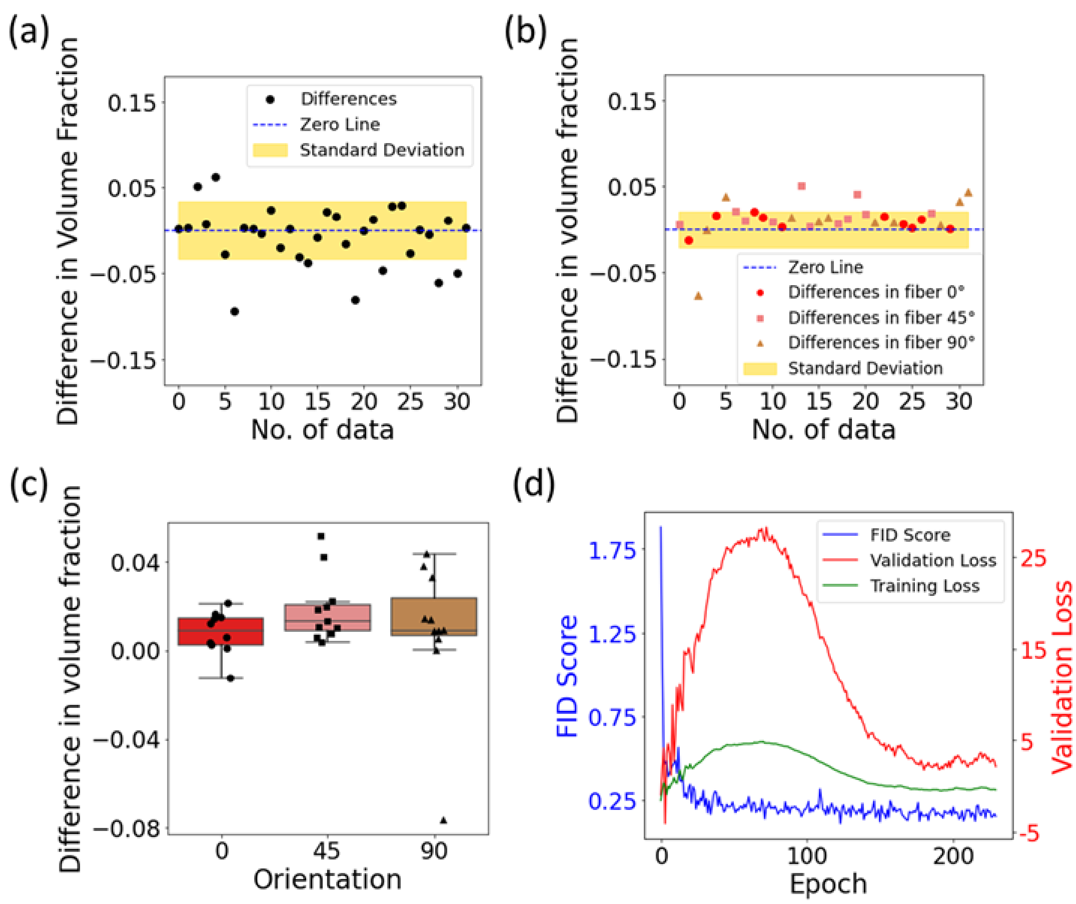

Figure 5.4: (a) Statistical analysis and comparison between the volume fraction of particles in original and generated microstructures. (b), (c) Statistical analysis and comparison between the volume fraction of fibers in original and generated microstructures at different fiber orientations. (d) DL model data validations by the losses on training, validation data, and FID scores.

Figure 5.4 (b) compares the differences in fiber volume fraction across three distinct fiber orientations: 0°, 45°, and 90°. Most data points are clustered around the zero line and within a standard deviation of ±2.09%. Figure 5.4 (c) further compares the differences in volume fraction between the generated and original microstructures across the three fiber orientations. Although a few outliers were present in the 45° and 90° orientations, the results suggested a consistently minimal difference in volume fraction across different fiber orientations. Figure 5.4 (d) illustrates the training progression of the cGAN model over 250 epochs, focusing on three key metrics: FID score, validation loss, and training loss.35 On the validation dataset, the FID score started with a high value of 1.88. It converged quickly to a low value at 0.21±0.07 as the training progressed over more epochs with better generation quality. The validation loss increased rapidly to its peak around epoch 75, then declined and stabilized after epoch 160. The training loss showed a lower score than validation loss of all epoch numbers and converged around epoch 150. The convergence of training loss and validation loss stabilizes at low values and improves model performance.

More importantly, we evaluated the full-range stress-strain curves calculated based on the AI-generated microstructure results and compared them with the target input stress-strain curves (Figure 5.5). We have utilized Multi-Criteria Decision Analysis (MCDA)[138–140] to provide a robust means of quantifying prediction accuracy and identifying the instances of higher deviations based on multiple conflicting criteria. The evaluation of mechanical property predictions for generated microstructures was conducted using a weighted function combining normalized R^2 score and RMSE, Score= $0.9 * R^2 - 0.1 * RMSE$, was used. We have defined the evaluation criteria by assigning a higher weight to R^2 (90%) compared to RMSE (10%), emphasizing the importance of capturing the overall variance explained by the model (R^2) over the absolute error magnitude (RMSE). This decision prioritizes the model fit with accuracy while balancing goodness-of-fit and error tolerance in evaluating overall microstructure performance. The R^2 score captures the proportion of variance explained by the model, while RMSE reflects the magnitude of error in the predictions. The results were categorized into three groups based on the quadratic normalization of the combined scores: high score performance (Score > 0.5), low score performance (Score < -0.5), and medium score performance (between -0.5 and 0.5).

Multiple examples are shown in Figure 5.5 (a) for the three groups. For high score cases, the AI-generated microstructure results (stress-strain curves) and the target stress-strain curves matched almost perfectly with high scores. For medium score cases, there were reasonable matches but variation at high strain regions near failure. The low score cases exhibited close stress-strain relationships at the initial strain region and deviated from target curves with increasing strain. An observation was that the target stress-strain curves in the low score cases failed at much smaller strains than the other two groups. During training, the stress value was set as zeroes after failure till the maximum value of strain of all training data. This might generate bias due to the large amount of zero values and cause errors in judging failure strains for these low failure strain cases. Another possible factor could be the loss of certain imperfect filler features during the AI-generated microstructure detection process. As a result, although the AI-generated images included all necessary features to produce similar full-range stress-strain curves in simulations, the imperfect feature representation led to a mismatch in smaller strain cases.

Figure 5.5 (b) uses colored regions to visually present the distinction between the performance levels, highlighting the distribution of high (green region), medium (blue region), and low score (red region) cases of the AI-generated microstructures. The plot shows that 88% of the cases fall within the high and medium scores categories, indicating a reasonably high efficiency in the inverse microstructure design for a target full-range stress-strain curve.

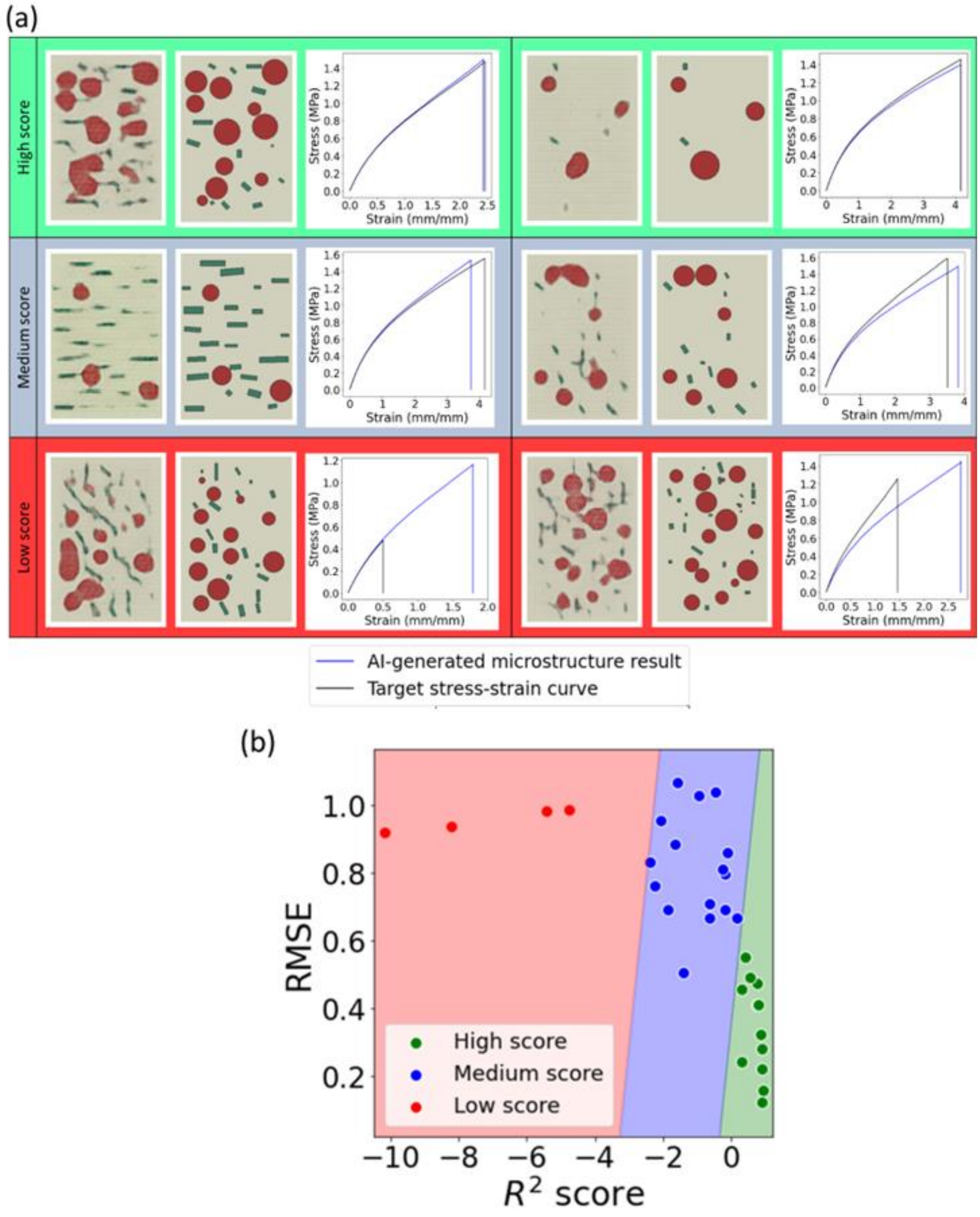

Figure 5.5: (a) Examples of AI-generated microstructures and their mechanical behaviors compared with the target stress-strain curves. (b) Distribution of the performance of example cases with respect to their R2 score and RMSE. A statistical score indicated the colored regions to quantify the prediction accuracy.

Furthermore, based on the established DL model of the elastomer-based composites, we employed a transfer learning approach to expand the ability to design and establish inverse S-P relationships for other composites. The model does not require training from scratch for each new material in transfer learning. Instead, it utilizes a pre-trained model, which has already learned essential structural and mechanical characteristics. It fine-tunes this model to accelerate and enhance the learning process for new materials (Figure 5.1 (c)). This method reduces the need for extensive data for each new material. It allows the model to generalize across different materials, from flexible and stretchable composites (PDMS-based elastomer composites) to stiffer and brittle composites (like epoxy-based composites).

Figure 5.6 represents the generated microstructures using transfer learning techniques based on the stress-strain behaviors of two hybrid composites: epoxy-carbon fiber-glass particle composites and epoxy-glass fiber-glass particle composites, with controlled design parameters. We utilized the pre-trained model, which had been trained on similar structural fillers but with much more compliant and deformable materials. The mechanical properties of the epoxy-carbon fiber-glass particle and epoxy-glass fiber-glass particle composites were more than 10 times higher in ultimate strength and over 67 times lower in failure strain compared to the pre-trained model's dataset for PDMS-based composites.

Our base model, a customized LSTM-cGAN was used as the pre-trained model, and its parameters were fine-tuned to train a new model for the above mentioned datasets. Figure 5.6 (a) and Figure 5.6 (b) depict two distinct cases of the original microstructures used in the training process, alongside the microstructures generated by the fine-tuned model. These generated microstructures are based on the stress-strain behavior characteristic of the epoxy-carbon fiber-glass particle composite. During the testing phase, the fine-tuned model generates tailored microstructure based on provided stress-strain curves. After fine-tuning, the model exhibited a low FID score on this composites' validation dataset (0.214) and test dataset (0.281). Similarly, for the epoxy-glass fiber-glass particle composite, the FID score was 0.182 on the test dataset.

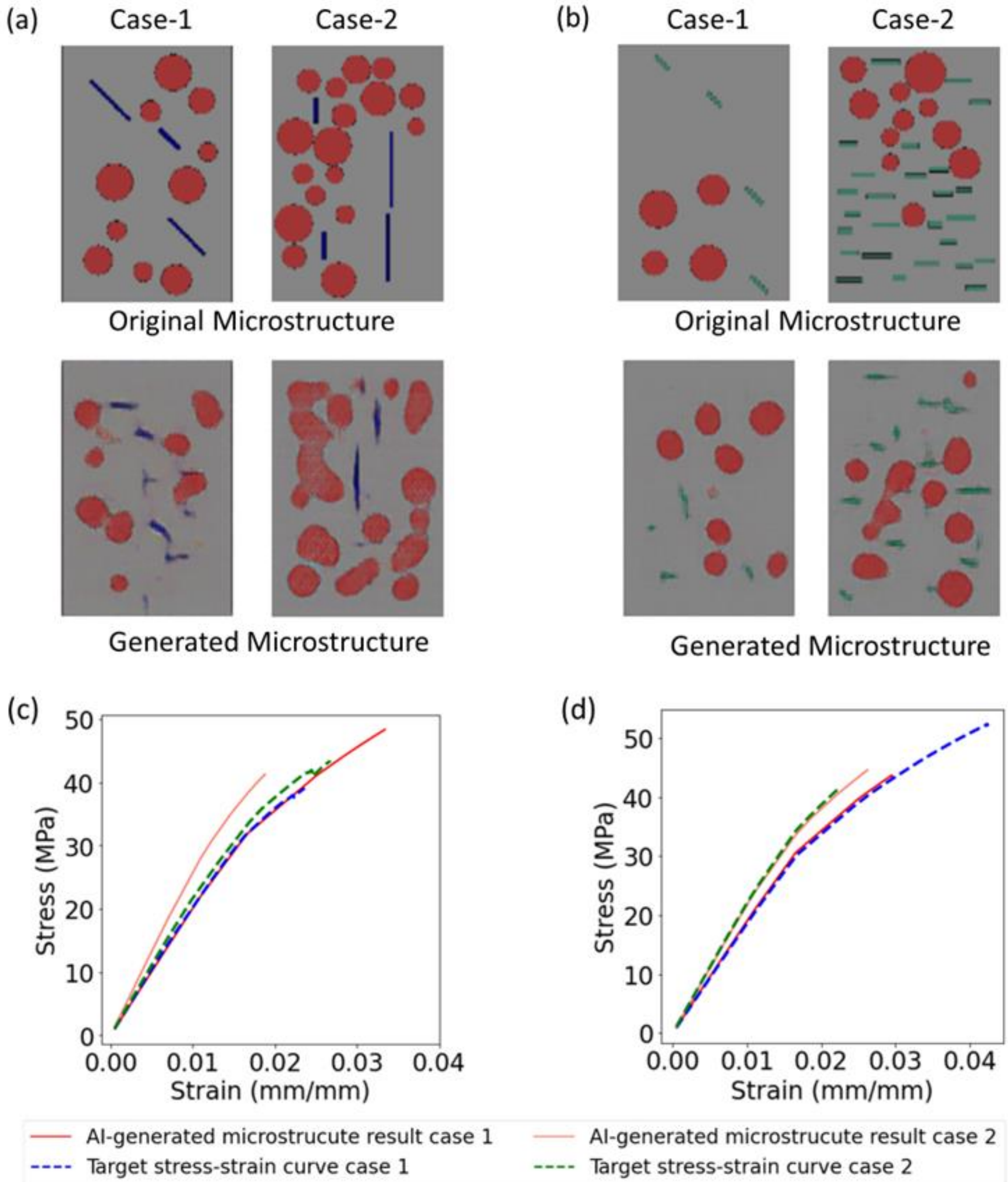

Figure 5.6: (a), (b) The generated microstructure using transfer learning was compared with original microstructures and (c), (d) comparison of the AI-generated microstrucutre results and target stress-strain properties of hybrid epoxy-carbon fiber-glass particle composites and epoxy-glass fiber-glass particle composites.

Figure 5.6 (c) and Figure 5.6 (d) compare the AI-generated microstructure results with the target stress-strain curves for two different cases: the epoxy-carbon fiber-glass particle composite and the epoxy-glass fiber-glass particle composite. For both datasets, the AI-generated microstructures with transfer learning were utilized to detect key features of particles and fibers within the microstructure. Subsequently, those AI-generated microstructures were reintroduced into the FEA to obtain their stress-strain curves. The AI-generated stress-strain curves were then compared to the original stress-strain curves, which demonstrated a close correlation, particularly in the elastic regions, shown in Figure 5.6 (c) and Figure 5.6 (d). However, due to the uneven feature edges in some of the generated images, the filler features became elongated or shortened during the feature detection step. This might cause the overestimation in Figure 5.6 (c) and underestimation in Figure 5.6 (d) during the simulation of the AI-generated stress-strain curves like in Case-1 in the failure region. As shown in the figures, the model effectively forecasts tailored microstructures that align with the desired stress-strain curves, where the key features and orientations of the fillers closely resemble the original microstructures. Compared to re-training the DL model, the transfer learning process reduced the training time by around 52% and the required dataset size by around 78%.

5.3 Conclusions

In conclusion, we developed an AI-driven design framework for hybrid composites by integrating FEA with advanced ML approaches. Specifically, we employed a cGAN-LSTM-based model to directly generate tailored microstructures based on desired full-range stress-strain curves. This inverse S-P design process was demonstrated by elastomer-based and epoxy-based hybrid composites. The model demonstrated substantial feature similarity with a low FID score of 0.21 and 0.577 on the validation and testing datasets. We also compared the stress-strain curves of the AI-generated microstructures with the target stress-strain curves, resulting in 88% well-matched cases. We further employed transfer learning techniques to fine-tune the model to expand the design capability for other materials. The transfer learning models achieved FID scores of 0.281 and 0.182 on the test datasets for epoxy-carbon fiber-glass particle composites and epoxy-glass fiber-glass particle composites, respectively. This study established inverse S-P relationships featuring hybrid microstructures of matrix, fibers and particular fillers, as well as a fully trained baseline cGAN-LSTM model.

CHAPTER 6
FORMULATION OF INVERSE S-P RELATIONSHIPS

6.1 Introduction

With recent advancements in technology, the design of advanced hybrid composite materials with customized properties has significantly expanded for specific requirements. The concept of inverse S-P relationships involves understanding and developing methodologies for designing new materials with tailor-made functionalities for specific applications. A deeper understanding of inverse S-P relationships allows the design to be a more systematic, computational approach towards advanced modeling, simulation tools and AI driven approaches. However, to design these advanced materials to meet specific performance criteria requires a deep understanding of the intricate relationship between their structure and properties. Traditional approaches to material design often rely on time-consuming and costly direct experimentation and empirical models. To address these issues, formulating inverse S-P relationships is essential for accelerating the development of new materials with optimized performance for a wide range of applications. The integration of domain-specific knowledge or constraints into computational modelling and AI driven approaches can revolutionize the design of tailor-made materials by governing material behavior. This integration is known as a Domain-Specific Constraint Model which are computational model that explicitly incorporates domain-specific knowledge and empirical constraints into the model's architecture, loss functions, or training objectives. This approach improves the learning process and align the model's outputs with known theoretical or real-world behaviors. It also generalizes the model by incorporating meaningful fundamental information to enhance the accuracy of predictions in ML algorithms. By leveraging fundamental knowledge of material science and advanced computational techniques, obtaining the key relationship of inverse S-P will be more prominent. This inverse approach enables the custom design of hybrid composite materials with desired properties and reduces the need for trial-and-error experimentation. By combining empirical insights with computational modeling, it enhances efficiency and improves results in material design.

In this work, we applied a Domain-Specific Constraint Model using a fine-tuned CGAN-LSTM to tailor the microstructures of composite materials and achieve specific mechanical properties for automotive applications and experimental datasets. For automotive applications, we have designed a segmented front upper control arm where iterative adjustments across five generations achieved uniform stress distribution for each segment demonstrating the data-driven design efficacy. Using transfer learning on composite datasets, we refined the domain-specific constraint model's architecture and hyperparameters by improving the resemblance of generated microstructures to experimental data. With the incorporation of empirical domain constraints, the model demonstrated significant improvements in generating realistic microstructure to accurately capture filler morphology and mechanical properties. Furthermore, the model generated outputs mimic the real-world conditions enhancing both the efficiency and accuracy of material design.

6.2 Front Upper Control Arm Demonstration

To demonstrate real-world application and enhance the performance of automotive components, we applied targeted mechanical properties by generating tailored microstructures for a front upper control arm. For front upper control arm, we utilized a hybrid composite made from epoxy, carbon fiber, and glass particles. Although the strength of this composite may be lower than steel, the main goal is to showcase the capability of the customized CGAN model in tailoring the microstructure to achieve optimal mechanical properties such as tensile strength, stiffness, and impact resistance. By customizing the material's microstructure, we optimized different parts of the component for desired performance and demonstrated the model’s ability to design materials with the right balance of mechanical properties for real-world automotive applications.

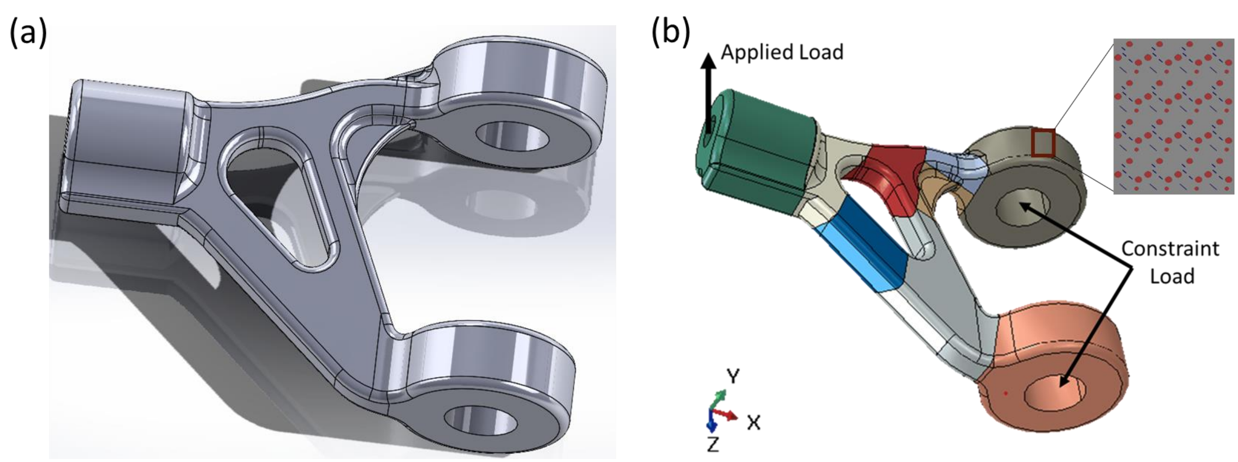

Figure 6.1: (a) 3D model and (b) applied load and boundary condition for demonstration of hybrid composite materials in the application of automotive front upper control/suspension arm.

Figure 6.1 illustrates the geometric structure of an automotive front upper control arm (suspension arm) and its division into 9 parts where each part has different microstructures and material properties using a hybrid composite. Figure 6.1(b) shows the different colored regions representation of various components made from hybrid composites and optimized for even stress distribution across all parts for automotive applications. This also represent the different microstructural composition of the composite materials, including the volume fraction of fillers, the combination of fillers, and fiber orientations within the matrix.

Figure 6.2 demonstrates the simulation results of the front upper control arm under cyclic loading conditions and the stress distribution across different stages of the load cycle. Each arm displayed with a color gradient representing stress levels, where red indicates areas of higher stress and blue represents lower stress. As the load was applied cyclically ranging from 7.5 psi to -7.5 psi, the stress patterns evolve with specific regions experiencing higher stress concentrations that require optimization for evenly distributed maximum stress. Optimization for evenly distributed maximum stress is needed to prevent localized stress concentrations to improve the component's durability from damage in specific areas of the component.

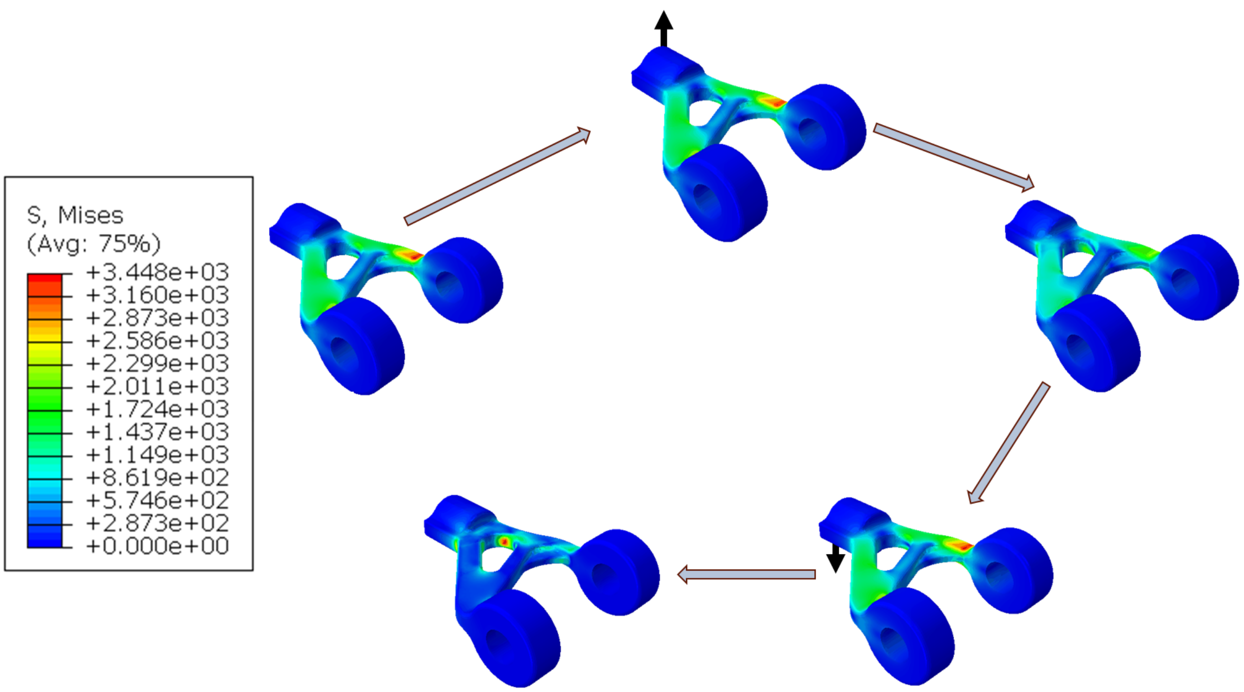

Figure 6.2: Demonstration of front upper control/suspension arm on cyclic loading condition highlighting stress distribution and mechanical performance of the hybrid composite material.

In this step, we have done the iterative optimization of mechanical properties across five generations to achieve even distribution of maximum 1st principal stress across all parts of the front upper control arm. Figure 6.3 shows the stress-strain curves for the front upper control arm components across five generations. In each generation, different mechanical properties (such as Young's modulus, yield stress, and plastic strain) were applied to each component during simulation. The goal was to iteratively update these properties to bring the maximum 1st principal stress of all components to similar levels for uniform stress distribution. Each generation represents a step toward optimizing these mechanical properties based on the analysis of the previous one. Figure 6.4 displays the bar charts showing the maximum 1st principal stress for each component of the control arm over five generations. Initially, the stress varied significantly between components, however, with each generation the mechanical properties were adjusted to reduce these discrepancies. By the final generation, all the parts of front upper control arm achieved even stress distribution, as the stress levels for each part became more similar.

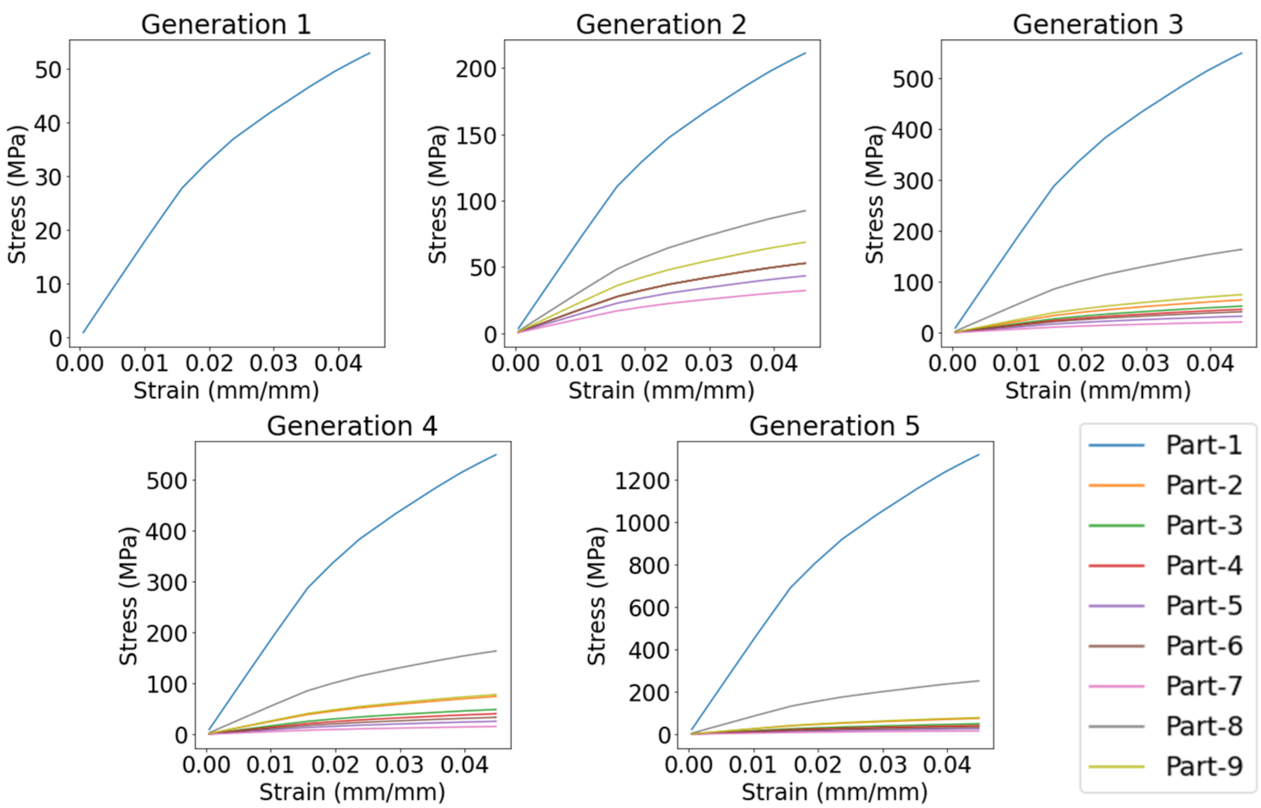

Figure 6.3: Stress-strain curves showing the evolution of mechanical properties across generations for targeted stress distribution.

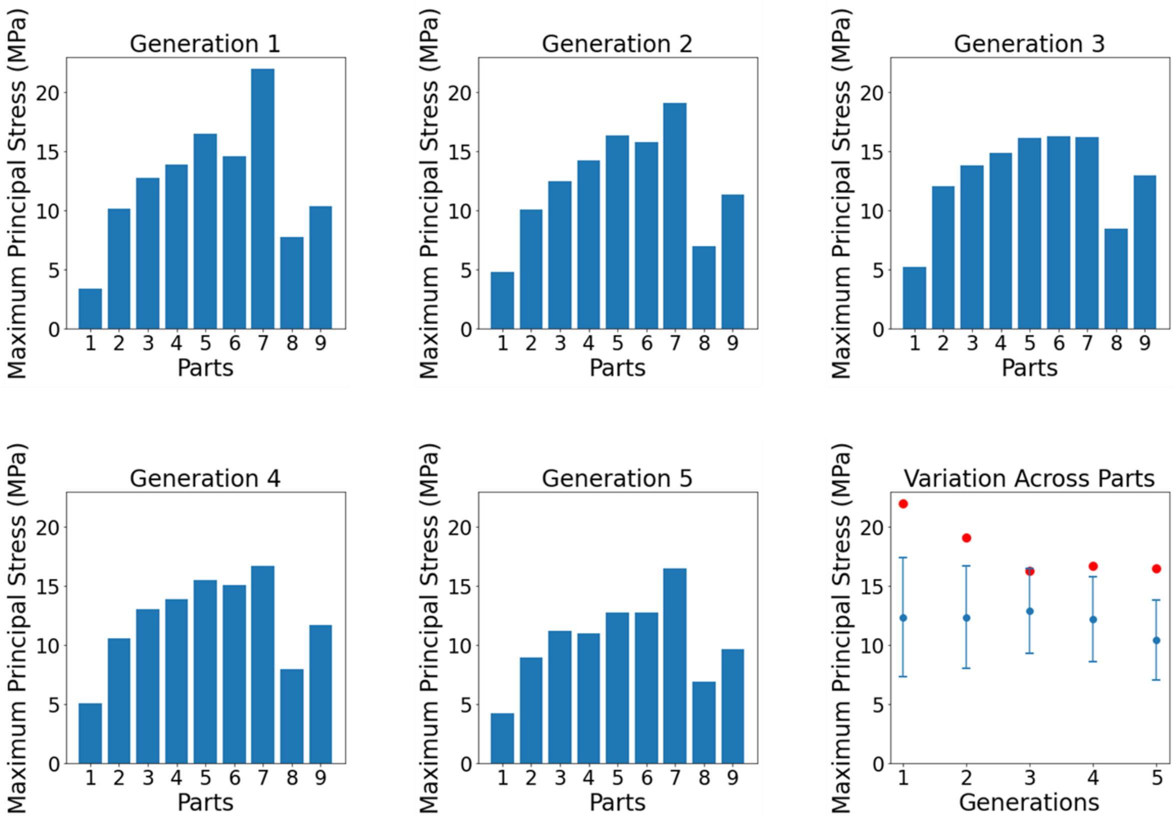

Figure 6.4: Maximum 1st principal stress utilized for evenly distributed stress concentrations on all the parts during different generation phase and variation across generation.

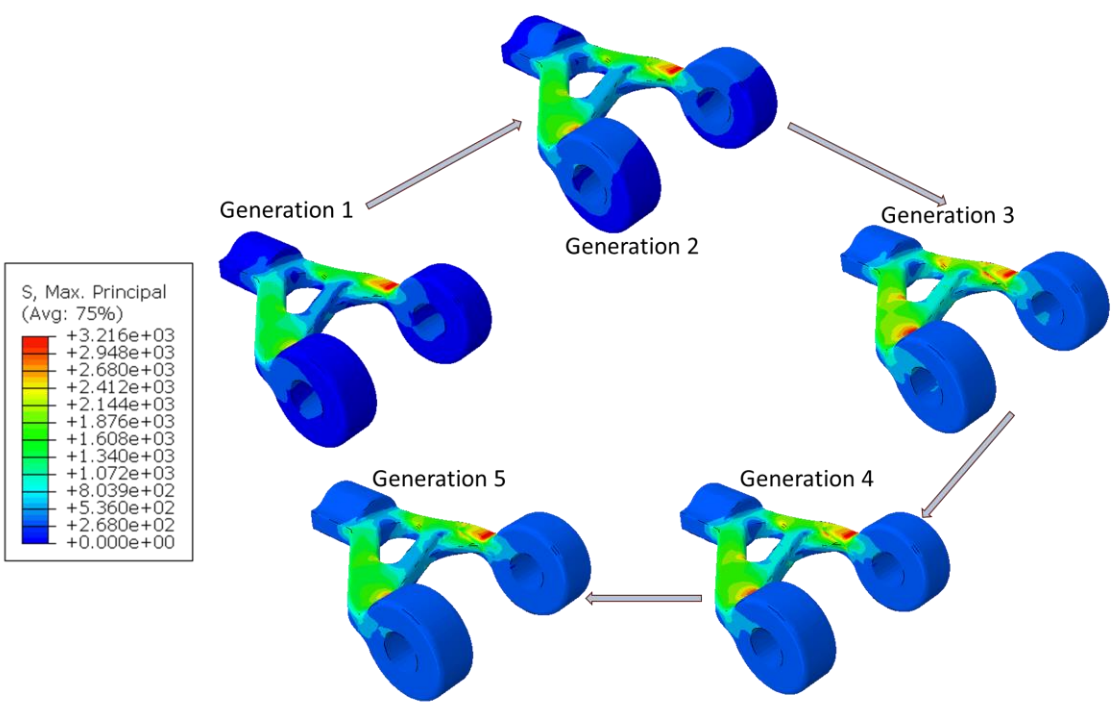

Figure 6.5: Different generational phase of front upper control/suspension arm highlighting maximum stresses.

Figure 6.5 provides visual representations of the stress distribution across the control arm in each generation using a color gradient to indicate stress levels. Early generations show uneven stress distributions with certain regions experiencing higher concentrations of stress. As mechanical properties were optimized over successive generations, the stress distribution becomes more even which indicates the iterative approach successfully optimized the material properties for uniform stress performance.

6.3 Transfer Learning on Experimental Dataset

To validate the current deep learning framework, we utilized an experimental dataset to further assess the model's efficacy. Specifically, we used both single and double filler composites, including PDMS-hollow spherical glass particle composites and PDMS-hollow spherical glass particle-glass fiber composites. We 3D-printed and casted a substantial dataset by varying filler volume fractions, orientations, and printing conditions, and collected diverse microstructure images of the composites using an optical microscope. Additionally, we performed tensile tests to evaluate the impact of these parameter variations on the mechanical stress-strain data.

Initially, we employed a transfer learning approach to refine the model based on previously trained models. For fine-tuning, we have used updated dataset and adjusted the learning rate to a lower value of 0.00001 to ensure that the pre-trained model's weights are not drastically altered. Additionally, we also incorporated a learning rate scheduler to dynamically reduce the learning rate if the validation loss stagnates. Furthermore, the model was fine-tuned over a total of 100 epochs on the new dataset and evaluated using the FID to measure the similarity between the generated and real images for checking models performance. Figure 6.6 shows the generated microstructure from transfer learning techniques and simulated/real microstructures for version 1.1 (V 1.1) and version 1.2 (V 1.2). The main difference between two version of the models is learning rate which is 0.0005 for V 1.1 and 0.00001 for V 1.2 which resulted in significant variations in the outcomes. The microstructure generated by V 1.1 exhibits poor structural quality due to the repetition of fiber positions. In contrast, V 1.2 has very high FID score of 1.6743 on the test dataset, also showed poor structural similarity with indication of challenges in generating realistic microstructures with these parameters.

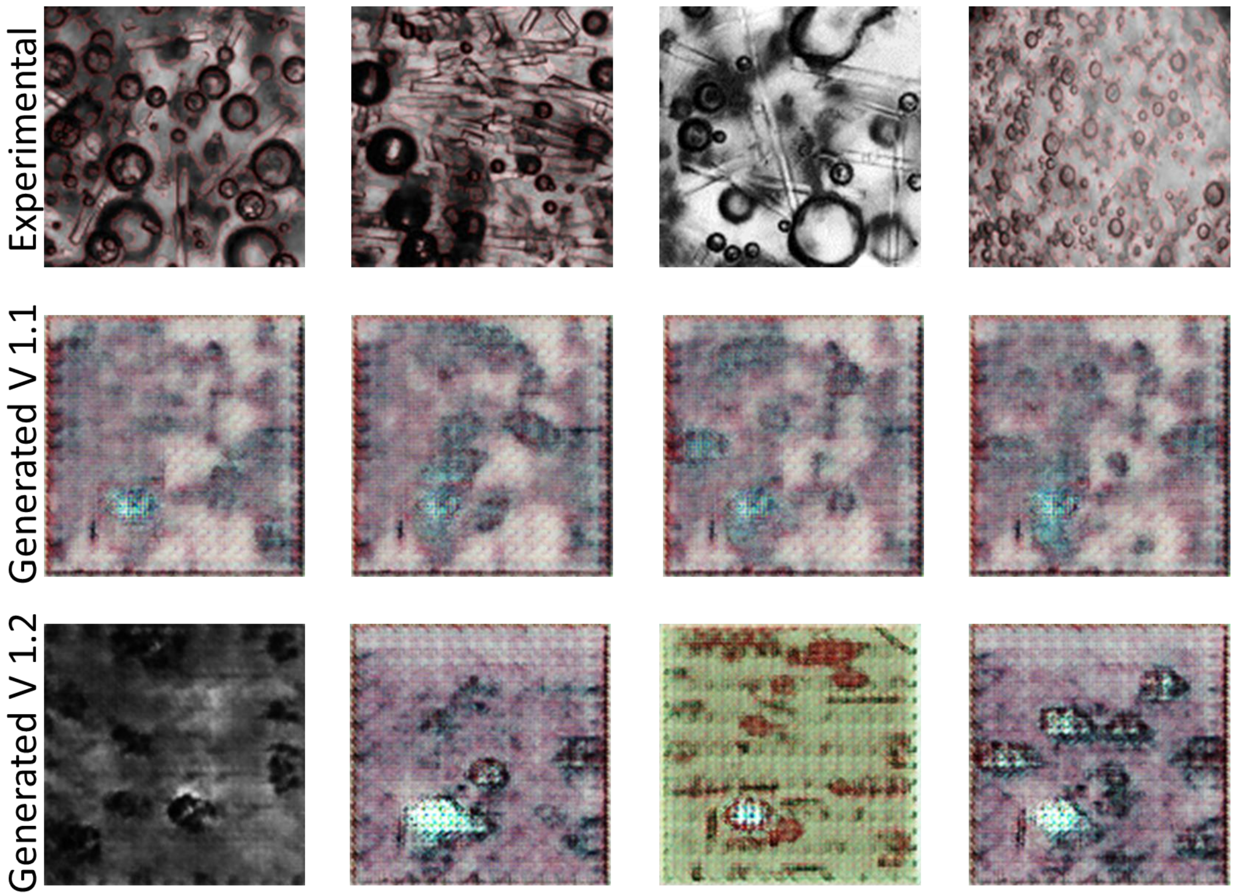

Figure 6.6: Transfer learning results using for version 1.1 and 1.2, similar architecture of pretrained model on experimental dataset containing PDMS-glass particle-glass fiber hybrid composite.

Later, we have updated the transfer learning approach by further adjusting the hyperparameters to better align the generated microstructures with the simulated/real microstructures, known as V2. For that, we have updated the model with a significantly reduced learning rate 0.000001 to ensure more subtle adjustments to the pre-trained weights, while increasing the number of training epochs to 300 to converge the model for new data. Additionally, we incorporated custom data augmentation techniques such as random flipping, rotation, brightness, and contrast adjustments to improve generalization. We also reshuffled and merged multiple datasets of 3d printed PDMS-glass particle composite and PDMS-glass particle-glass fiber hybrid composite to enhance the model's ability for generalization across different microstructure types. Lastly, we implemented layer freezing for certain layers of the model to remain fixed while fine-tuning others and monitor the performance of the model. Figure 6.7 represents the updated models generated microstructure and simulated/real microstructures. However, although the model performance has not significantly improved, the generated microstructures exhibited more distinctive features. As shown in the Figure 6.7, the texture and particle formations in the generated images have evolved to resemble the structures more closely. Few details showed improvements such as the distribution and shape of particles, however, the overall fidelity and alignment with the real microstructure still require further optimization.

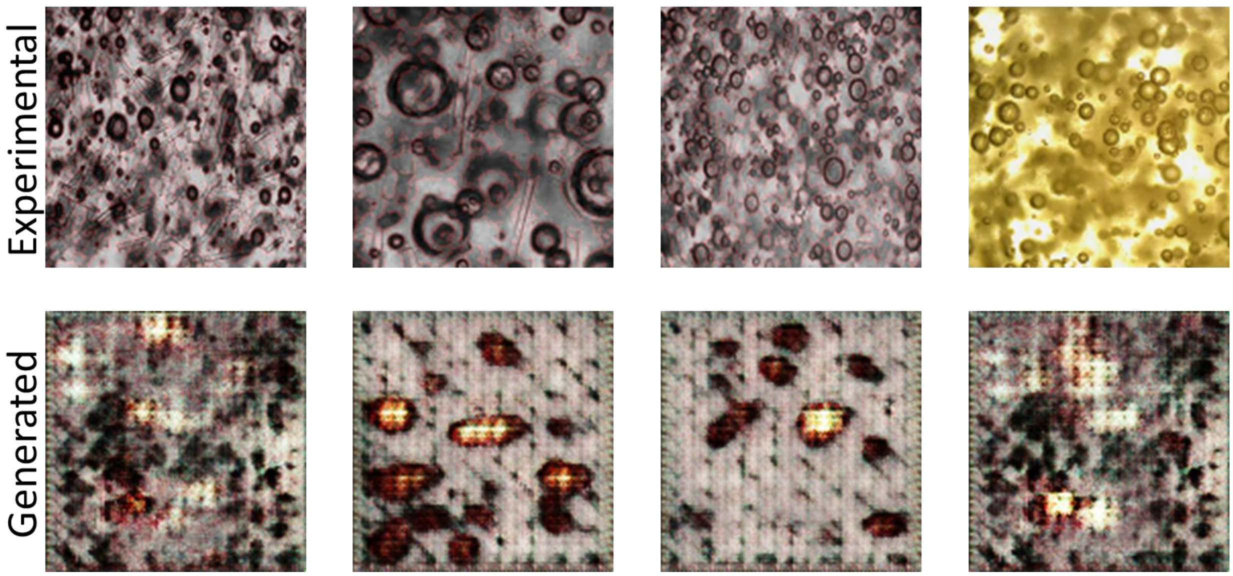

Figure 6.7: Transfer learning V2 with base model architecture with fine-tuned parameters results on experimental dataset containing PDMS-glass particle-glass fiber hybrid composite.

In the next phase, we enhanced the model to improve the resemblance of generated microstructures by incorporating additional datasets for combining multiple sources for more comprehensive training, labeled as V3. Additional datasets contain casted composites and hybrid composites. We also modified the training strategy by selectively freezing and unfreezing layers at different stages of training to better retain useful pre-trained features for adapting to new data. Key hyperparameters were further adjusted, including a reduction in the learning rate and updates to the number of critic steps, to stabilize the training process and enhance performance. However, the generated microstructure started to resemble more to the pretrained model generated microstructure. In the Figure 6.8, the microstructure generated began to exhibit more distinct features. However, the generated images continue to inherit dominant characteristics from the pre-trained model instead of showing significant adaptation to the new dataset. The generated microstructure displays similarities in pattern and texture to the pre-trained model, particularly in the arrangement of elongated shapes and clustered regions, lack the intended variability or refinement expected from training on the new data. From that we can say that the generated images fail to adequately capture the complexity or realism of the new training data.

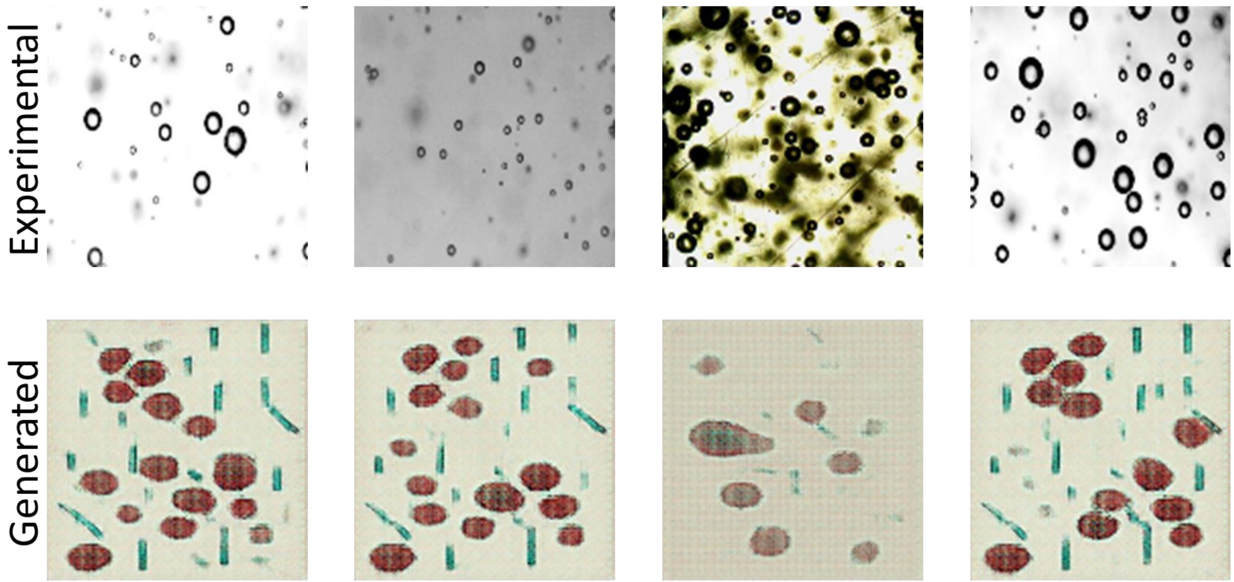

Figure 6.8: Transfer learning V3 with updated fine-tuned parameters results on experimental dataset containing PDMS-glass particle composite.

As further adjustments and refinements in the training process are required to push the model towards generating microstructures for reflecting the diversity of the new dataset, we introduced additional techniques to enhance model performance. We utilized transfer learning with architectural modifications to fine-tune our base CGAN-LSTM model updating its knowledge for experimental composite materials, described as V4. This process leverages the pretrained model's initial weights and modifies the architecture to accommodate the structural and conditional characteristics of the new datasets for better performance on the updated task. By gradually unfreezing layers and introducing new convolutional blocks, we allowed the model to learn both low-level and high-level features specific to the composite material domain. Additionally, we incorporated custom loss functions, such as microstructure loss and feature matching, which enabled the model to generate images that accurately capture the intricate particle distributions and stress-strain relationships found in the experimental data. The microstructure loss ensured that the generated images maintained realistic particle sizes, distributions, and intensities, while mimicking the physical characteristics of the materials. Feature matching further refined the generator for improving the overall visual quality as well as structural fidelity of the generated microstructures by comparing intermediate features between real and generated images.

In our work, the fine-tuning process involved several key architectural modifications that optimized the base CGAN-LSTM model for the composite material dataset. Firstly, we froze most of the pretrained layers in both the generator and discriminator to retain their prior knowledge and gradually unfreezing deeper layers during training for adaptation to the new data. Then, we updated both the generator and discriminator convolutional layers by progressively up sampling feature maps conditioned on strain-stress sequences at each stage of generation to accurately reflect the mechanical properties of the materials. During training, the Wasserstein loss with gradient penalty was used to stabilize the GAN's training and prevent mode collapse while the generator and discriminator learned. To ensure the physical accuracy of the generated microstructures, the microstructure loss specifically evaluated the generated images against the real ones by comparing statistical properties like particle size, distribution, and intensity. Additionally, the feature matching loss supported the generator to produce images of realistic looking at the pixel level and similar internal feature activations like real images as assessed by the discriminator. These combined mechanisms allowed the model to refine its outputs for progressively producing images that closely matched the intricate structures and properties of the real microstructure data. The accuracy and quality of the generated images were quantitatively measured as reflected in the significantly lower Fréchet Inception Distance (FID) scores and improved SSIM values during validation.

Figure 6.9 shows the results from the fine-tuned CGAN-LSTM model where model has a clear improvement in generating microstructure images to accurately reflect the experimental composite material data. Comparing with the real images, the generated images demonstrated highly consistent particle sizes and accurate spatial arrangement along with the significant reduction in discrepancies between the mean and standard deviation of particle sizes. Additionally, the generated images have smoother internal structures transitions and more natural particle formations for feature matching loss contribution. Quantitatively, the model achieved a notable improvement in FID score which dropped from 1.6743 to 0.7779, indicating that the generated image distribution converged much closer to that of the real data. Furthermore, the customized loss values decreased from 12.8179 to -0.0017 and showed similarity in overall appearance as well as retained critical structural features, particularly in terms of texture and material contrast. The visual comparison between the real and generated images showed that the fine-tuning successfully preserved the particle morphology and strain-stress relationships for a reliable representation of the material microstructures observed in the experimental data. These results confirm that the architectural modifications and custom loss functions directly contributed to produce high-quality microstructures closely aligned with real-world material properties. The domain-specific constraint models were capable of generating microstructures for both individual particle-based and hybrid composites.

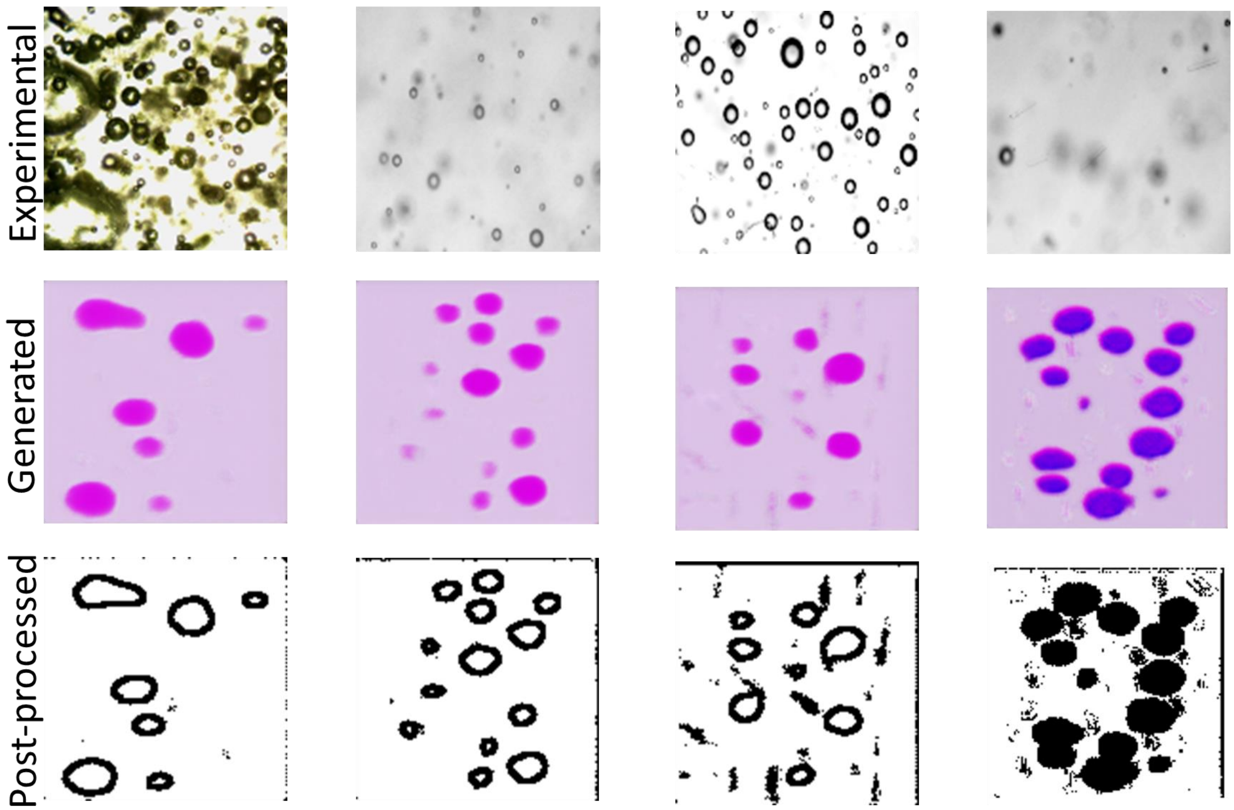

Figure 6.9: Transfer learning V4 with upgraded architecture results on experimental dataset containing PDMS-glass particle composite and PDMS-glass particle-glass fiber hybrid composite.

6.4 Conclusions

In conclusion, we demonstrated the real-life application of a CGAN model for tailoring the microstructures of composite materials to achieve specific mechanical properties in both automotive applications and experimental datasets. For the automotive front upper control arm, we iteratively adjusted the mechanical properties of each part over five generations to achieve uniform maximum 1st principal stress across all components. Cyclic loading simulations and stress distribution analysis emphasized the importance of preventing localized stress concentrations to enhance durability which showcases the effectiveness of data-driven material design for manufacturing high-performance automotive components. Additionally, we validated the deep learning framework by applying a transfer learning approach on experimental composite datasets including single and double filler composites. Across multiple versions (V1.1 to V4), we iteratively refined the model's architecture and hyperparameters to improve the resemblance of the generated microstructures to real experimental data. Key strategies included adjusting learning rates, incorporating data augmentation, freezing/unfreezing layers, and implementing custom loss functions like microstructure loss and feature matching. The model's performance evaluated by using FID and validation loss values which showed progressive improvement particularly in version V4. Version V4 achieved a significant reduction in the FID score reflecting better alignment between generated and real microstructure images. Despite some challenges in capturing the full complexity of the dataset, the fine-tuned domain specific constraint CGAN-LSTM model demonstrated clear advancements in generating high-fidelity images that accurately represent the particle shape, distributions, and mechanical properties of the composite materials.

CHAPTER 7
CONCLUSIONS AND FUTURE WORK

7.1 Conclusions

In conclusion, we have demonstrated a comprehensive framework for designing and characterizing the S-P relationships of lightweight hybrid composites. This study leveraged a multifaceted approach that includes conventional DOE, a theoretical hybrid model, and advanced, image-driven ML methods to elucidate the intricate mechanical behaviors of these advanced materials. Conventional DOE approaches were utilized, highlighting the significant impact of printing direction and fiber volume fraction on material properties. While a hybrid mechanics model was proposed, it tended to overestimate the mechanical properties; conversely, an image-driven ML model provided more accurate predictions with significantly lower error rates.

Furthermore, we developed a microstructural design approach by integrating FEA and advanced ML aiming for customized solutions across various material prospects. Our cGAN-LSTM framework demonstrated the capability to generate tailored microstructures which are closely align with specific stress-strain sequences and exhibit strong feature similarity as well as low FID scores. The model’s predictive accuracy was validated through the re-simulation of composite microstructures along with the majority of cases showing minimal error. The integration of transfer learning further enhanced the model's performance across different material scales, such as stronger and stiffer materials by achieving even lower FID scores for epoxy-based composites. The transfer learning model effectively generated customized microstructures aligned with the desired mechanical properties by mapping filler features and spatial orientations to mimic real microstructures. Also, the implementation of transfer learning approach reduced the training time and required data size significantly.

Additionally, we explored the formulation of inverse S-P relationships through the incorporation of domain specific constraint models by enhancing our understanding of how individual constraints, such as microstructure features influence on these tailor-made materials. To validate the approach, we applied a domain specific constraint transfer learning method on an experimental dataset of composite materials with single and double fillers. Through iterative refinements across multiple versions, key strategies such as data augmentation, learning rate adjustments, and custom domain-specific loss functions improved the model's performance. Version V4 significantly reduced FID scores and better aligning the generated microstructures with real experimental data as well as accurately representing the filler shapes and distributions. Moreover, we demonstrated the real-life application of a CGAN model in automotive parts by tailoring composite material microstructures to achieve specific mechanical properties. For these automotive parts, we used the front upper control arm where iterative adjustments over five generations resulted in uniform stress distribution across all sections. The integration of conventional experimental designs with advanced theoretical and ML approaches presents a promising methodology for investigating the mechanical behaviors of lightweight hybrid composites.

7.2 Limitations and Future works

The limitation of this study is that we have only considered out-of-plane fillers. In-plane fillers can be difficult for the model to recognize due to the different alignment of the filler. In cGAN-LSTM model training, only cylindrical and circular fillers with lengths of 0.031-0.215 mm and radii of 0.02-0.049 mm were considered. Additionally, the model struggles to differentiate voids from particle fillers and sometimes falsely identifies voids as fillers due to imperfections in experiments.

In future work, we will focus on extending our existing FEA and deep learning framework to explore and customizing hybrid composite materials for utilizing alternative fiber and particle reinforcements. Building upon our current model, we will integrate new material options such as natural fiber (hemp, flax, etc.), multi-walled carbon nanotube, corn starch, cellulose microbeads, silica-based particles. These materials offer promising mechanical properties, including high tensile strength, improved toughness, and enhanced wear resistance, making them suitable for automotive applications. To refine our approach, we will focus on optimizing the composite microstructure by varying especially, filler geometry including circular, cylindrical, ellipse and other-shaped reinforcements. We will also incorporate multi-scale modeling techniques to analyze the effect of microstructure on macro-level performance, particularly under complex loading scenarios like combined bending, torsion, and impact loads. To further improve prediction accuracy, we will enhance the current deep learning model by incorporating additional physics-informed constraints to incorporate real-world operational conditions. Further improvement in the design will be able to deliver a next-generation composite material solution for realistic application with superior mechanical performance and weight efficiency.

REFERENCES

1. Grand View Research. *Composites market size and share analysis report, 2030*. https://www.grandviewresearch.com/industry-analysis/composites-market (2023).

2. SkyQuest Technology. *Composites market size, share, and growth analysis 2022-2030*. https://www.skyquestt.com/report/composites-market (2023).

3. Claunch, E. C. Forecasting on Composites – Markets, Products, and Demands. *J. Text. Appar. Technol. Manag.* **9**, (2015).

4. Nester, R. *Hybrid Composites Market revenue to exceed USD 21 Billion by 2035, says Research Nester*. https://www.globenewswire.com/en/news-release/2023/10/05/2755203/0/en/Hybrid-Composites-Market-revenue-to-exceed-USD-21-Billion-by-2035-says-Research-Nester.html (2023).

5. Krauklis, A. E., Karl, C. W., Gagani, A. I. & Jørgensen, J. K. Composite Material Recycling Technology—State-of-the-Art and Sustainable Development for the 2020s. *J. Compos. Sci.* **5**, (2021).

6. Ravishankar, B., Nayak, S. K. & Kader, M. A. Hybrid composites for automotive applications – A review. *J. Reinf. Plast. Compos.* **38**, 835–845 (2019).

7. Sauer, Michael and Kuhnel, M. Composites market report 2019. *Carbon Compos.* **2**, 1–11 (2019).

8. Chavhan, G. R. & Wankhade, L. N. Improvement of the mechanical properties of hybrid composites prepared by fibers, fiber-metals, and nano-filler particles – A review. *Mater. Today Proc.* **27**, 72–82 (2020).

9. Jamir, M. R. M., Majid, M. S. A. & Khasri, A. Natural lightweight hybrid composites for aircraft structural applications. in *Sustainable composites for aerospace applications* 155–170 (Elsevier, 2018).

10. Gu, H. *et al.* Introducing advanced composites and hybrid materials. *Adv. Compos. Hybrid Mater.* **1**, 1–5 (2018).

11. Xie, C., Cao, M., Guan, J., Liu, Z. & Khan, M. Improvement of boundary effect model in multi-scale hybrid fibers reinforced cementitious composite and prediction of its structural failure behavior. *Compos. Part B Eng.* **224**, 109219 (2021).

12. Zhang, J., Chaisombat, K., He, S. & Wang, C. H. Hybrid composite laminates reinforced with glass/carbon woven fabrics for lightweight load bearing structures. *Mater. Des.* **36**, 75–80 (2012).

13. Bazan, P., Nosal, P., Wierzbicka-Miernik, A. & Kuciel, S. A novel hybrid composites based on biopolyamide 10.10 with basalt/aramid fibers: Mechanical and thermal investigation. *Compos. Part B Eng.* **223**, 109125 (2021).

14. Banerjee, S. & Sankar, B. V. Mechanical properties of hybrid composites using finite element method based micromechanics. *Compos. Part B Eng.* **58**, 318–327 (2014).

15. Cheng, P. *et al.* 3D printed continuous fiber reinforced composite lightweight structures: A review and outlook. *Compos. Part B Eng.* **250**, 110450 (2023).

16. Bouhfid, N. *et al.* 5 - Numerical modeling of hybrid composite materials. in *Modelling of Damage Processes in Biocomposites, Fibre-Reinforced Composites and Hybrid Composites* (eds. Jawaid, M., Thariq, M. & Saba, N.) 57–101 (Woodhead Publishing, 2019). doi:https://doi.org/10.1016/B978-0-08-102289-4.00005-9.

17. Mustapha, A. N. *et al.* Taguchi and ANOVA analysis for the optimization of the microencapsulation of a volatile phase change material. *J. Mater. Res. Technol.* **11**, 667–680 (2021).

18. Kowalczyk, M. Application of Taguchi and Anova Methods in Selection of Process Parameters for Surface Roughness in Precision Turning of Titanium. *Adv. Manuf. Sci. Technol.* **38**, 21–35 (2014).

19. Auffray, L., Gouge, P. A. & Hattali, L. Design of experiment analysis on tensile properties of PLA samples produced by fused filament fabrication. *Int. J. Adv. Manuf. Technol.* **118**, 4123–4137 (2022).

20. Yang, W. qiang *et al.* Designable Mechanical Properties of 3D Printing Composites with

Multiple Filaments by Different Infill Percentages and Structures. *Adv. Eng. Mater.* **21**, 1900508 (2019).

21. Das, A. *et al.* Rheological investigation of nylon-carbon fiber composites fabricated using material extrusion-based additive manufacturing. *Polym. Compos.* **42**, 6010–6024 (2021).

22. El Magri, A., El Mabrouk, K., Vaudreuil, S. & Ebn Touhami, M. Experimental investigation and optimization of printing parameters of 3D printed polyphenylene sulfide through response surface methodology. *J. Appl. Polym. Sci.* **138**, 49625 (2020).

23. Xu, H., Liu, R., Choudhary, A. & Chen, W. A Machine Learning-Based Design Representation Method for Designing Heterogeneous Microstructures. *J. Mech. Des. Trans. ASME* **137**, 1–10 (2015).

24. Mo, C., Jiang, Y. & Raney, J. R. Microstructural evolution and failure in short fiber soft composites: Experiments and modeling. *J. Mech. Phys. Solids* **141**, 103973 (2020).

25. Ferdousi, S., Advincula, R., Sokolov, A. P., Choi, W. & Jiang, Y. Investigation of 3D printed lightweight hybrid composites via theoretical modeling and machine learning. *Compos. Part B Eng.* **265**, 110958 (2023).

26. Shashank Sharma Sameehan S. Joshi, M. V. P. M. R. S. M. & Dahotre, N. B. Multiphysics multi-scale computational framework for linking process–structure–property relationships in metal additive manufacturing: a critical review. *Int. Mater. Rev.* **68**, 943–1009 (2023).

27. Kouraytem, N., Li, X., Tan, W., Kappes, B. & Spear, A. D. Modeling process-structure-property relationships in metal additive manufacturing: A review on physics-driven versus data-driven approaches. *JPhys Mater.* **4**, 032002 (2021).

28. Li, G., Ferdousi, S., Tejeda-Godinez, G. & Jiang, Y. 3D-printed self-cleaning structured surfaces through capillary force. *MRS Commun.* **12**, 982–987 (2022).

29. Ravoori, D., Alba, L., Prajapati, H. & Jain, A. Investigation of process-structure-property relationships in polymer extrusion based additive manufacturing through in situ high speed imaging and thermal conductivity measurements. *Addit. Manuf.* **23**, 132–139

(2018).

30. Gu, G. X., Takaffoli, M. & Buehler, M. J. Hierarchically Enhanced Impact Resistance of Bioinspired Composites. *Adv. Mater.* **29**, 1700060 (2017).

31. Khatri, N. R. *et al.* Integrating helicoid channels for passive control of fiber alignment in direct-write 3D printing. *Addit. Manuf.* **48**, 102419 (2021).

32. Muth, J. T., Dixon, P. G., Woish, L., Gibson, L. J. & Lewis, J. A. Architected cellular ceramics with tailored stiffness via direct foam writing. *Proc. Natl. Acad. Sci.* **114**, 1832–1837 (2017).

33. Mo, C., Long, H. & Raney, J. R. Tough, aorta-inspired soft composites. *Proc. Natl. Acad. Sci.* **119**, e2123497119 (2022).

34. Woo, R., Chen, G., Zhao, J. & Bae, J. Structure–Mechanical Property Relationships of 3D-Printed Porous Polydimethylsiloxane. *ACS Appl. Polym. Mater.* **3**, 3496–3503 (2021).

35. Wang, Y. *et al.* Mining structure–property relationships in polymer nanocomposites using data driven finite element analysis and multi-task convolutional neural networks. *Mol. Syst. Des. Eng.* **5**, 962–975 (2020).

36. Cipriani, C. E. *et al.* Structure-Processing-Property Relationships of 3D Printed Porous Polymeric Materials. *ACS Mater. Au* **1**, 69–80 (2021).

37. Pena, E. Prediction of the softening and damage effects with permanent set in fibrous biological materials. *J. Mech. Phys. Solids* **59**, 1808–1822 (2011).

38. Marini, G. *et al.* A continuum description of the damage process in the arterial wall of abdominal aortic aneurysms. *Int. J. Numer. Method. Biomed. Eng.* **28**, 87–99 (2012).

39. Fu, S. Y., Feng, X. Q., Lauke, B. & Mai, Y. W. Effects of particle size, particle/matrix interface adhesion and particle loading on mechanical properties of particulate-polymer composites. *Compos. Part B Eng.* **39**, 933–961 (2008).

40. Martinez-Garcia, J. C. *et al.* A generalized approach for evaluating the mechanical properties of polymer nanocomposites reinforced with spherical fillers. *Nanomaterials* **11**,

830 (2021).

41. Liang, J. Z., Li, R. K. Y. & Tjong, S. C. Morphology and tensile properties of glass bead filled low density polyethylene composites: MATERIAL PROPERTIES. *Polym. Test.* **16**, 529–548 (1998).

42. Qi, H. J. & Boyce, M. C. Constitutive model for stretch-induced softening of the stress-stretch behavior of elastomeric materials. *J. Mech. Phys. Solids* **52**, 2187–2205 (2004).

43. Li, W. Damage Models for Soft Tissues: A Survey. *J. Med. Biol. Eng.* **36**, 285–307 (2016).

44. Ochiai, S., Hojo, M. & Inoue, T. Shear-lag simulation of the progress of interfacial debonding in unidirectional composites. *Compos. Sci. Technol.* **59**, 77–88 (1999).

45. López Jiménez, F. & Pellegrino, S. Constitutive modeling of fiber composites with a soft hyperelastic matrix. *Int. J. Solids Struct.* **49**, 635–647 (2012).

46. Yang, Z., Niksiar, P. & Meng, Z. Identifying structure-property relationships of micro-architectured porous scaffolds through 3D printing and finite element analysis. *Comput. Mater. Sci.* **202**, 110987 (2022).

47. Zhao, Y., Chen, Y. & Zhou, Y. Novel mechanical models of tensile strength and elastic property of FDM AM PLA materials: Experimental and theoretical analyses. *Mater. Des.* **181**, 108089 (2019).

48. Tang, H., Chen, H., Sun, Q., Chen, Z. & Yan, W. Experimental and computational analysis of structure-property relationship in carbon fiber reinforced polymer composites fabricated by selective laser sintering. *Compos. Part B Eng.* **204**, 108499 (2021).

49. Papon, E. A. & Haque, A. Review on process model, structure-property relationship of composites and future needs in fused filament fabrication. *J. Reinf. Plast. Compos.* **39**, 758–789 (2020).

50. Abbott, A. C., Tandon, G. P., Bradford, R. L., Koerner, H. & Baur, J. W. Process-structure-property effects on ABS bond strength in fused filament fabrication. *Addit.*

Manuf. **19**, 29–38 (2018).

51. Zhu, C., Zhu, P. & Liu, Z. Uncertainty analysis of mechanical properties of plain woven carbon fiber reinforced composite via stochastic constitutive modeling. *Compos. Struct.* **207**, 684–700 (2019).

52. Prusty, B. G. & Banerjee, A. Structure–Property Correlation and Constitutive Description of Structural Steels during Hot Working and Strain Rate Deformation. *Materials (Basel).* **13**, (2020).

53. Wernik, J. M. & Meguid, S. A. Multiscale micromechanical modeling of the constitutive response of carbon nanotube-reinforced structural adhesives. *Int. J. Solids Struct.* **51**, 2575–2589 (2014).

54. Yu, Z., Liu, J. & Wei, X. A general property-structure relationship from crack stability analysis on hybrid staggered composites with elasto-plastic matrices. *Compos. Struct.* **240**, 112071 (2020).

55. Xu, R. *et al.* Microstructure-based modeling on structure-mechanical property relationships in carbon nanotube/aluminum composites. *Int. J. Plast.* **120**, 278–295 (2019).

56. Guo, F. *et al.* Dynamic shear fracture behaviors and "pseudo-plastic" constitutive model of carbon/carbon composite pins. *Int. J. Mech. Sci.* **187**, 105903 (2020).

57. Xu, X., Wang, G., Yan, H. & Yao, X. Constitutive relationship of fabric rubber composites and its application. *Compos. Struct.* **304**, 116302 (2023).

58. Kamiński, M. & Sokołowski, D. Probabilistic Analysis of Composite Materials with Hyper-Elastic Components. *Materials (Basel).* **15**, (2022).

59. Amamoto, Y. Data-driven approaches for structure-property relationships in polymer science for prediction and understanding. *Polym. J.* **54**, 957–967 (2022).

60. de Menezes, E. A. W., Eggers, F., Marczak, R. J., Iturrioz, I. & Amico, S. C. Hybrid composites: Experimental, numerical and analytical assessment aided by online software.

Mech. Mater. **148**, 103533 (2020).

61. Alkemper, J. & Voorhees, P. W. Quantitative serial sectioning analysis. *J. Microsc.* **201**, 388–394 (2001).

62. Devaraj, A. *et al.* Three-dimensional nanoscale characterisation of materials by atom probe tomography. *Int. Mater. Rev.* **63**, 68–101 (2018).

63. Le, L. M. *et al.* Hybrid Artificial Intelligence Approaches for Predicting Buckling Damage of Steel Columns Under Axial Compression. *Materials (Basel).* **12**, (2019).

64. Ly, H.-B. *et al.* Hybrid Artificial Intelligence Approaches for Predicting Critical Buckling Load of Structural Members under Compression Considering the Influence of Initial Geometric Imperfections. *Appl. Sci.* **9**, (2019).

65. Liu, X., Tian, S., Tao, F. & Yu, W. A review of artificial neural networks in the constitutive modeling of composite materials. *Compos. Part B Eng.* **224**, 109152 (2021).

66. Yang, L., Qi, C., Lin, X., Li, J. & Dong, X. Prediction of dynamic increase factor for steel fibre reinforced concrete using a hybrid artificial intelligence model. *Eng. Struct.* **189**, 309–318 (2019).

67. Soltani, M., Ferdousi, S., Haridas, R. S., Mishra, R. S. & Jiang, Y. A Crystal Plasticity Finite Element—Machine Learning Combined Approach for Phase Transformation Prediction in High Entropy Alloy. *Int. J. Appl. Mech.* **16**, 2450024 (2024).

68. Okafor, C. E. *et al.* Advances in machine learning-aided design of reinforced polymer composite and hybrid material systems. *Hybrid Adv.* **2**, 100026 (2023).

69. Sharma, A., Mukhopadhyay, T., Rangappa, S. M., Siengchin, S. & Kushvaha, V. Advances in Computational Intelligence of Polymer Composite Materials: Machine Learning Assisted Modeling, Analysis and Design. *Arch. Comput. Methods Eng.* **29**, 3341–3385 (2022).

70. Yang, H. *et al.* Energy absorption and failure pattern of hybrid composite tubes under quasi-static axial compression. *Compos. Part B Eng.* **198**, 108217 (2020).

71. Sun, G., Chen, D., Zhu, G. & Li, Q. Lightweight hybrid materials and structures for energy absorption: A state-of-the-art review and outlook. *Thin-Walled Struct.* **172**, 108760 (2022).

72. Di Benedetto, R. M., Botelho, E. C., Janotti, A., Ancelotti Junior, A. C. & Gomes, G. F. Development of an artificial neural network for predicting energy absorption capability of thermoplastic commingled composites. *Compos. Struct.* **257**, 113131 (2021).

73. Shirmohammadi, M., Goushchi, S. J. & Keshtiban, P. M. Optimization of 3D printing process parameters to minimize surface roughness with hybrid artificial neural network model and particle swarm algorithm. *Prog. Addit. Manuf.* **6**, 199–215 (2021).

74. Tran-Ngoc, H. *et al.* Efficient Artificial neural networks based on a hybrid metaheuristic optimization algorithm for damage detection in laminated composite structures. *Compos. Struct.* **262**, 113339 (2021).

75. Ramesh, M., Rajeshkumar, L. & Balaji, D. Influence of Process Parameters on the Properties of Additively Manufactured Fiber-Reinforced Polymer Composite Materials: A Review. *J. Mater. Eng. Perform.* **30**, 4792–4807 (2021).

76. Pattnaik, P. *et al.* Role of machine learning in the field of Fiber reinforced polymer composites: A preliminary discussion. *Mater. Today Proc.* **44**, 4703–4708 (2021).

77. Zhai, C., Li, T., Shi, H. & Yeo, J. Discovery and design of soft polymeric bio-inspired materials with multiscale simulations and artificial intelligence. *J. Mater. Chem. B* **8**, 6562–6587 (2020).

78. Xian, G., Guo, R. & Li, C. Combined effects of sustained bending loading, water immersion and fiber hybrid mode on the mechanical properties of carbon/glass fiber reinforced polymer composite. *Compos. Struct.* **281**, 115060 (2022).

79. Yuan, S., Li, S., Zhu, J. & Tang, Y. Additive manufacturing of polymeric composites from material processing to structural design. *Compos. Part B Eng.* **219**, 108903 (2021).

80. Yang, B., Fu, K., Lee, J. & Li, Y. Artificial Neural Network (ANN)-Based Residual Strength Prediction of Carbon Fibre Reinforced Composites (CFRCs) After Impact. *Appl.*

Compos. Mater. **28**, 809–833 (2021).

81. Chen, C.-T. & Gu, G. X. Generative Deep Neural Networks for Inverse Materials Design Using Backpropagation and Active Learning. *Adv. Sci.* **7**, 1902607 (2020).

82. Wu, J., Sigmund, O. & Groen, J. P. Topology optimization of multi-scale structures: a review. *Struct. Multidiscip. Optim.* **63**, 1455–1480 (2021).

83. Cappelli, L., Montemurro, M., Dau, F. & Guillaumat, L. Characterisation of composite elastic properties by means of a multi-scale two-level inverse approach. *Compos. Struct.* **204**, 767–777 (2018).

84. Wu, L., Zulueta, K., Major, Z., Arriaga, A. & Noels, L. Bayesian inference of non-linear multiscale model parameters accelerated by a Deep Neural Network. *Comput. Methods Appl. Mech. Eng.* **360**, 112693 (2020).

85. Wang, J., Wang, Y. & Chen, Y. Inverse Design of Materials by Machine Learning. *Materials (Basel).* **15**, (2022).

86. Conde, F. M. *et al.* Optimization of the microstructure of unidirectional hybrid composites under uniaxial tensile loads. *Compos. Struct.* **235**, 111795 (2020).

87. Mehl, K. *et al.* Structural Optimization of Locally Continuous Fiber-Reinforcements for Short Fiber-Reinforced Plastics. *J. Compos. Sci.* **5**, (2021).

88. Roy, A. *et al.* Machine-learning-guided descriptor selection for predicting corrosion resistance in multi-principal element alloys. *npj Mater. Degrad.* **6**, 9 (2022).

89. Elvas, A., Sohouli, A. & Suleman, A. Simultaneous topology and fiber path optimization of composite structures with MAC constraints. *Compos. Struct.* **294**, 115645 (2022).

90. He, Z. C., Shi, X., Li, E. & Li, X. K. Elastic properties and multi-scale design of long carbon fiber nonwoven reinforced plane-based isotropic composite. *Compos. Struct.* **251**, 112657 (2020).

91. Gupta, A., Cecen, A., Goyal, S., Singh, A. K. & Kalidindi, S. R. Structure-property linkages using a data science approach: Application to a non-metallic inclusion/steel

composite system. *Acta Mater.* **91**, 239–254 (2015).

92. Zhang, Z. *et al.* Predicting Flexural Strength of Additively Manufactured Continuous Carbon Fiber-Reinforced Polymer Composites Using Machine Learning. *J. Comput. Inf. Sci. Eng.* **20**, 061015 (2020).

93. Jiang, J., Xiong, Y., Zhang, Z. & Rosen, D. W. Machine learning integrated design for additive manufacturing. *J. Intell. Manuf.* **33**, 1073–1086 (2022).

94. Shah, V., Zadourian, S., Yang, C., Zhang, Z. & Gu, G. X. Data-driven approach for the prediction of mechanical properties of carbon fiber reinforced composites. *Mater. Adv.* **3**, 7319–7327 (2022).

95. Ferdousi, S. *et al.* Characterize traction–separation relation and interfacial imperfections by data-driven machine learning models. *Sci. Rep.* **11**, 14330 (2021).

96. Chowdhury, A., Kautz, E., Yener, B. & Lewis, D. Image driven machine learning methods for microstructure recognition. *Comput. Mater. Sci.* **123**, 176–187 (2016).

97. Yang, C., Kim, Y., Ryu, S. & Gu, G. X. Prediction of composite microstructure stress-strain curves using convolutional neural networks. *Mater. Des.* **189**, 108509 (2020).

98. Herriott, C. & Spear, A. D. Predicting microstructure-dependent mechanical properties in additively manufactured metals with machine- and deep-learning methods. *Comput. Mater. Sci.* **175**, 109599 (2020).

99. Kim, D.-W., Lim, J. H. & Lee, S. Prediction and validation of the transverse mechanical behavior of unidirectional composites considering interfacial debonding through convolutional neural networks. *Compos. Part B Eng.* **225**, 109314 (2021).

100. Tan, R. K., Zhang, N. L. & Ye, W. A deep learning–based method for the design of microstructural materials. *Struct. Multidiscip. Optim.* **61**, 1417–1438 (2020).

101. Wang, Z.-L. & Adachi, Y. Property prediction and properties-to-microstructure inverse analysis of steels by a machine-learning approach. *Mater. Sci. Eng. A* **744**, 661–670 (2019).

102. Link, N., Iraki, T. & Dornheim, J. Inverse Process-Structure-Property Mapping. *Res. Impact Key Ind.* 85.

103. Jiang, W. *et al.* Dispersion relation prediction and structure inverse design of elastic metamaterials via deep learning. *Mater. Today Phys.* **22**, 100616 (2022).

104. Urs, T. G., Gowtham, G. K., Somashekar, R. & Somashekarappa, H. M. Structure-property relation in HPMC:CoCl¬2 polymer composites using functional data analysis. *Acta Crystallogr. Sect. A* **73**, (2017).

105. Li, Y. Predicting materials properties and behavior using classification and regression trees. *Mater. Sci. Eng. A* **433**, 261–268 (2006).

106. Madhukar, P., Selvaraj, N., Rao, C. S. P. & Veeresh Kumar, G. B. Tribological behavior of ultrasonic assisted double stir casted novel nano-composite material (AA7150-hBN) using Taguchi technique. *Compos. Part B Eng.* **175**, 107136 (2019).

107. Krizhevsky, A., Sutskever, I. & Hinton, G. E. ImageNet classification with deep convolutional neural networks. *Commun. ACM* **60**, 84–90 (2017).

108. Wang, C., Tan, X. P., Tor, S. B. & Lim, C. S. Machine learning in additive manufacturing: State-of-the-art and perspectives. *Addit. Manuf.* **36**, 101538 (2020).

109. Bhaduri, A., Gupta, A. & Graham-Brady, L. Stress field prediction in fiber-reinforced composite materials using a deep learning approach. *Compos. Part B Eng.* **238**, 109879 (2022).

110. Kingma, D. & Ba, J. Adam: A Method for Stochastic Optimization. *Int. Conf. Learn. Represent.* (2014).

111. Herriott, C. & Spear, A. D. Predicting microstructure-dependent mechanical properties in additively manufactured metals with machine- and deep-learning methods. *Comput. Mater. Sci.* **175**, 109599 (2020).

112. Kim, J. & Lee, C. Prediction of turbulent heat transfer using convolutional neural networks. *J. Fluid Mech.* **882**, A18 (2020).

113. Fonda, E., Pandey, A., Schumacher, J. & Sreenivasan, K. R. Deep learning in turbulent convection networks. *Proc. Natl. Acad. Sci.* **116**, 8667–8672 (2019).

114. Lecun, Y., Bottou, L., Bengio, Y. & Haffner, P. Gradient-based learning applied to document recognition. *Proc. IEEE* **86**, 2278–2324 (1998).

115. Guo, X., Li, W. & Iorio, F. Convolutional neural networks for steady flow approximation. in *Proceedings of the 22nd ACM SIGKDD International Conference on Knowledge Discovery and Data Mining* 481–490 (2016).

116. Iyer, A., Dey, B., Dasgupta, A., Chen, W. & Chakraborty, A. A Conditional Generative Model for Predicting Material Microstructures from Processing Methods. in *Workshop on Machine Learning and the Physical Sciences (NeurIPS)* 1–6 (2019).

117. Mirza, M. & Osindero, S. Conditional generative adversarial nets. *arXiv Prepr. arXiv1411.1784* **v1**, (2014).

118. Nguyen, P. C. H. *et al.* Synthesizing controlled microstructures of porous media using generative adversarial networks and reinforcement learning. *Sci. Rep.* **12**, 9034 (2022).

119. Gebauer, N. W. A., Gastegger, M., Hessmann, S. S. P., Müller, K. R. & Schütt, K. T. Inverse design of 3d molecular structures with conditional generative neural networks. *Nat. Commun.* **13**, 1–11 (2022).

120. Shan, S. *et al.* Multistable Architected Materials for Trapping Elastic Strain Energy. *Adv. Mater.* **27**, 4296–4301 (2015).

121. Johnston, I. D., McCluskey, D. K., Tan, C. K. L. & Tracey, M. C. Mechanical characterization of bulk Sylgard 184 for microfluidics and microengineering. *J. Micromechanics Microengineering* **24**, 35017 (2014).

122. Demchuk, Z. *et al.* Unravelling the Influence of Surface Modification on the Ultimate Performance of Carbon Fiber/Epoxy Composites. *ACS Appl. Mater. Interfaces* **14**, 45775–45787 (2022).

123. Islam, M. N. & Jiang, Y. 3D Printable Sustainable Composites with Thermally Tunable

Properties Entirely from Corn-Based Products. *ACS Sustain. Chem. Eng.* **10**, 7818–7824 (2022).

124. Compton, B. G. & Lewis, J. A. 3D-printing of lightweight cellular composites. *Adv. Mater.* **26**, 5930–5935 (2014).

125. Jiang, Y. & Raney, J. R. 3D Printing of Amylopectin-Based Natural Fiber Composites. *Adv. Mater. Technol.* **4**, 1900521 (2019).

126. Liang, J. Z., Li, R. K. Y. & Tjong, S. C. Tensile properties and morphology of PP/EPDM/glass bead ternary composites. *Polym. Compos.* **20**, 413–422 (1999).

127. Affdl, JC Halpin and Kardos, J. The Halpin-Tsai Equations: A Review. *Polym. Eng. Sci.* **16**, 344–352 (1976).

128. Mori, T. & Tanaka, K. Average stress in matrix and average elastic energy of materials with misfitting inclusions. *Acta Metall.* **21**, 571–574 (1973).

129. Hashin, Z. & Rosen, W. B. The Elastic Moduli of Fibre-Reinforced Materials. *J. Appl. Mech.* **31**, 223–232 (1964).

130. Tsai, S. W. & wu, E. M. A General Theory of Strength for Anisotropic Materials. *J. Compos. Mater.* **5**, 58–80 (1971).

131. Egorikhina, E., Bogovalov, S. V. & Tronin, I. V. Determination of mechanical characteristics of unidirectional fiber composites. *Phys. Procedia* **72**, 66–72 (2015).

132. Yao, T., Zhang, K., Deng, Z. & Ye, J. A novel generalized stress invariant-based strength model for inter-layer failure of FFF 3D printing PLA material. *Mater. Des.* **193**, 108799 (2020).

133. Nelson, W. Weibull Analysis of Reliability Data with Few or No Failures. *J. Qual. Technol.* **17**, 140–146 (1985).

134. Barbero, E., Fernández-Sáez, J. & Navarro, C. Statistical analysis of the mechanical properties of composite materials. *Compos. Part B Eng.* **31**, 375–381 (2000).

135. Lee, K.-H., Lim, H. J. & Yun, G. J. A data-driven framework for designing microstructure of multifunctional composites with deep-learned diffusion-based generative models. *Eng. Appl. Artif. Intell.* **129**, 107590 (2024).

136. Dhariwal, P. & Nichol, A. Diffusion models beat gans on image synthesis. *Adv. Neural Inf. Process. Syst.* **34**, 8780–8794 (2021).

137. Nichol, A. Q. & Dhariwal, P. Improved denoising diffusion probabilistic models. in *International conference on machine learning* 8162–8171 (2021).

138. Wang, J. J., Jing, Y. Y., Zhang, C. F. & Zhao, J. H. Review on multi-criteria decision analysis aid in sustainable energy decision-making. *Renew. Sustain. Energy Rev.* **13**, 2263–2278 (2009).

139. Kaliszewski, I. & Podkopaev, D. Simple additive weighting - A metamodel for multiple criteria decision analysis methods. *Expert Syst. Appl.* **54**, 155–161 (2016).

140. Bhadra, D. & Dhar, N. R. Selection of the natural fiber for sustainable applications in aerospace cabin interior using fuzzy MCDM model. *Materialia* **21**, 101270 (2022).

141. Andre, N. G. & Ishak, Z. A. M. Predicting the Tensile Modulus of Randomly Oriented Nonwoven Kenaf/Epoxy Composites. *Procedia Chem.* **19**, 419–425 (2016).

142. Goodier, J. N. Concentration of Stress Around Spherical and Cylindrical Inclusions and Flaws. *J. Appl. Mech.* **1**, 39–44 (1933).

143. Yamanaka, K. & Kowaka, M. Mechanical Properties and Fracture Behavior of Chemically Bonded Composites. *Nippon Kinzoku Gakkai-si* **43**, 1151–1157 (1979).

144. Hashin, Z. & Rosen, B. W. The Elastic Moduli of Fiber-Reinforced Materials. *J. Appl. Mech.* **31**, 223–232 (1964).

APPENDIX A: MATHEMATICAL MODELS

A.1 Particle models

A.1.1 Rule of mixture for particle composites: The rule of mixtures is the simplest model for calculating stiffness and strength of a composite, assuming that both matrix and particles are subjected to equal strains and a perfect interface and stress transfer between matrix and particles.[141]

$$E_{c_p} = E_p f + E_m(1-f) \tag{A.1}$$

$$\sigma_{c_p} = \sigma_p f + \sigma_m(1-f) \tag{A.2}$$

where σ_p, σ_m, E_p, E_m are the strength and stiffness of the particle fillers and matrix, respectively. f, E_{c_p}, σ_{c_p} are the volume fraction of particle fillers, stiffness of the particle composite, and strength of the particle composite.

A.1.2 Rigid inclusion model: Goodier solutions are used to define high internal stress gradients associated with elastic inhomogeneities for spherical inclusions, which affect the mechanical strength of composite materials.[142] The rigid inclusions produce different types of stress concentrations due to the interaction with surrounding materials.[143] The expression of stress concentration in the inclusions are

$$\sigma_p = 2G_p\left[-\frac{A}{r^2} + \left(\frac{3B}{r^4} - \frac{2C}{r^2}\right)cos2\theta\right] + \frac{T}{2}(1 + cos2\theta) \tag{A.3}$$

where $A = \frac{TR^2}{4G_p}\frac{(1-2\upsilon_m)G_p-(1-2\upsilon_p)G_m}{(1-2\upsilon_p)G_p+G_m}$, $B = \frac{TR^4}{4G_p}\frac{G_p-G_m}{(3-3\upsilon_p)G_m+G_p}$, and $C = \frac{TR^2}{2G_p}\frac{G_p-G_m}{(3-4\upsilon_p)G_m+G_p}$.

T is the applied tensile load, θ is angle from direction of applied load for maximum stress concentration, A, B, C are the tensile stress concentration to the regions of particle, G_p is shear modulus of glass, G_m is shear modulus of matrix, υ_p is the Poisson's ratio of the glass particle, υ_m is the Poisson's ratio of the matrix, R is the inner radius of the thin-shell hollow particles, and r is the outer radius.

A.1.3 Mori-Tanaka model: In the Mori-Tanaka model, the correlation between the strength of the composite and volume fraction of particles can be derived when the matrix and the filler are elastic.[128] The following equation are[41]

$$\sigma_{c_p} = E_m \varepsilon_c \left[1 + \frac{\lambda f(\frac{E_p}{E_m}-1)}{1+(1-f)(\frac{E_p}{E_m}-1)(\frac{7-5\upsilon_p}{15(1-\upsilon_p)})}\right] \quad \text{(A.4)}$$

where λ =1.5, which is a constant related to particle size distribution, geometry and interfacial adhesion, ε_c is the strain of composite.

A.1.4 Halpin-Tsai model for particle composites: In an effort to describe particle-matrix micromechanics, Halpin-Tsai developed a generalized equation[127,144]

$$\sigma_{c_p} = \varepsilon_c \left[\left(\frac{E_m f}{3E_m+4G_m} + \frac{E_p(1-f)}{3E_p+4G_m}\right) / \left(\frac{1-f}{3E_m+4G_m} + \frac{f}{3E_p+4G_m}\right)\right] \quad \text{(A.5)}$$

A.2 Fiber model

To define fiber-matrix and interlayer failure, the tensile strength can be derived from Halpin-Tsai model and Tsai-Hill criterion.[47,127,130–132] The expression of tensile strength is

$$\sigma_{c_f} = \left(\frac{cos^4\theta}{(E_1\epsilon_1)^2} + \frac{sin^4\theta}{(E_2\epsilon_2)^2} + \left(\frac{1}{G_{12}\gamma_{12}} - \frac{1}{(E_1\epsilon_1)^2}\right) sin^2\theta cos^2\theta\right)^{-\frac{1}{2}} \quad \text{(A.6)}$$

in which $E_1 = E_m \left(\frac{1+\frac{2l}{d}\eta_1 f}{1-\eta_1 f}\right)$ and $E_2 = E_m \left(\frac{1+2\eta_2 f}{1-\eta_2 f}\right)$

Here, the in-plane shear modulus is $G_{12} = \frac{\upsilon_f}{G_f} + \frac{\upsilon_m}{G_m}$, the in-plane shear strain is $\gamma_{12} = \frac{\tau_{12}}{G_{12}} = \frac{f\tau_f+(1-f)\tau_m}{G_{12}}$, θ is the fiber orientation angle against loading direction, ϵ_1 and ϵ_2 are the strain in the longitudinal and transverse direction, respectively. A measure of reinforcement geometry and stiffness contrast between filler and matrix is described in $\eta_1 = \frac{E_f - E_m}{E_f + \frac{2l}{d}}$ for longitudinal direction and $\eta_2 = \frac{E_f - E_m}{E_f + 2}$ for transverse direction. The fiber diameter d= 11.66 μm is determined experimentally in this study and l is the length of the fiber, which is $l = 110 - 36.5\left(1 - e^{-\left(\frac{f}{0.065}\right)^{10}}\right)$ mm determined experimentally from previous study.[24]

A.3 Hybrid strength model:

In the hybrid model, we incorporated individual models of fiber-matrix and particle-matrix failure probability via a Weibull distribution function. The strength of hybrid composite is

$$\sigma_c = \sigma_{c_f} P_{s_f} + \sigma_{c_p} P_{s_p} \tag{A.7}$$

and P_{s_f} and P_{s_p} are the probability of failure of the fiber-matrix and particle-matrix, respectively, under a uniaxial tensile.

$$P_{s\_f} = 1 - e^{\left(-\frac{l}{l_{cr}}\left(\frac{\sigma}{\sigma_{crf}}\right)^{m_1}\right)} \tag{A.8}$$

$$P_{s\_p} = 1 - e^{\left(-\left(\frac{\sigma}{\sigma_{crp}}\right)^{m_2}\right)} \tag{A.9}$$

where m_1 and m_2 are the Weibull coefficients of fiber-matrix and particle-matrix interfaces, respectively. σ_{crf} and σ_{crp} are the critical strength of fiber-matrix and particle-matrix interfaces. l_{cr} is the critical length of fiber which is associated with the critical strength σ_{crf}. σ_{c_p} and σ_{c_f} are the strength of particle composite and fiber composite, defined in Eq. (A.4) and (A.6) respectively.

The Weibull parameters and the critical stresses are calculated using the general linear regression method and the weight function.[134]

$$\mathrm{m} = \frac{(\sum w_i)(\sum w_i z_i y_i) - (\sum w_i z_i)(\sum w_i y_i)}{(\sum w_i)(\sum w_i z_i^2) - (\sum w_i z_i)^2} \tag{A.10}$$

$$\sigma_{cr} = e^{\left(-\frac{a}{m}\right)} \tag{A.11}$$

where $z_i = \ln \sigma_i$, $y_i = \ln[\ln(\frac{1}{1-F_i})]$, $w_i = [(1-F_i)\ln(1-F_i)]^2$, $F_i = \frac{i-0.3}{n+0.4}$, and $a = \frac{(\sum w_i y_i) - m(\sum w_i z_i)}{(\sum w_i)}$. n is the number of samples are considered, for fiber, n=11 and for particle, n=20.

APPENDIX B: MATERIALS PROPERTY

Table B.1. ANOVA table for stiffness.

Parameter	SSV	MSV	MSE	MSV/MSE	F(2,33,α=0.05)	Percentage of contribution (%)
Fiber (vol %)	3.03	1.51	0.21	7.16	Significant	30.26
Particle (vol %)	2.13	1.07	0.24	4.47	Significant	21.32
Printing direction	4.53	2.26	0.16	13.63	Significant	45.24
Nozzle size	0.32	0.16	0.29	0.54	Insignificant	3.16

Table B.2. ANOVA table for strength.

Parameter	SSV	MSV	MSE	MSV/MSE	F(2,33,α=0.05)	Percentage of contribution (%)
Fiber (vol %)	1.72	0.86	0.038	22.46	Significant	57.64
Particle (vol %)	0.64	0.32	0.071	4.57	Significant	21.68
Printing direction	0.32	0.16	0.081	2.01	Insignificant	10.86
Nozzle size	0.29	0.15	0.082	1.79	Insignificant	9.81

Here, SSV is sum of square of a variable, MSV is mean square of a variable, MSE is mean square error of a variable. For significance F-test, the confidnece interval is 95% (α=0.05).

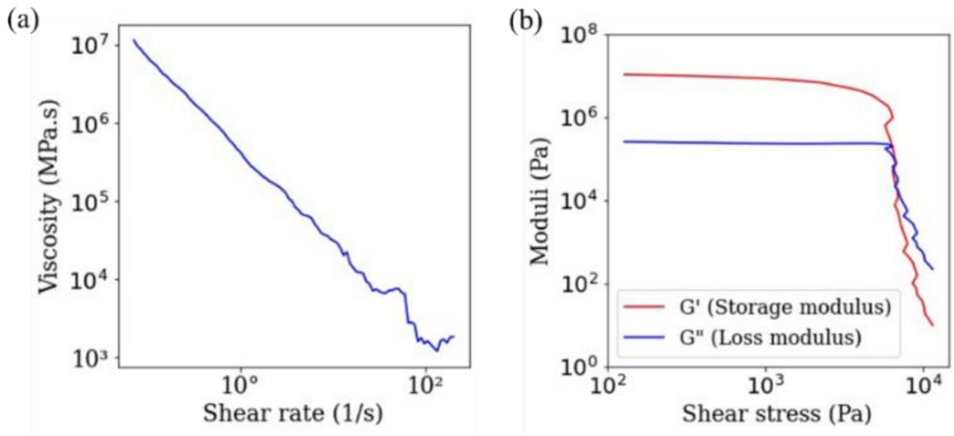

Fig. B.1. Rheology characterization of 3D printability of the ink of hybrid composite materials, showing (a) shear thinning and (b) yielding behaviors.

USE OF PREVIOUSLY PUBLISHED MATERIAL

Material in sections 2.1 second paragraph, 2.2 second paragraph, 2.3 first paragraph, 2.4.1, 2.4.3, 3.1, 3.2, 3.3, 3.4.1, 4.1-4.3, Appendix A, and Appendix B is reproduced and revised from the following publication:

Sanjida Ferdousi, Rigoberto Advincula, Alexei P Sokolov, Wonbong Choi, & Yijie Jiang. (2023). "Investigation of 3D printed lightweight hybrid composites via theoretical modeling and machine learning." Compos. Part B Eng. 265, 110958, https://doi.org/10.1016/j.compositesb.2023.110958